

1994

Measurements and modelling of structure sensitive magnetic properties of materials

Zhao-Jun Chen
Iowa State University

Follow this and additional works at: <https://lib.dr.iastate.edu/rtd>

 Part of the [Electrical and Electronics Commons](#), and the [Materials Science and Engineering Commons](#)

Recommended Citation

Chen, Zhao-Jun, "Measurements and modelling of structure sensitive magnetic properties of materials " (1994). *Retrospective Theses and Dissertations*. 10546.

<https://lib.dr.iastate.edu/rtd/10546>

This Dissertation is brought to you for free and open access by the Iowa State University Capstones, Theses and Dissertations at Iowa State University Digital Repository. It has been accepted for inclusion in Retrospective Theses and Dissertations by an authorized administrator of Iowa State University Digital Repository. For more information, please contact digirep@iastate.edu.

INFORMATION TO USERS

This manuscript has been reproduced from the microfilm master. UMI films the text directly from the original or copy submitted. Thus, some thesis and dissertation copies are in typewriter face, while others may be from any type of computer printer.

The quality of this reproduction is dependent upon the quality of the copy submitted. Broken or indistinct print, colored or poor quality illustrations and photographs, print bleedthrough, substandard margins, and improper alignment can adversely affect reproduction.

In the unlikely event that the author did not send UMI a complete manuscript and there are missing pages, these will be noted. Also, if unauthorized copyright material had to be removed, a note will indicate the deletion.

Oversize materials (e.g., maps, drawings, charts) are reproduced by sectioning the original, beginning at the upper left-hand corner and continuing from left to right in equal sections with small overlaps. Each original is also photographed in one exposure and is included in reduced form at the back of the book.

Photographs included in the original manuscript have been reproduced xerographically in this copy. Higher quality 6" x 9" black and white photographic prints are available for any photographs or illustrations appearing in this copy for an additional charge. Contact UMI directly to order.

UMI

A Bell & Howell Information Company
300 North Zeeb Road, Ann Arbor, MI 48106-1346 USA
313/761-4700 800/521-0600



Order Number 9518366

**Measurements and modelling of structure sensitive magnetic
properties of materials**

Chen, Zhao-Jun, Ph.D.

Iowa State University, 1994

U·M·I

300 N. Zeeb Rd.
Ann Arbor, MI 48106

**Measurements and modelling of structure sensitive
magnetic properties of materials**

by

Zhao-Jun Chen

A Dissertation Submitted to the
Graduate Faculty in Partial Fulfillment of the
Requirements for the Degree of
DOCTOR OF PHILOSOPHY

Department: Electrical Engineering and Computer Engineering
Major: Electrical Engineering (Electromagnetics)

Approved:

Signature was redacted for privacy.

In Charge of Major Work

Signature was redacted for privacy.

For the Major Department

Signature was redacted for privacy.

For the Graduate College

Iowa State University
Ames, Iowa

1994

TABLE OF CONTENTS

	Page
GENERAL INTRODUCTION	1
Materials Evaluation Using Magnetic Measurement Techniques	2
Statement of Problem and Scope of Dissertation	4
Objective and Expected Contribution	5
Magnescope for In-situ Magnetic Measurement	7
Dissertation Organization	7
PART I. MODELLING OF STRUCTURE SENSITIVE MAGNETIC PROPERTIES DUE TO EFFECTS OF LOCALIZED DEFECTS	11
INTRODUCTION	12
MODELLING OF INITIAL PERMEABILITY	16
Background	16
Reversible Wall Bowing and Initial Permeability	16
Initial Permeability as a Function of Carbon Content	21
MODELLING OF MAGNETIC PROPERTIES USING THE THEORY OF HYSTERESIS	24
Theory of Hysteresis	24
Modelling of Hysteresis Curves	25
Physical Interpretation of Hysteresis Modelling Parameters	26

CONCLUSIONS	37
REFERENCES	38
PART II. MAGNETIC HYSTERESIS MEASUREMENTS IN THE DETECTION OF EFFECTS OF THE FATIGUE	40
INTRODUCTION	41
EXPERIMENTAL	44
Materials and Specimens	44
Mechanical Tests	44
Fatigue Tests	44
Inspection Head	49
Magnetic Measurements	50
Metallurgical Study	50
RESULTS AND DISCUSSIONS	53
Fatigue Analysis	53
Magnetic Hysteresis Measurement	57
Metallurgical Study	72
Dependence of Coercivity on the Number of Fatigue Cycles	90
CONCLUSIONS	92
REFERENCES	93

PART III. MAGNETIC HYSTERESIS MEASUREMENTS IN THE DETECTION OF CREEP DAMAGE	95
INTRODUCTION	96
EXPERIMENTAL	100
Materials and Specimens	100
Inspection Head	100
Magnetic Measurements	105
Metallurgical Study	106
RESULTS	107
Magnetic Hysteresis Measurements	107
Metallurgical Study	110
DISCUSSIONS	125
Creep Analysis	125
Analysis of Magnetic Measurement	126
PHYSICAL MODEL AND NUMERICAL CALCULATION	128
CONCLUSIONS	133
REFERENCES	134
PART IV. PRACTICAL TECHNIQUES TACKLING PROBLEMS IN SURFACE MAGNETIC HYSTERESIS MEASUREMENT	136
INTRODUCTION	137
A. DEVELOPMENT OF TRANSFER FUNCTION TO MEASURE INTRINSIC MAGNETIC PROPERTY FROM SURFACE INSPECTION	140

Background	140
First Approximation and Leakage Coefficient	144
Surface Magnetic Charge Model	145
Transfer Function with Flux Leakage and Geometry Correction	151
Test Results and Discussions	151
Conclusions and Future Work	162
B. IMPROVEMENT OF MAGNETIC SURFACE MEASUREMENT BY REDUCING LIFT-OFF EFFECT	164
Background	164
Experimental	165
Results and Discussions	170
Magnetic Circuit Model	178
Conclusions	181
REFERENCES	183
GENERAL CONCLUSIONS	184
GENERAL REFERENCES	187
ACKNOWLEDGEMENTS	190

GENERAL INTRODUCTION

It is well known that the magnetic properties of ferromagnetic materials depend strongly on microstructural features such as grain size, dislocation density, and size and density of inhomogeneous second phases. When a ferromagnetic material is under an external magnetic field, some of its domains which are oriented favorably with respect to the magnetic field grow at the expense of the others mainly by domain wall translation but also by domain rotation. Since domain walls carry a stress field due to a combination of the exchange energy, magnetocrystalline anisotropy and magnetoelastic coupling, they interact with the strain fields of the different structural defects. In other words, it is the magnetostrictive coupling (and also the magnetostatic coupling if the defect is larger than the thickness of the domain wall) between the structural defects and the domain walls that affects the motion of the domain wall, and therefore the magnetic properties. The irreversible motion of the domain walls during the magnetization process is the origin of magnetic hysteresis. For this reason, the research and development of magnetic materials is heavily reliant on the metallurgy. For example, controlling microstructure features such as content of impurities, recrystallization, composition, and precipitation processes has allowed for a gradual improvement in specific magnetic alloys. On the other hand, it is also possible to exploit the magnetization process in reverse order, i.e., to deduce microstructural information from the magnetization process. The present work mainly elaborates upon this point of view, concentrating on the application of the dependence between the microstructure and magnetization process in the area of nondestructive evaluation (NDE) of ferromagnetic

materials, mainly steel components in structural systems.

Materials Evaluation Using Magnetic Measurement Techniques

The subject of nondestructive evaluation has become very important as more industries become aware of the potential benefits of plant life extension, the cost effectiveness of retiring only the defective components and the possibilities of avoiding potentially catastrophic failures by monitoring the condition of structures both for defects and the presence of high levels of stress. Besides most commonly used ultrasonic and eddy current techniques, magnetic methods are unique for nondestructive evaluation of steel because they utilize the inherent ferromagnetic properties of the steel for detection of a wide range of material properties from cracks to residual strain. The magnetic NDE techniques include, but are not limited to, the Barkhausen effect, magnetoacoustic emission, magnetic hysteresis, residual field and magnetoelastic methods for evaluation of intrinsic properties of magnetic materials; and magnetic particle inspection and magnetic flux leakage for detection of flaws, cracks and other macroscopic inhomogeneities. Reviews of magnetic methods for nondestructive evaluation have been given by Jiles [1,2] and recently by Devine [3]. A review on Barkhausen effect technique has also been given by Matzkanin et al. [4]. The work within this dissertation will concentrate on the new developments in the application of the magnetic hysteresis measurement technique in NDE.

Magnetic hysteresis measurements are based on the extraction of a number of parameters which describe the shape of the hysteresis loop of a ferromagnetic material (see Fig. 1). The hysteresis properties such as permeability, coercivity, remanence and hysteresis

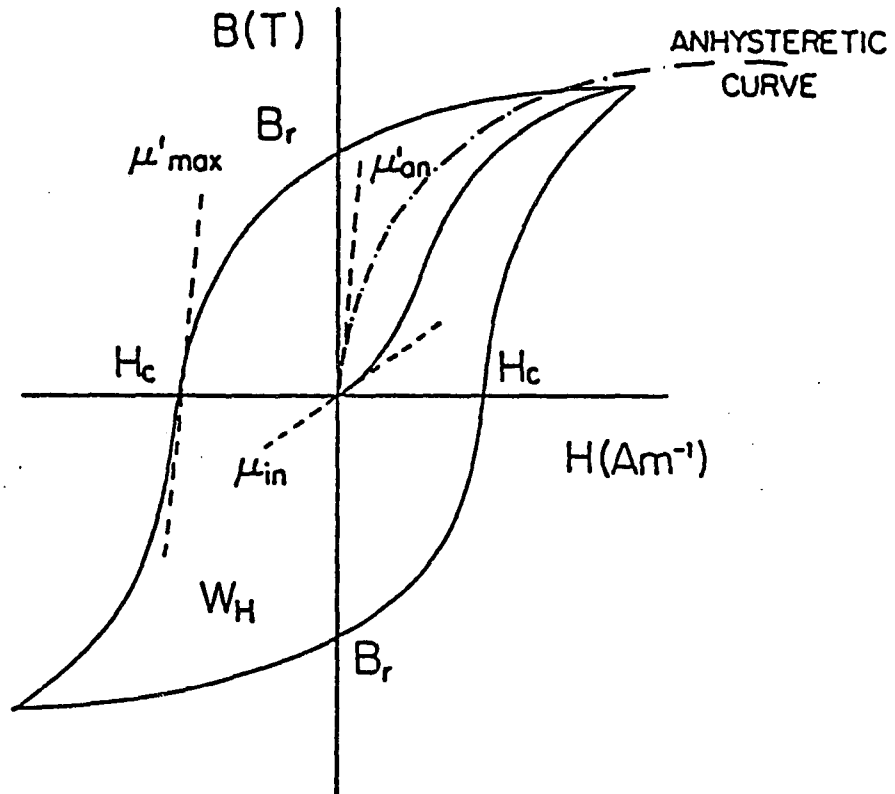


Fig. 1. Hysteresis loop of ferromagnetic material, showing different components extracted for materials evaluation.

loss are known to be sensitive to such factors as stress [5,6], strain [7,8], grain size [9], dislocation density [10,11], heat treatment [12] and the presence of precipitates of a second phase, such as iron carbide [13] in steels. It was reported earlier [14] that several independent parameters are needed in order to identify the change in magnetic properties whether it is due to external stress, microstructure or other effects. Since several independent parameters can be obtained through a single measurement, the hysteresis measurement technique is ideally suited for the determination of intrinsic properties of steel.

Statement of Problem and Scope of Dissertation

Although the application of magnetic hysteresis techniques for NDE has been reported in the early 1970's, including the detection of the heat treatment effect [15,16], stress [17] and texture [18], it was not until the late 1980s when intensive basic research was conducted on the inter-dependence of microstructure [7-13,19-20], and external stress [5,6] on the magnetic properties of steels, that the hysteresis measurement technique began to demonstrate a promising role in the detection of stress effects [6,21], fatigue effects [22,23], thermomechanical damage (creep damage) [24] and irradiation degradation [25]. Besides the advancement in magnetic hysteresis measurement techniques [26-28], much of the progress was also due to the development of the hysteresis theory [29-32] and the modelling of the mechanism of domain wall microstructure interaction in magnetization process [33-35]. However, the interpretation of changes in the hysteresis characteristics in terms of fundamental changes in sample properties still remains a difficult problem. The practical problems such as the demagnetizing effect, the geometry effect and the lift-off effect (or any

combination of them) also influence the magnetization process and the measurement result [36-37]. Therefore, the extraction of intrinsic magnetic properties from a measured hysteresis loop to maximize the measurement information is critical for successful magnetic testing. This is especially true for on-site measurement where the opportunity for material preparation is minimal.

In this dissertation, the modelling of magnetic properties and hysteresis curves will be stated first as a contribution to the theory of magnetism. The work will focus on the relationship between the defect density in a material and the initial permeability as well as magnetic hysteresis modelling parameters. Then the application of hysteresis measurement technique in the assessment of fatigue and creep induced microstructure will be studied. Research will be focused on the relationship between accumulated fatigue and creep damage to the variation of structure sensitive magnetic parameters. Finally practical techniques for on-site surface magnetic NDT measurement will be addressed. Emphasis is on the correction of flux leakage effect, geometry effect and the lift-off problem.

Objective and Expected Contribution

According to the scope of this thesis, the research within this dissertation will be composed of three areas: modelling of magnetic properties, applications of magnetic NDE method and measurement techniques.

1) Modelling of Magnetic Properties

The objective of this part of the dissertation is to model the structure-sensitive magnetic properties. Only localized spherical volumetric defects are considered. As a result,

the initial permeability as a function of defect density will be derived based on the domain wall bowing approximation.

As an alternative way of modelling magnetic properties, hysteresis modelling theory [29-32] will be used. This method gives more complete information on magnetic properties. In order to correlate microstructural features with magnetic properties, the relationship between hysteresis modelling parameters and defect density will be derived.

2) NDE Application of Hysteresis Measurement

The objective of this part of the dissertation is to apply the hysteresis measurement technique to practical industrial problems of fatigue and creep damage. Magnetic properties of a ferromagnetic material are very sensitive to microstructure, thermal history and external stress. Previous research [22-24] has already shown the potential of this technique in non-destructive assessment of fatigue and creep damage.

The work within this dissertation aims to conduct a systematic study on the magnetic properties of fatigue and creep damaged materials under different test conditions, and to find structure property relationships so that the magnetic NDE technique can be used to assess the quality of a structural component which is in service. Phenomenological models will also be developed based on experimental results.

3) Measurement Techniques

The objective of this part is to solve some practical problems in the surface magnetic hysteresis measurement. In a real NDE situation, the hysteresis magnetic measurement technique is impaired by the sample preparation, the shape of the specimen, and the position of the inspection head with respect to the specimen. As a result, the flux leakage effect,

geometrical effect and lift-off effect will influence the measurement and make the interpretation of results difficult in terms of the variation of the intrinsic properties.

In this part of the dissertation, flux leakage and geometry effects will be analyzed and a transfer function will be developed to correct of the flux leakage for the geometry of the specimen and inspection head. The influence of the surface condition of a specimen and the lift-off effect on the measurement result will be resolved by the use of a magnetic coupling gel and pre-lifting technique, which will reduce the measurement fluctuation and separate the intrinsic magnetic property from the artifacts due to the test condition. A magnetic circuit model will also be developed to address these problems.

Magnescope for In-situ Magnetic Measurement

A special magnetic hysteresis measurement instrument the Magnescope [22] should also be mentioned here. It is a portable computer controlled electronics system which employs specially designed data acquisition and analysis software. The block diagram of the system is shown in Fig. 2. Most of the data presented in this thesis were measured by the Magnescope in conjunction with surface inspection heads. The Magnescope has found applications in the field measurement of stress [35] and creep effects [36].

Dissertation Organization

This dissertation is composed of four parts. The modelling of the structure-sensitive magnetic properties is contained in Part I. It describes the influence of localized point defects on magnetic properties and magnetic modelling parameters. Portions of this part have been

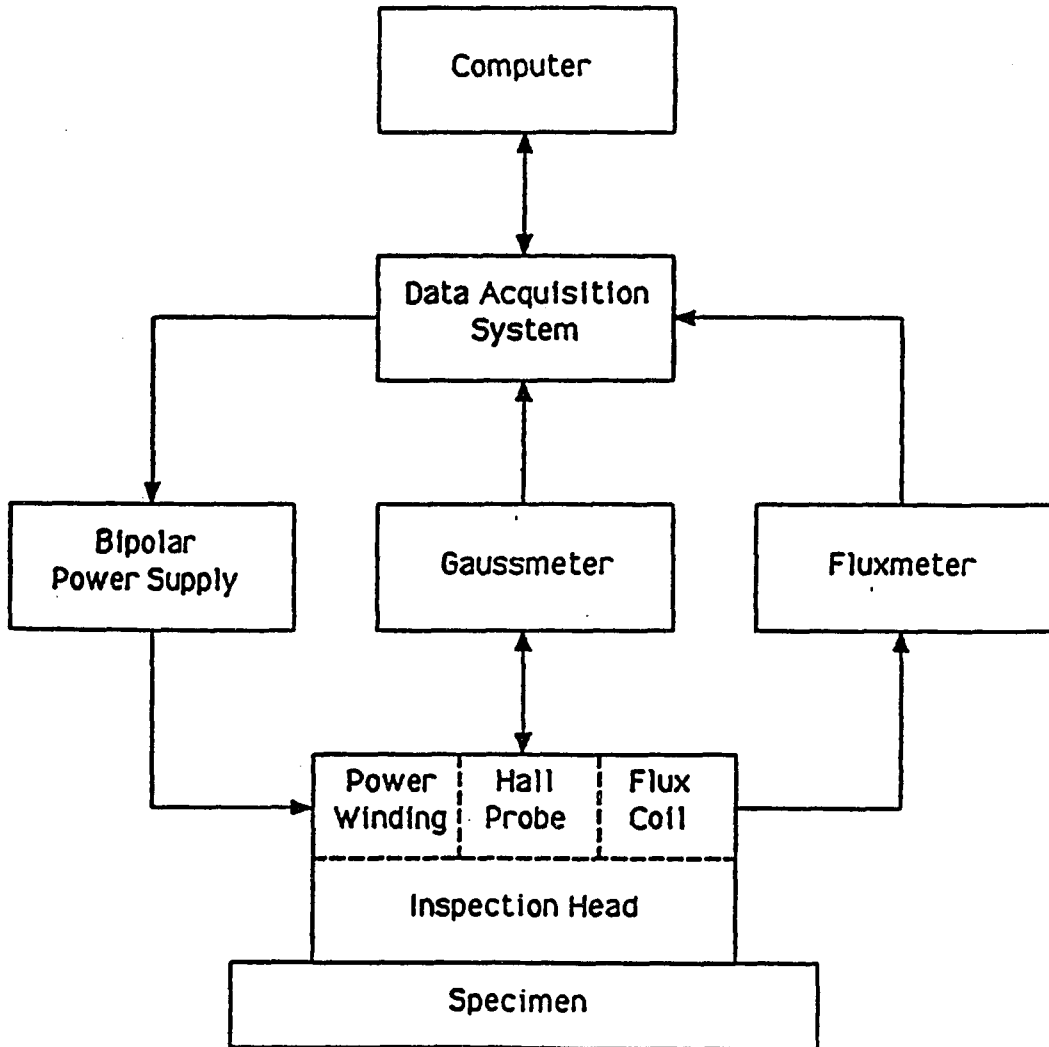


Fig. 2. Block diagram of the Magnoscope.

published or are going to be submitted as two papers. One paper entitled "Modelling of reversible domain wall motion under the action of magnetic field and localized defects" has been published in IEEE Transactions on Magnetics, Vol.29, No.6, 2554, November, 1993 and the other "The effect of point defect on magnetic modelling parameters" will be submitted to IEEE Transactions on Magnetics.

The study of the effect of fatigue on magnetic properties is contained in Part II. This mainly consists of the research results from a project "Application of a new magnetic monitoring technique to in situ evaluation of fatigue damage in ferrous components of nuclear primary systems." Some of the results have already been published in "Micromagnetic surface measurements for evaluation of surface modification due to cyclic stress," IEEE Transaction on Magnetics, Vol.29, No.6, 3031, November, 1993, "Estimation of fatigue exposure from magnetic hysteresis parameters," Journal of Applied Physics 75(10), 6975, May, 1994 and "SEM & TEM investigation of fatigue induced microstructural changes and resulting effect on magnetic properties of structural steels," Proceedings of 1993 ASM Material Week. The other results have been submitted in a paper to Journal of Magnetism and Magnetic Materials entitled as "Effect of structural inhomogeneities on the magnetic properties of iron based alloys."

The application of magnetic hysteresis techniques in the detection of creep is contained in Part III. Portions of this part have been accepted for publication as two papers resulting from a project "Mechanical Deformation Effect on Magnetic Properties." One of the papers "Assessment of creep damage of ferromagnetic material using magnetic inspection" has been accepted for publication in IEEE Transaction on Magnetics and the

other "Detection of creep damage of Cr-Mo steel by magnetic hysteresis measurement" will be published in Review of Progress in Quantitative Nondestructive Evaluation.

Part IV addresses some practical problems of on-site surface magnetic hysteresis measurements for NDE applications. The flux leakage effect has been discussed in "Measurement of magnetic circuit characteristics for comprehension of intrinsic magnetic properties of materials from surface inspection," published in Journal of Applied Physics 73(10), 5620, May, 1993. The transfer function for surface magnetic measurement with a correction for the geometrical effects is to be submitted to IEEE Transaction on Magnetics and the portion addressing the lift-off effect has been submitted for International Magnetics Conference of 1995 and will be scheduled for publication in IEEE Transactions on Magnetics.

Following Part IV are general conclusions. References cited within each part are listed at the end of that part. References cited in the General Introduction follow the General Conclusions.

PART I.

**MODELLING OF STRUCTURE SENSITIVE MAGNETIC
PROPERTIES DUE TO EFFECTS OF LOCALIZED DEFECTS**

INTRODUCTION

Magnetic properties can generally be divided into two categories. These are structure sensitive properties, such as coercivity, permeability, remanence and hysteresis loss, and structure insensitive properties such as saturation magnetization, saturation magnetostriction, exchange coupling and Curie temperature. In the past, the structure insensitive properties have been the subject of numerous investigations and consequently by now are well understood. By comparison the structure sensitive properties of magnetic materials are still relatively poorly understood, as noted by Litmann [1].

Since the study of structure sensitive magnetic properties is not only important for the understanding of micromagnetic processes, it is also beneficial in elucidating the underlying principles for material characterization by magnetic nondestructive testing methods [2,3]. Significant effects have recently been made to understand these processes. For example, the effects of carbides on magnetic properties were studied recently using alloys of the iron-carbon system [4,5]. It was found that magnetic properties were highly sensitive to the carbon content as well as the morphology of iron carbide particles. It was concluded that the pinning effects of Fe_3C particles on the domain wall were responsible for the increase in coercivity and hysteresis loss and the decrease in initial permeability. The effects of grain size on magnetic properties were also studied [6] and found that coercivity and hysteresis loss decrease with grain size as grain size increases up to 1 mm. Other effects of microstructure, such as chemical composition [7], porosity [8], dislocation [9] and lattice defects [10] have also been studied.

Besides experimental work, theoretical modelling of structure sensitive magnetic properties has also been of interest. The influence of lattice defects on the mobility of domain walls has been investigated in cases of dislocations [9], point defects [11] and antiphase boundaries [12]. Hilzinger and Kronmuller [13] concluded that, in the rigid domain wall approximation, the coercive force H_c depends on defect density ρ and wall area F_B according to

$$H_c \sim \rho^{1/2} F_B^{-1/2} \quad (1)$$

and in domain wall bowing approximation, coercive force H_c relates to defects density according to following relation:

$$H_c \sim \rho^{2/3} \quad (2)$$

Although the Hilzinger-Kronmuller theories are greatly oversimplified and therefore of little practical significance in real materials, they do point out a first principles relationship between structure and properties of magnetic materials.

In the theoretical work it is noticed that the previous models were mainly focused on the discussion of coercive force, although some progress has also been made on the modelling of initial permeability [14,15], another important structure sensitive magnetic property. In the practical situation, especially in magnetic NDE measurement, where the saturation of a specimen is usually difficult, initial permeability has its advantage over coercive force as a measurement parameter, since it is independent of the maximum applied magnetic field. Based on the reversible domain wall motion under the action of a magnetic field and localized defects, this paper will present a model for the relationship between initial

permeability and defect density.

Besides the direct modelling of a single structure sensitive magnetic property such as coercive force or initial permeability, the modelling of the whole hysteresis curve could ideally be the alternative way to understand the structure sensitive magnetic properties. The advantage of modelling the hysteresis curve is quite obvious: it can provide complete information on the structure sensitive magnetic properties from a single modelling. The difficulty mainly results from the lack of a physically based model of hysteresis. Most hysteresis models available in the past either only fit a restricted region of the curve with physical meaning [16,17] or fit for the whole curve with high accuracy but without physical foundation [18]. In this paper, it will be demonstrated that, with aid of a newly-developed hysteresis theory, modelling of structure sensitive magnetic properties through complete hysteresis loop modelling can be achieved. The hysteresis theory used here is based on that originally developed by Jiles and Atherton [19-21]. This theory describes the entire hysteresis curve with a high degree of accuracy. One of the most successful aspects of this theory is that it is based only on a few dominant mechanisms which are incorporated into the model through a limited number of parameters. In order to model the structure sensitive magnetic properties, the essential point here is to find the relationship between the microstructure features and the hysteresis modelling parameters.

The following discussion assumes that distributed defects are the only microstructure feature which influence domain wall motion. Modelling of initial permeability from first principles will be performed, followed by the magnetic hysteresis curve modelling. Finally

the correlation between microstructural features and hysteresis modelling parameters will be established.

MODELLING OF INITIAL PERMEABILITY

Background

Isolated regions of second-phase material with magnetic properties different from those of the matrix material are known as magnetic inclusions. These reduce the energy of domain walls when the domain walls intersect them and consequently the domain walls become attracted to the inclusions which effectively impede wall motion. The inclusions themselves may take many forms such as insoluble second-phase material, which appears if the solubility limit of the minority element has been exceeded, they may be oxides or carbides, or they may be pores, voids, cracks or other mechanical inhomogeneities. Well-known examples of magnetic inclusions are cementite (Fe_3C) particles in iron and steels. This paper treats magnetic inclusions as localized defects, and models their pinning effects on domain wall motion. For simplicity of calculation, a uniform distribution of localized inclusions is assumed.

Reversible Wall Bowing and Initial Permeability

Domain wall bowing is a reversible process at low field amplitudes and is the main mechanism of domain wall motion at the origin of the initial magnetization curve. The influence of the localized defects on domain wall bowing is an important problem because this determines the details of the magnetization curve in most materials.

Under the action of a magnetic field, the domain wall expands like an elastic membrane. In order to have a tractable mathematical description of domain wall bowing

without losing the basic physical picture, some simplifying assumptions must be made. These are as follows:

1) The localized pinning sites are the only type of pinning sites considered for domain wall motion.

2) These pinning sites are uniformly distributed inside the material and the separation between pinning sites is $2a$. This is shown in Fig. 3.

3) Initially, we consider the domain walls to be flat and one of them is considered to be sitting on the x - y plane with pinning sites uniformly distributed over its surface. On applying an external field \mathbf{H} , the domain wall bends upward. This is shown in Fig. 4.

4) Only a 180° domain wall is considered here with the applied field parallel to the direction of \mathbf{M}_s in one domain. (If there exist other kinds of domain walls, a factor of $\cos(\vartheta)$ should replace $\cos(180^\circ)$ in the derivation, where ϑ is the angle between \mathbf{M}_s and \mathbf{H} .)

5) The final shape of the domain is determined by minimization of the total energy, which we will assume is mainly composed of domain surface energy and field energy.

For isotropic materials, the domain wall bends around the pinning site with local symmetry in the Φ direction and with an average radius curvature of r . Based upon the above assumptions, the domain wall area associated with a pinning site at point O in Fig. 3 is

$$A = \int_0^a 2\pi y \sqrt{1 + (dz/dy)^2} dy \quad , \quad (3)$$

where $z=z(y,r,a)$ is the equation of curve OA.

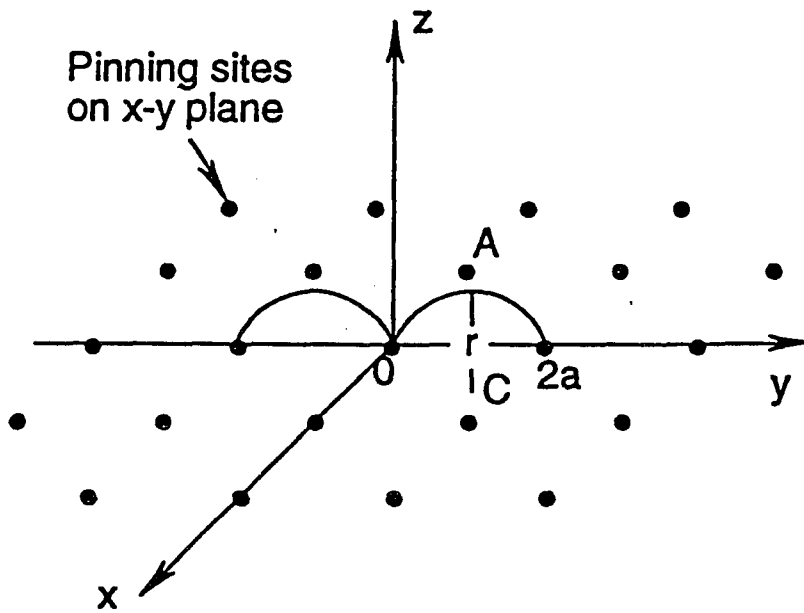


Fig. 3. Domain wall and pinning site configuration on x-y plane.

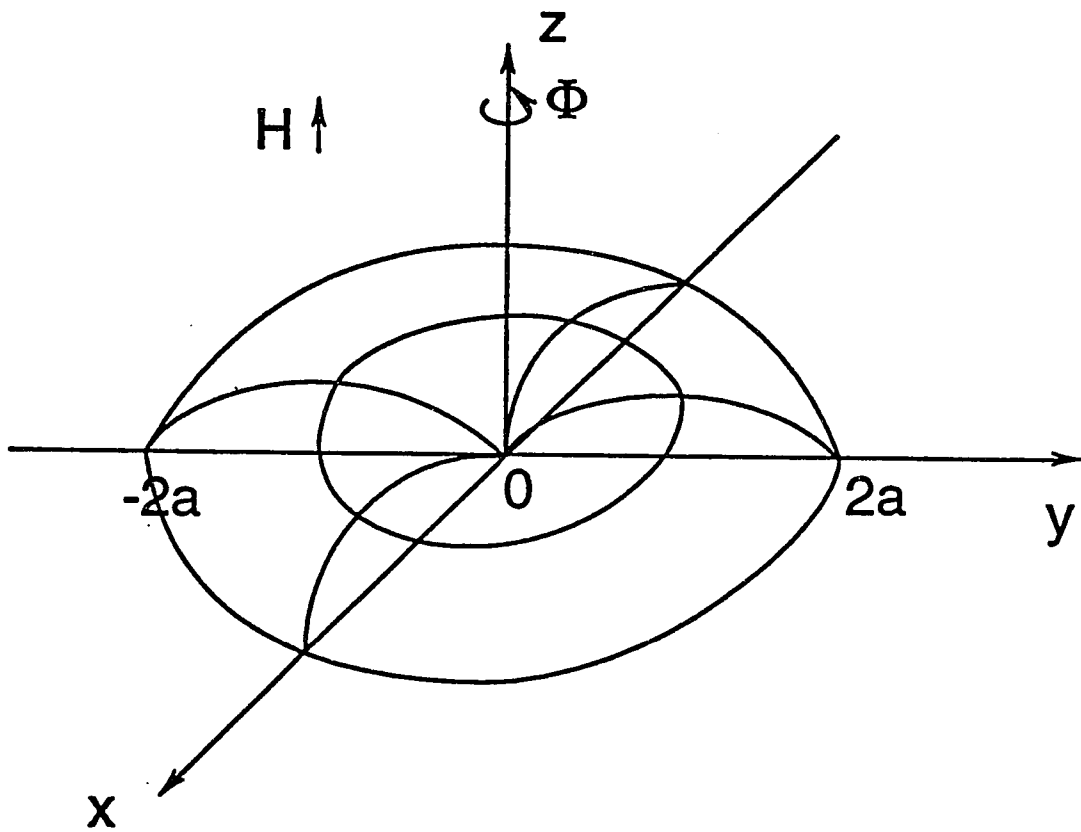


Fig. 4. Domain wall bowing on pinning site O under the action of magnetic field H .

$$z = \sqrt{r^2 - (y-a)^2} - \sqrt{r^2 - a^2} \quad (4)$$

In the low field region, for small distortions of the wall, $r \gg a$ and $r \gg y$, and this simplifies the change in the area of domain wall as follows:

$$\begin{aligned} \Delta A &= A - \pi a^2 \\ &\approx \int_0^a \frac{1}{2} \left(\frac{a-y}{\sqrt{r^2 - (y-a)^2}} \right)^2 2\pi y \, dy \\ &\approx \frac{\pi a^4}{12 r^2} . \end{aligned} \quad (5)$$

Similarly, the volume swept out by a domain wall is

$$\Delta V = \int_0^a z \, 2\pi y \, dy \approx \frac{5}{12} \frac{\pi a^4}{r} . \quad (6)$$

Therefore the change in magnetic energy as a result of the deformation of a 180° domain wall is

$$\begin{aligned} \Delta E &= \gamma \Delta A - M_s H (1 - \cos(180^\circ)) \Delta V \\ &= \frac{\pi a^4 \gamma}{12 r^2} - \frac{5 M_s H \pi a^4}{6 r} , \end{aligned} \quad (7)$$

where γ ($\text{J} \cdot \text{m}^{-2}$) is the domain wall surface energy. This can then be differentiated to get the curvature of the domain wall in its equilibrium state:

$$\begin{aligned} \frac{\partial \Delta E}{\partial r} &= 0 \\ r &= \frac{\gamma}{5 M_s H} \end{aligned} \quad (8)$$

The initial relative permeability, which is approximately equal to the initial susceptibility in ferromagnets, can be derived as follows:

$$\begin{aligned}\mu &\approx \lim_{\Delta H \rightarrow 0} \frac{\Delta M}{\Delta H} = \frac{2M_s \Delta V}{H} \\ &= \frac{25M_s^2 \pi a^4}{6\gamma} .\end{aligned}\tag{9}$$

By considering the contributions of domain wall bulging at the other pinning sites, a factor of $1/(2a)^2$ which arises from the surface pinning density should be included in Eq. 9. The initial permeability then becomes:

$$\begin{aligned}\mu &= \frac{25M_s^2 \pi a^2}{24\gamma} \\ &= \frac{25 M_s^2 \pi}{96\gamma} \rho^{-2/3} ,\end{aligned}\tag{10}$$

where $\rho = 1/(2a)^3$ is the number density of pinning sites.

The physical meaning of Eq. 10 is in agreement with observation: the higher the pinning density and surface energy, the less the domain wall will bend, and the less the initial permeability will be.

Initial Permeability as a Function of Carbon Content

Carbon steels can be heat treated to achieve a microstructure containing Fe_3C inclusions, where all of the carbide gathers into small spheroidal volumes which act as localized pinning sites. Assuming that the Fe_3C inclusions are distributed inside the material with average mass of carbon w , then the volume density of Fe_3C inclusion relates to its carbon weight percent (Wt%) as follows:

$$\frac{100\rho w}{\text{density of material}} = \text{Wt\%} \quad . \quad (11)$$

Therefore, the initial permeability of the material can be related to its carbon content, in terms of weight percent (Wt%), as follows:

$$\mu = C_1 \text{Wt\%}^{-2/3} \quad , \quad (12)$$

where C_1 is a constant.

In a real situation we need to consider other pinning sites such as dislocations in addition to the carbon inclusions. A parameter b , which represents the effect of these other types of pinning sites, can be introduced into Eq. 12, which then becomes:

$$\mu = C_1 (\text{Wt\%} + b)^{-2/3} \quad (13)$$

Data from the previous work of Jiles [4] are shown in Table 1. These were used to check the relation between carbon concentration and initial permeability. Agreement appears to be reasonable, as shown in Fig. 5.

Table 1. Magnetic properties of AISI carbon steel with spheroidised Fe_3C

Specimen	Wt% C	H_c (Oe)	B_r (G)	μ_{in} (G Oe ⁻¹)	W_H (ergs cm ⁻³)
1000	0.00	2.5	8500	350	12900
1020	0.20	6.5	13125	275	37900
1045	0.45	7.5	13375	200	40600
1080	0.85	9.0	10500	185	40400
1095	0.95	8.0	12000	170	49000

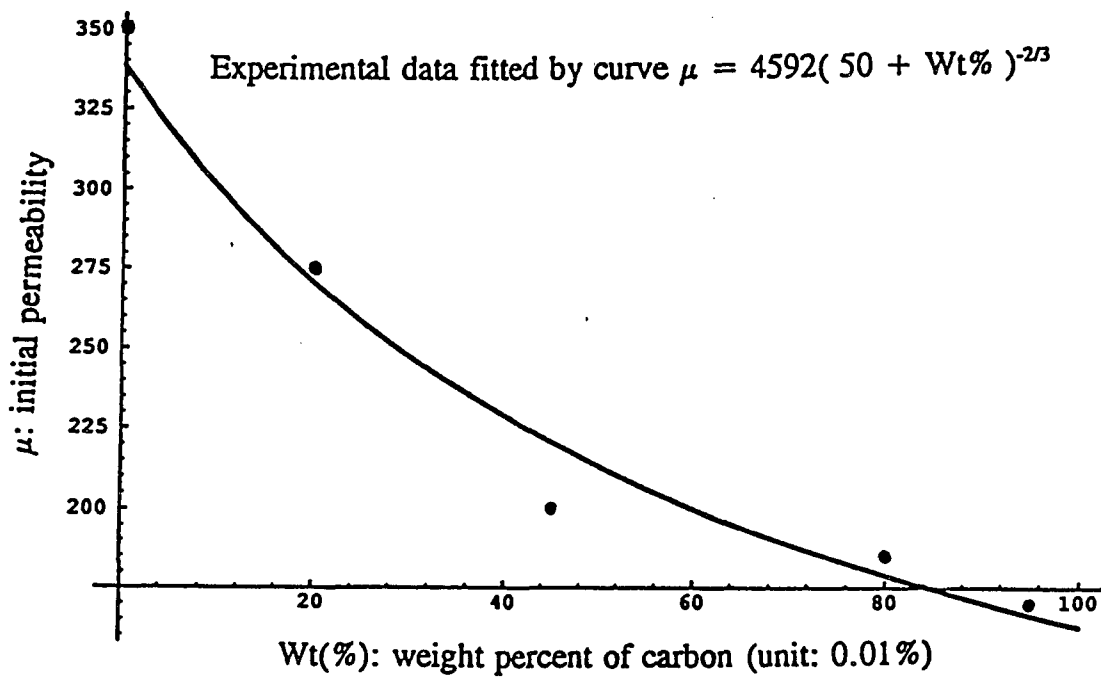


Fig. 5. Initial permeability as a function of Wt% of Carbon in steel with microstructure of spheroidised Fe_3C .

MODELLING OF MAGNETIC PROPERTIES USING THE THEORY OF HYSTERESIS

An alternative way of modelling structure sensitive magnetic properties is to use hysteresis modelling theory. Compared with direct modelling, this method gives the whole hysteresis curve, and therefore provides more complete information on magnetic properties. The critical issue is to select an appropriate model which has a strong underlying physical mechanism and which links microstructural features with hysteresis parameters, rather than a straight-forward mathematical curve fitting procedure.

Theory of Hysteresis

A physically based model with five modelling parameters developed by Jiles and Atherton [19-21], was found to be suitable for this purpose. This model is based on the idea of energy balance and assumes that the anhysteretic magnetization is the global equilibrium state of a magnetic system under an external field. For simplicity, domain wall motion (bending or translation) is considered as the mechanism for the magnetization process.

According to this model, the energy loss due to the irreversible change in magnetization can be expressed by the following equation (in CGS unit system):

$$E_{pin} = k \int_0^{M_{irr}} dM_{irr} \quad (14)$$

where the parameter k is a function of pinning strength and pinning density. As a result, the differential irreversible susceptibility can be expressed as:

$$\frac{dM_{irr}}{dH} = \frac{M_{an} - M_{irr}}{k\delta - \alpha(M_{an} - M_{irr})} \quad (15)$$

where α is a mean field parameter representing interdomain coupling, and δ is a directional parameter having the value +1 for $dH/dt > 0$ and -1 for $dH/dt < 0$.

Assuming that the reversible domain wall motion reduces the difference between the prevailing irreversible magnetization M_{irr} and the anhysteretic magnetization M_{an} at a given field strength, a parameter c is introduced which is determined by the domain wall surface energy, and relates the reversible change in magnetization to the displacement from the anhysteretic:

$$M_{rev} = c(M_{an} - M_{irr}) \quad (16)$$

Furthermore, this model employs a modified Langevin equation as an approximation for the anhysteretic curve. Therefore, the equation for anhysteretic magnetization becomes:

$$M_{an}(H_e) = M_s (\coth(H_e/a) - a/H_e) \quad (17)$$

where M_s is the saturation magnetization and the parameter a characterizes the shape of the anhysteretic magnetization. In fact $a = k_B T / \langle m \rangle$ where T is the temperature, $\langle m \rangle$ is the magnetic moment of an average domain in the material, k_B is Boltzmann's constant.

Modelling of Hysteresis Curves

The five mentioned parameters k , c , α , M_s and a , can be calculated by the inverse magnetic hysteresis modelling algorithm [22]. Magnetic hysteresis curves of AISI carbon steel with spheroidised Fe_3C inclusions were modelled. The hysteresis modelling parameters,

which act as the input to the model, are shown in Table 2. The modelled hysteresis curves, which are the output of the model, are shown in Fig. 6. For comparison, the structure sensitive magnetic properties, both measured and modelled are listed in Table 3 and Table 4 respectively. Results demonstrate a good agreement between model and measurement considering the simple hysteresis modelling algorithm used in the theory.

Table 2. Hysteresis parameters used to generated hysteresis curves shown in Fig. 6

Specimen	Ms (emu/cc)	a (Oe)	k (Oe)	alpha(Oe)	c
1000	1600	11.5	1.8	0.0016	0.65
1020	1600	10.8	4.6	0.0018	0.40
1045	1600	9.8	6.0	0.0017	0.35
1080	1600	12.3	9.8	0.0016	0.35
1095	1500	6.8	10.8	0.00085	0.32

Physical Interpretation of Hysteresis Modelling Parameters

In the hysteresis model used above, it is the pinning parameter k and the domain wall bowing parameter c that play important roles in the connection of hysteresis to microstructure. Therefore, correlations between these two parameters with microstructural features are keys to interpret structure sensitive magnetic properties. As the relationship between parameter c and microstructure has been discussed before [23], only k will be discussed here.

From Eq. 14, k is basically the coefficient between the energy loss upon pinning and

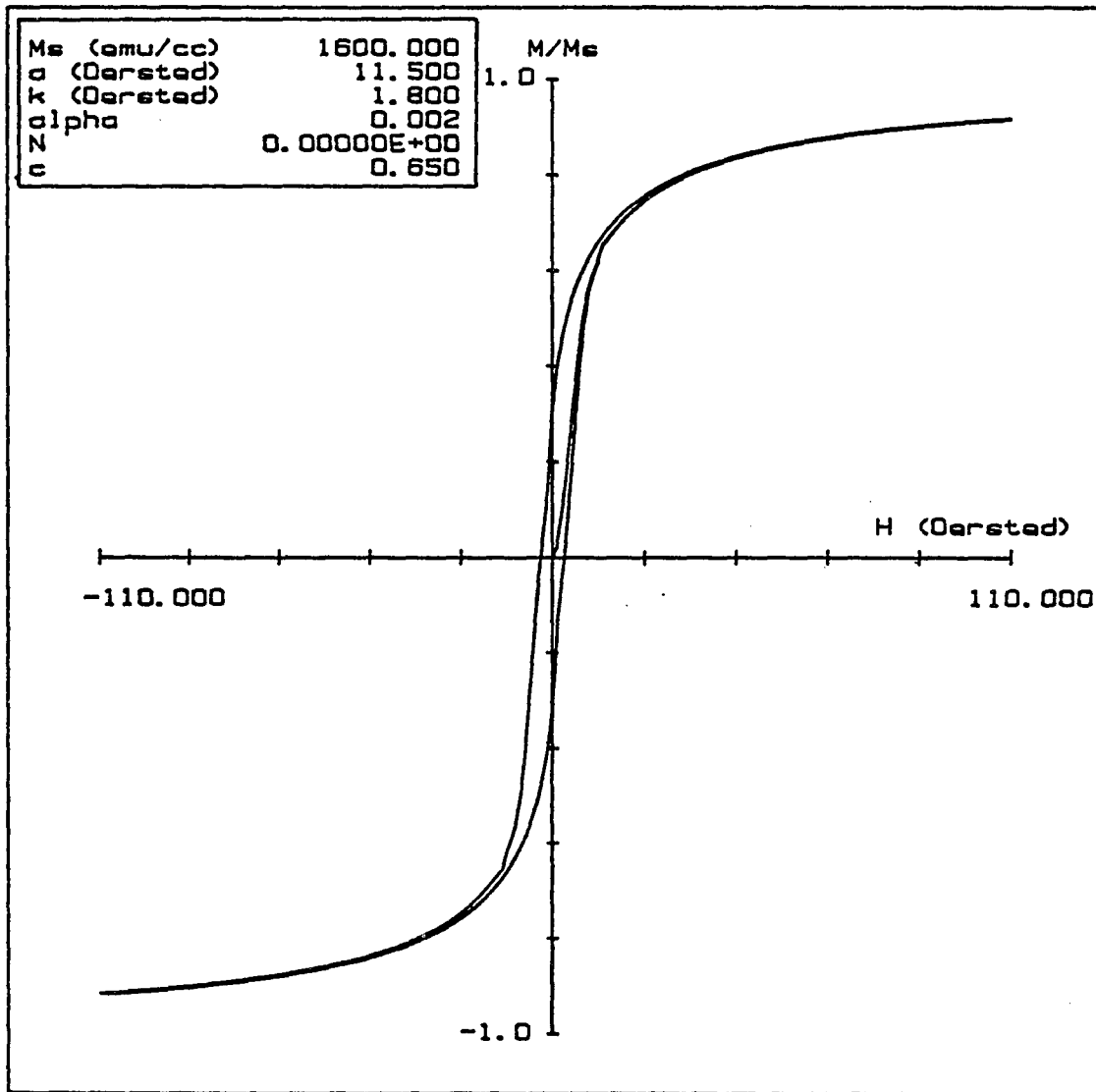


Fig. 6. Theoretical hysteresis loop modelled for (a) AISI 1000 carbon steel.

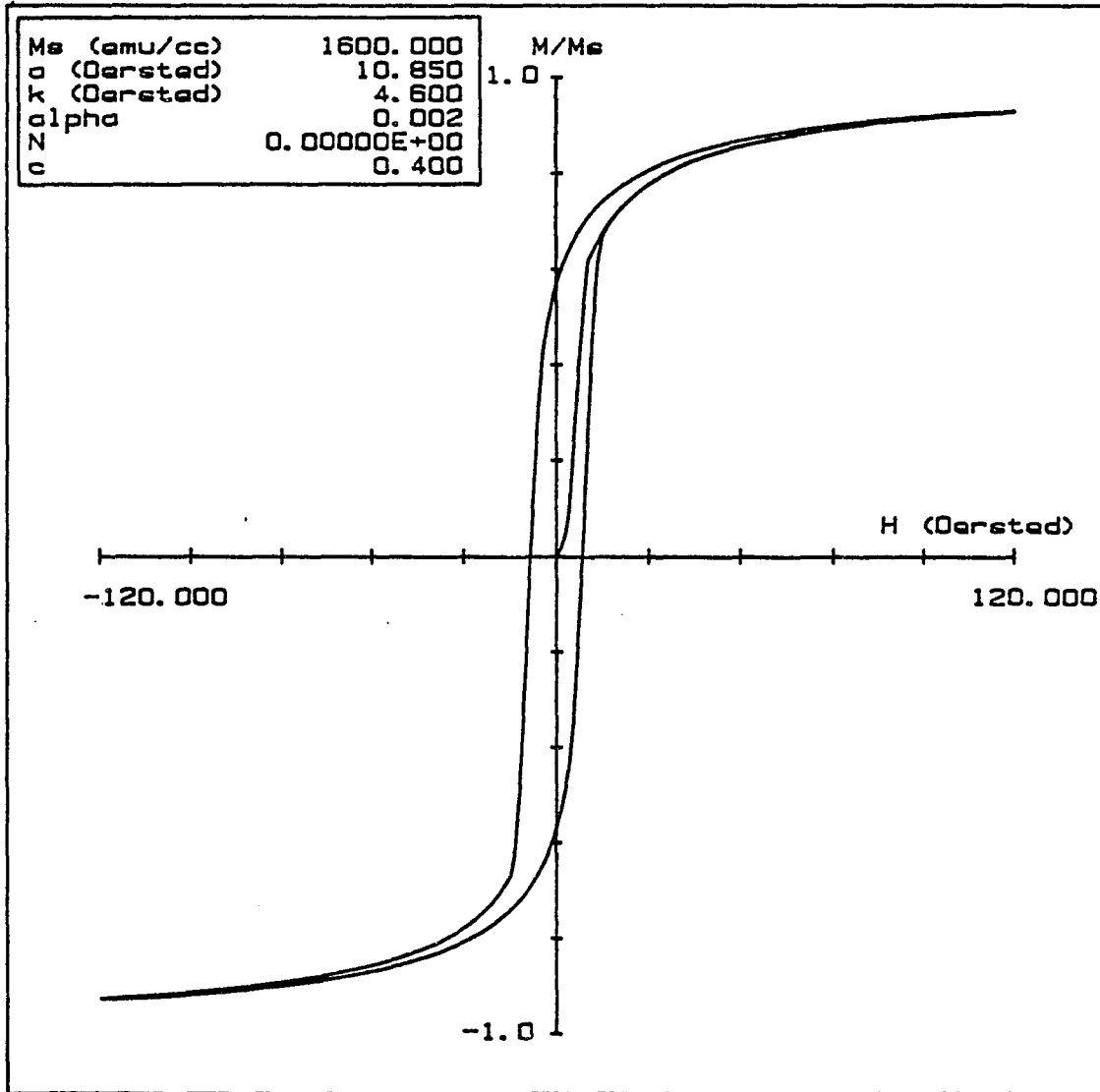


Fig. 6. (Continued) (b) for AISI 1020 carbon steel.

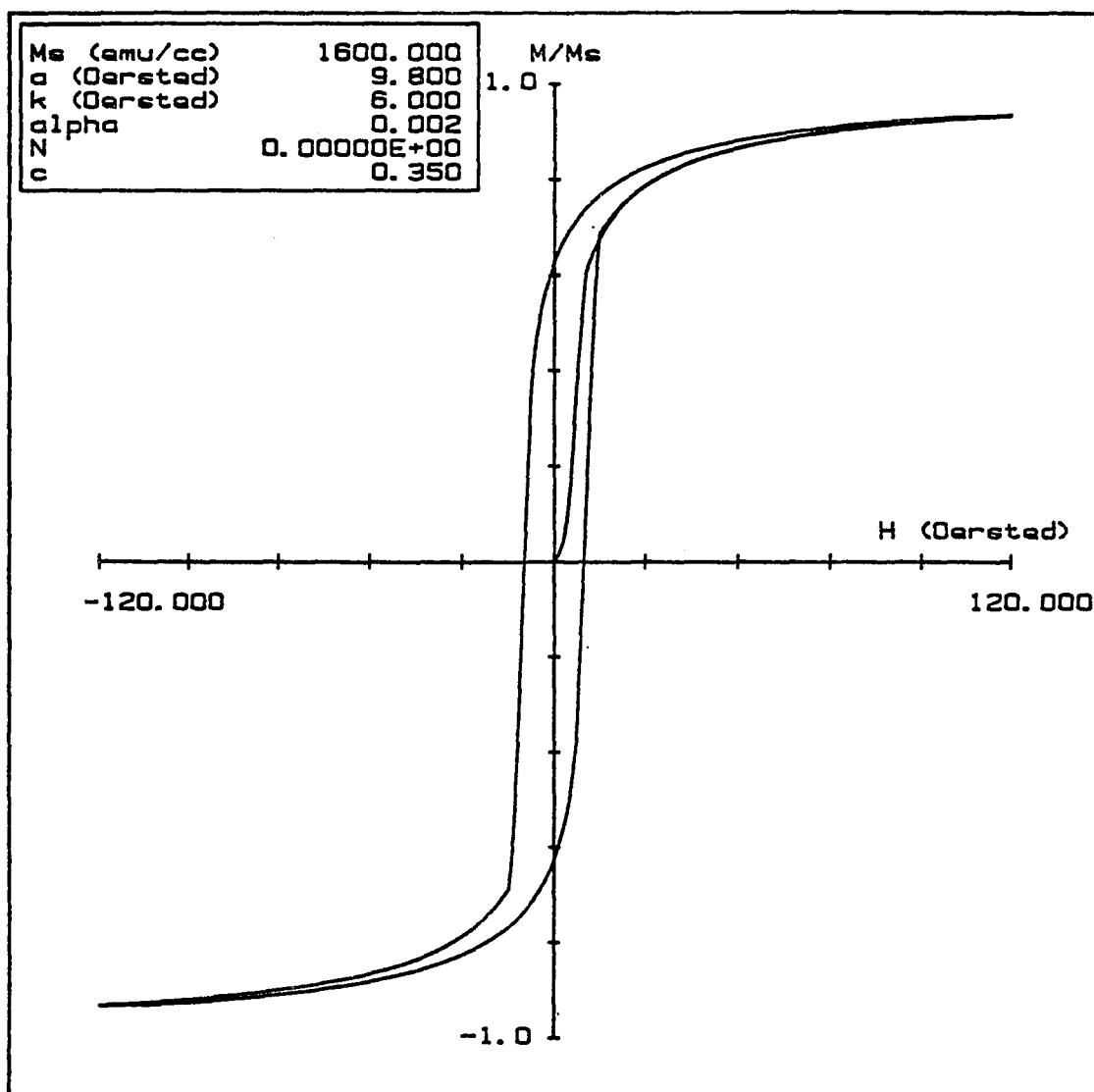


Fig. 6. (Continued) (c) for AISI 1045 carbon steel.

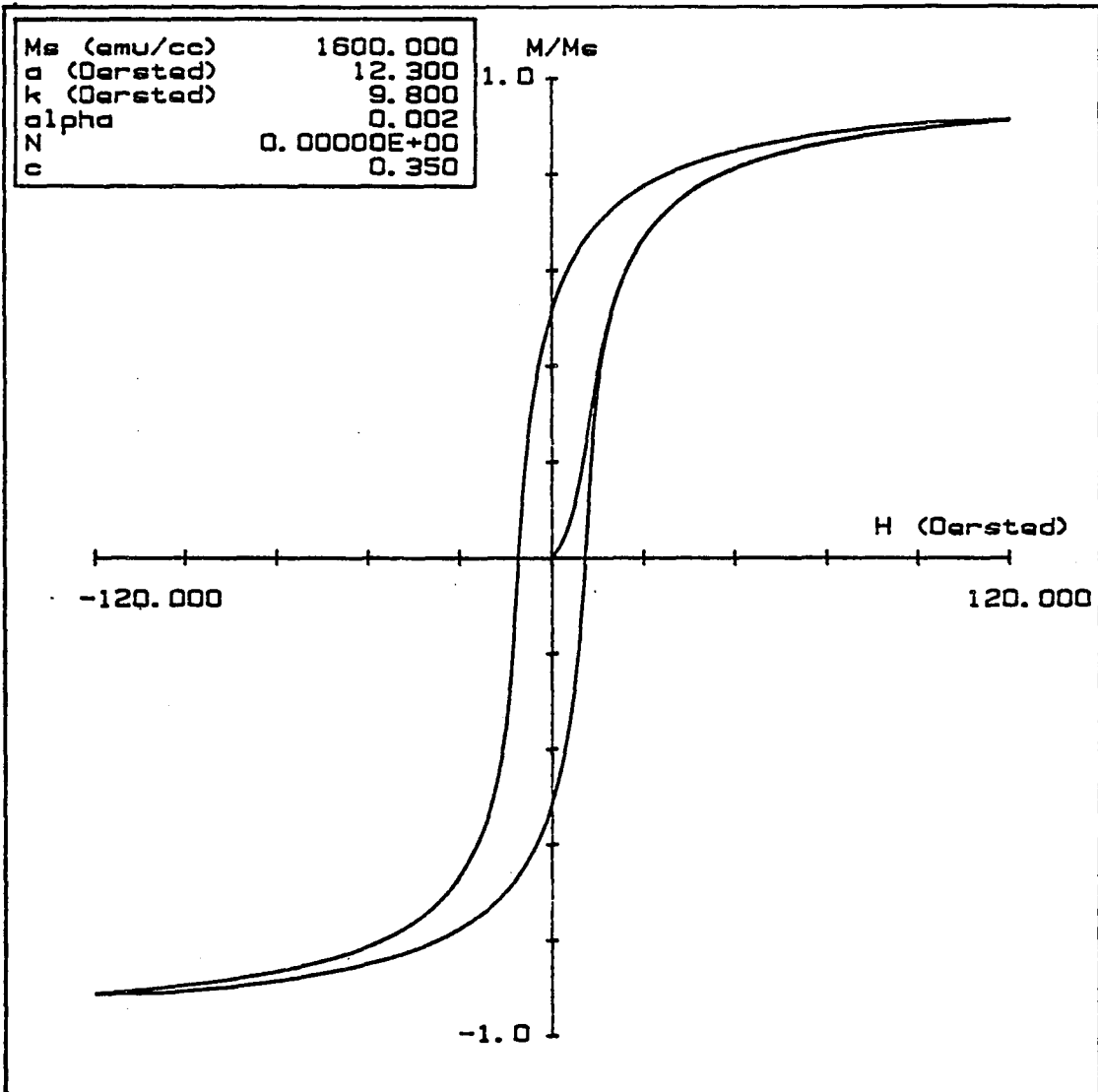


Fig. 6. (Continued) (d) for AISI 1080 carbon steel.

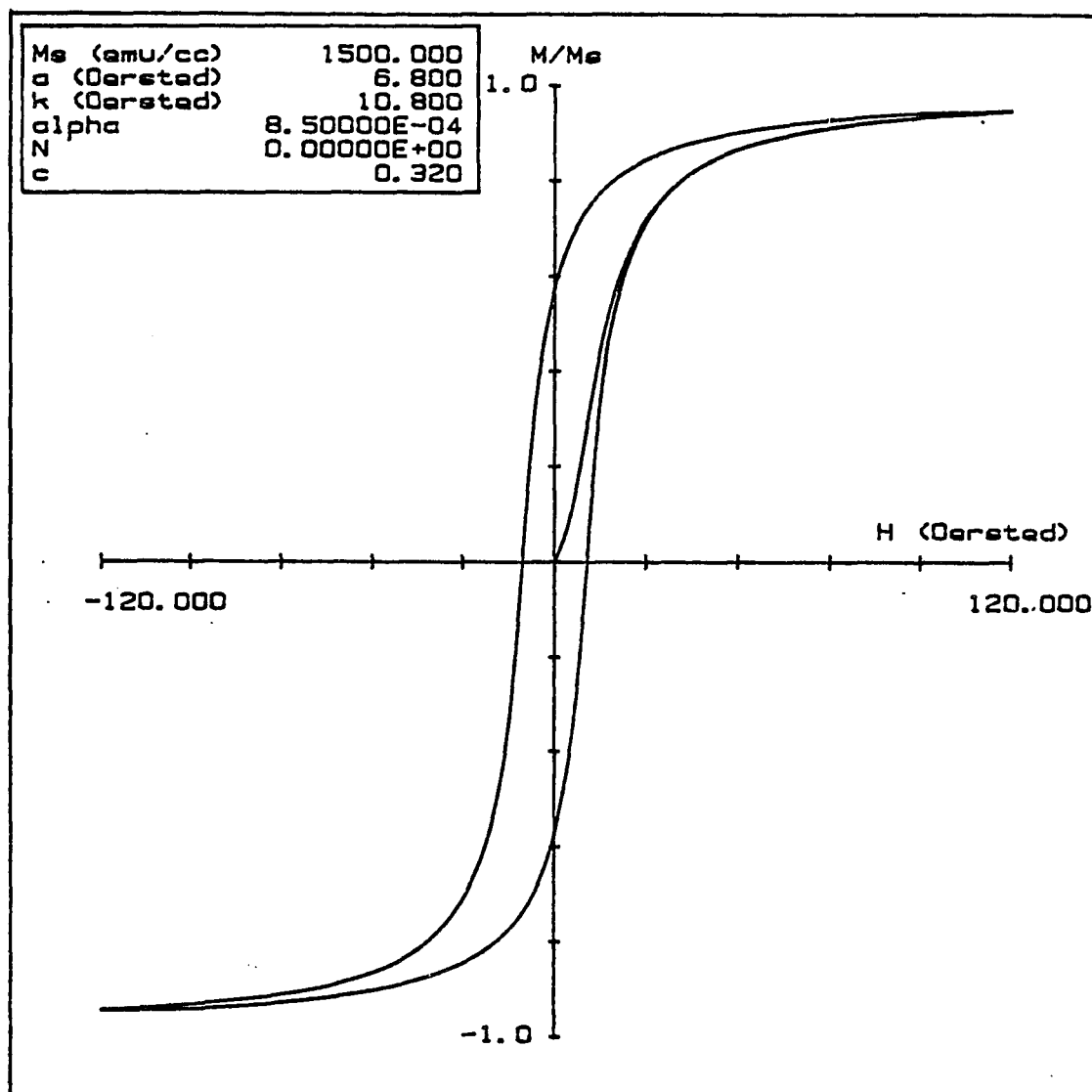


Fig. 6. (Continued) (e) for AISI 1095 carbon steel.

Table 3. Measured magnetic properties

Specimen	H_c (Oe)	M_r (emu/cc)	μ_{in} (G Oe ⁻¹)	W_H (ergs cm ⁻³)
1000	2.5	676	350	12900
1020	6.5	1044	275	37900
1045	7.5	1064	200	40600
1080	9.0	836	185	40400
1095	8.0	954	170	49000

Table 4. Modelled magnetic properties

Specimen	H_c (Oe)	M_r (emu/cc)	μ_{in} (G Oe ⁻¹)	W_H (ergs cm ⁻³)
1000	2.986	508	396	12230
1020	6.955	917	251	32086
1045	8.000	1005	243	39130
1080	8.910	827	192	46792
1095	8.691	864	297	48959

the irreversible magnetization achieved by the domain wall motion. According to Neel's theory [24], it is the magnetostatic energy associated with an inclusion that impedes the domain wall motion. Fig. 7 shows that when a naked magnetic inclusion is totally enclosed within the body of a domain, it has free poles attached, with an magnetostatic energy of $8\pi^2M_s^2r^3/9$. When a domain wall bisects it, the distribution of the free poles changes and results in a reduction of the magnetostatic energy to $4\pi^2M_s^2r^3/9$. Therefore, when a domain wall overcomes a pinning site, the amount of energy $4\pi^2M_s^2r^3/9$ is lost.

According to this physical picture of domain wall pinning by point defects, and considering only 180° domain wall motion, the pinning parameter k can be calculated as follows. When domain walls sweep over an unit volume of the material, the change of magnetization is $2M_s$, while the energy lost at pinning sites is $4\rho\pi^2M_s^2r^3/9$, and where ρ is the defect density. Therefore,

$$k = \frac{4\rho\pi^2M_s^2r^3}{9} \frac{1}{2M_s} \quad (18)$$

$$k = \frac{2\rho\pi^2M_s r^3}{9}$$

Again, in carbon steel with a microstructure containing spheroidised Fe_3C inclusions, if we assume they are distributed uniformly inside material with average size and mass, then k can be related to the carbon weight percent (Wt%) as follows:

$$k = C_2 \text{ Wt}\% + C_3 \quad (19)$$

where C_2 and C_3 are constants. C_3 represents the effect of pinning due to defects other than

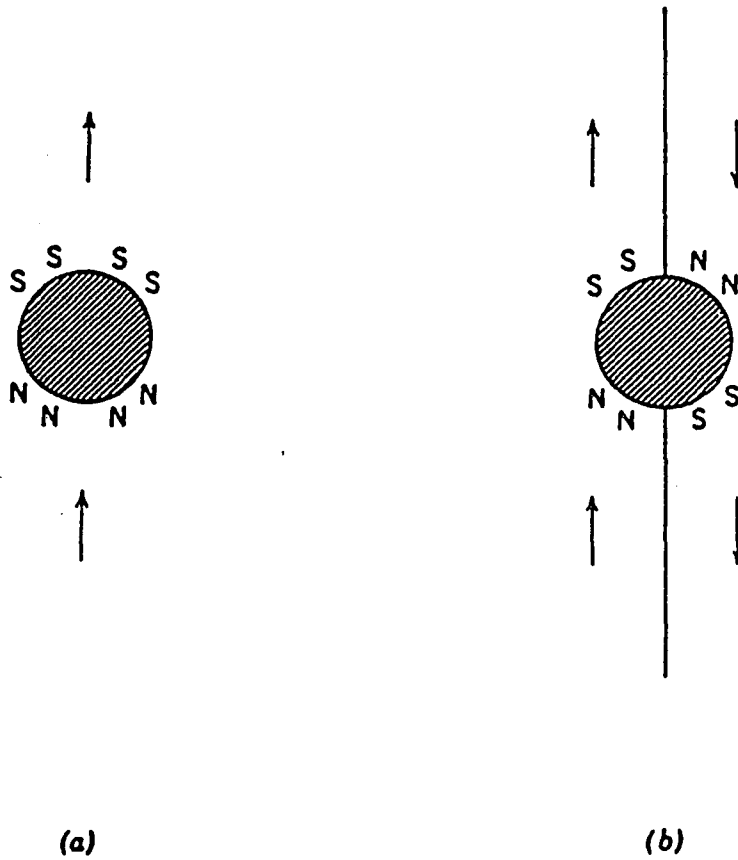


Fig. 7. (a) Free-pole distribution on a naked inclusion, (b) reduction of magnetostatic energy associated with an inclusion when intersected by a domain wall.

Fe_3C inclusion. Fig. 8 shows the relation between parameter k and carbon weight percentage of the plain carbon steel specimens. The result is reasonable, as carbon weight percentage increases, the pinning parameter k of the model also increases.

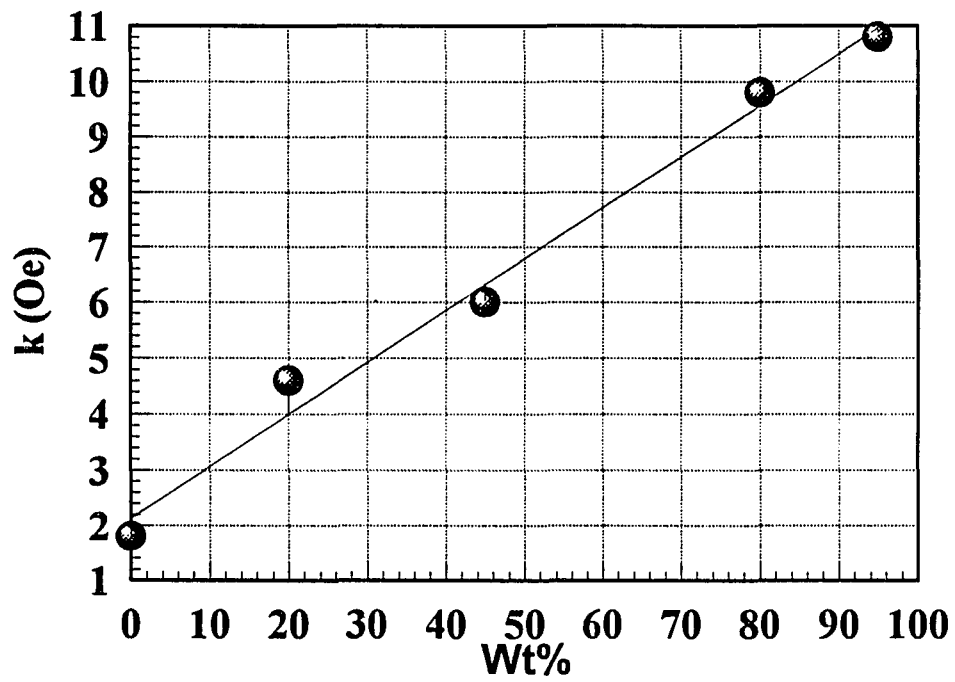


Fig. 8. Pinning parameter k as a function of carbon weight percentage.

CONCLUSIONS

The interactions between domain walls and point defects have been modelled in this paper. As a result, initial permeability has been derived as a function of pinning density and other domain parameters. Hysteresis theory has also been used to model structure sensitive magnetic properties. By developing relationships between hysteresis parameters and microstructure, the hysteresis theory described here can be used as a link between microstructure of materials and their global magnetic properties. In this paper, the hysteresis parameter k as a function of point defect density and other magnetic properties has been derived. By treating spheroidised Fe_3C inclusions in carbon steel as an example of a microstructure with localized defects, the relationship between initial permeability μ_{in} , pinning parameter k and carbon weight percentage $\text{Wt}\%$ were studied and tested against experimental result.

REFERENCES

- [1] M.F. Litmann, IEEE Trans. Mag. MAG-7, 48 (1971).
- [2] D.C. Jiles, NDT International, 21, 311 (1988).
- [3] D.C. Jiles, NDT International, 23, 83 (1990).
- [4] D.C. Jiles, J. Phys D: Appl. Phys., 21, 1186 (1988).
- [5] D.C. Jiles, J. Appl. Phys. 63, 2980 (1988).
- [6] R.Ranjan, D.C. Jiles and P.K. Rastogi, IEEE Trans. Mag. MAG-23, 1869 (1987).
- [7] S. Habermehl, D.C. Jiles and C.M. Teller, IEEE Trans. Mag. MAG-21, 1909 (1985).
- [8] D.C. Jiles, C.V. Owen and W.A. Spitzig, J. NDE, 6, 119 (1987).
- [9] J. Sternberk, E. Kratochvilova, J. Hrebik and A. Gemperle, Phys. Stat. Sol.(a) 79, 523 (1983).
- [10] A. Seeger, H. Kronmuller, H. Rieger and H. Trauble, J. Appl. Phys. 35(3), 740 (1964).
- [11] P.Gaunt, Phil. Mag. B, 48(3), 261 (1983).
- [12] H.-R. Hilzinger and H. Kronmuller, Physics Letters, 51A, 59 (1975).
- [13] H.R. Hilzinger and H. Kronmuller, J. Magn. Magn. Mater. 2, 11 (1976).
- [14] David Jiles, Introduction to Magnetism and Magnetic Materials (Chapman & Hall, New York, 1991), Chapter 7 and Chapter 8.
- [15] B. Astie, J. Degauque, J.L. Porteseil and R. Vergne, IEEE Trans. Mag. MAG-17, 2929 (1981).
- [16] Rayleigh and Lord, Phil. Mag. B, 23, 225 (1887).
- [17] R. Beckerand W. Doring, Ferromagnetismus (Springer, Berlin, 1938).

- [18] M.A. Rahman, M. Poloujadoff, R.D. Jackson, J. Perrard and S.D. Gowda, IEEE Trans. Mag. MAG-17, 3253 (1981).
- [19] D.C. Jiles and D.L. Atherton, J. Mag. Mag. Mater. 61, 48 (1986).
- [20] M.J. Sablik, G.L. Burkhardt, H. Kwun and D.C. Jiles, J. Appl. Phys. 63, 3930 (1988).
- [21] K.H. Carpenter, IEEE Trans. Mag. MAG-27, 4404 (1991).
- [22] D.C. Jiles, J.B. Thoelke and M.K. Devine, IEEE Trans. Mag. MAG-28, 27 (1992).
- [23] D.C. Jiles, "Physical interpretation of the hysteresis parameters in the theory of hysteresis: domain wall deformation model", present at the 37th Annual Magnetism & Magnetic Materials Conference, Houston, November 1992.
- [24] L. Neel, Cahiers de Phys., 25, 21 (1944).

PART II.

**MAGNETIC HYSTERESIS MEASUREMENT IN THE DETECTION
OF EFFECTS OF THE FATIGUE**

INTRODUCTION

Fatigue is a material degradation process in which materials are cyclically stressed resulting in progressive microstructural changes and leading to catastrophic failure. It has been estimated that fatigue failure is the primary cause of at least 90% of all service failures due to mechanical causes. Present knowledge of the mechanisms of metal fatigue have been summarized by Laird [1]. On a microscopic scale, plastic deformation arises as dislocations form bundles and later cell walls. Since localized inhomogeneities such as plastic deformation can act as stress concentration, micro fatigue cracks initiate when external stress or strain exceeds a certain threshold. Then upon further load cycles, fatigue- induced micro cracks grow into a macroscopic crack. Later the macro crack continues to grow until it reaches a critical length for which the next load peak produces tensile failure. Present NDT methods in detecting fatigue failure are mainly related to the detection of macroscopic cracks which generally appear in later stages of the fatigue life when the component is already close to failure. Hence, in order to detect fatigue damage in its early stage, the ideal NDE technique should be able to monitor dislocation structures as well as nucleation and propagation of cracks.

It is well known that when a ferromagnetic material is magnetized, its magnetization processes, and hence its magnetic properties, are strongly influenced by its microstructural features, including dislocation tangles, grain boundaries, inclusions and micro cracks. Therefore magnetic NDE techniques such as hysteresis measurement [2] and Barkhausen effect measurement [3] are believed to be the ideal NDE techniques in the detection of

fatigue damage in ferromagnetic materials, because these methods depend on the inherent magnetic properties of steels for material evaluation. Early in the 1940s, Wlodek [4] and Cavanagh [5] began to study fatigue by observing the changes in voltage induced in a search coil surrounding the test specimen. In the 1950s, Vicena [6] calculated the interaction potential between a domain wall and a dislocation. In the 1960s, Salkin [7] studied structural changes of steel during the first 1000 fatigue cycles by measuring their magnetodynamic properties. Ilescu [8] studied the fatigue limit in carbon steels by using a magnetic viscosity technique. In the 1970s, Schumann [9] reported for the first time the measurements of coercive force within a single load cycle in the saturation stage of the fatigue hardening curve. Murghrabi et al [10] studied the dislocation structure of ferromagnetic material during strain controlled cyclic deformation by measuring magnetic properties. In the 1980s, Shah and Bose [11] and Bose [12] studied the change of magnetic properties during whole fatigue life and found a correlation between variation of magnetic properties and load condition. Sanford-Francis [13,14] used the changes in magnetic properties with stress cycling to predict remaining fatigue life. In 1990s, Demkin [15] estimated dislocation density in fatigue cycled polycrystalline nickel by measuring coercivity.

Parallel to the development of magnetic hysteresis measurement in fatigue detection, Barkhausen effect measurement techniques have also been reported in this study. In the 1970s, Karjalainen and Moilanen [16] and Karjalainen et al. [17] detected minor plastic deformation during tensile and cyclic loading by measuring Barkhausen a noise signal. McClure et al. [18] studied fatigue crack growth by correlating the Barkhausen effect with acoustic emission. Matzkanin and Gardner [19] measured residual stress by using Barkhausen

noise analysis. In the 1980s, Karjalainen and Miolanen [20] found that the changes observed in the shape and area of Barkhausen noise versus stress could be used to detect fatigue softening and hardening in mild steel. Titto [3] reviewed Barkhausen noise techniques for fatigue detection and summarized their possible uses in (1) detection of the effect of elastic and plastic strain/stress, (2) detection of the effect of cyclic strain on variation of Barkhausen noise in single strain cycle, (3) detection of overloading, and (4) detection of stress relaxation.

In spite of all this previous work, there is a lack of basic understanding of the variation in microstructure-sensitive magnetic properties with fatigue damage. In recent years a large magnetic NDE technology program has been developed at the Center for NDE at Iowa State University. The effects of fatigue on the magnetic properties have been studied systematically [21-24]. The present paper reports on the most recent investigations of a study of microstructural changes due to fatigue damage in A533B nuclear reactor pressure vessel steels and corresponding changes in magnetic properties, using magnetic hysteresis methods. The ultimate objective of this investigation is to develop a suitable NDE method to monitor the remaining fatigue life of structural steel components.

EXPERIMENTAL

Materials and Specimens

The material used in this investigation was a medium strength structural alloy (*ASTM* code *A533B*) whose chemical composition is given in Table 5. Smooth fatigue specimens in an "hour glass" shape with 6 mm diameter in the center and 64 mm gauge length, parallel to the rolling direction, were machined from the material. The geometry of the sample is shown in Fig. 9. The geometry of the sample was designed so that the fatigue damage will always be most severe in the center of the specimen, which allows an easy magnetic NDE inspection for investigation of fatigue effects.

Mechanical Tests

Tensile tests to determine the strength characteristics of the material were performed at room temperature on two samples by a computer controlled Instron tensile test machine, Model 4505. Tensile test results of engineering strain-stress are shown in Figs. 10 - 11. Rockwell hardness tests were performed on broken pieces of these two samples by a Rockwell Hardness Tester, Model 3JR. Test results of average values are shown in Table 6.

Fatigue Tests

Fatigue tests were carried out on smooth tensile specimens using a computer controlled, 20KIPS, servo hydraulic MTS system together with an MTS Extensometer

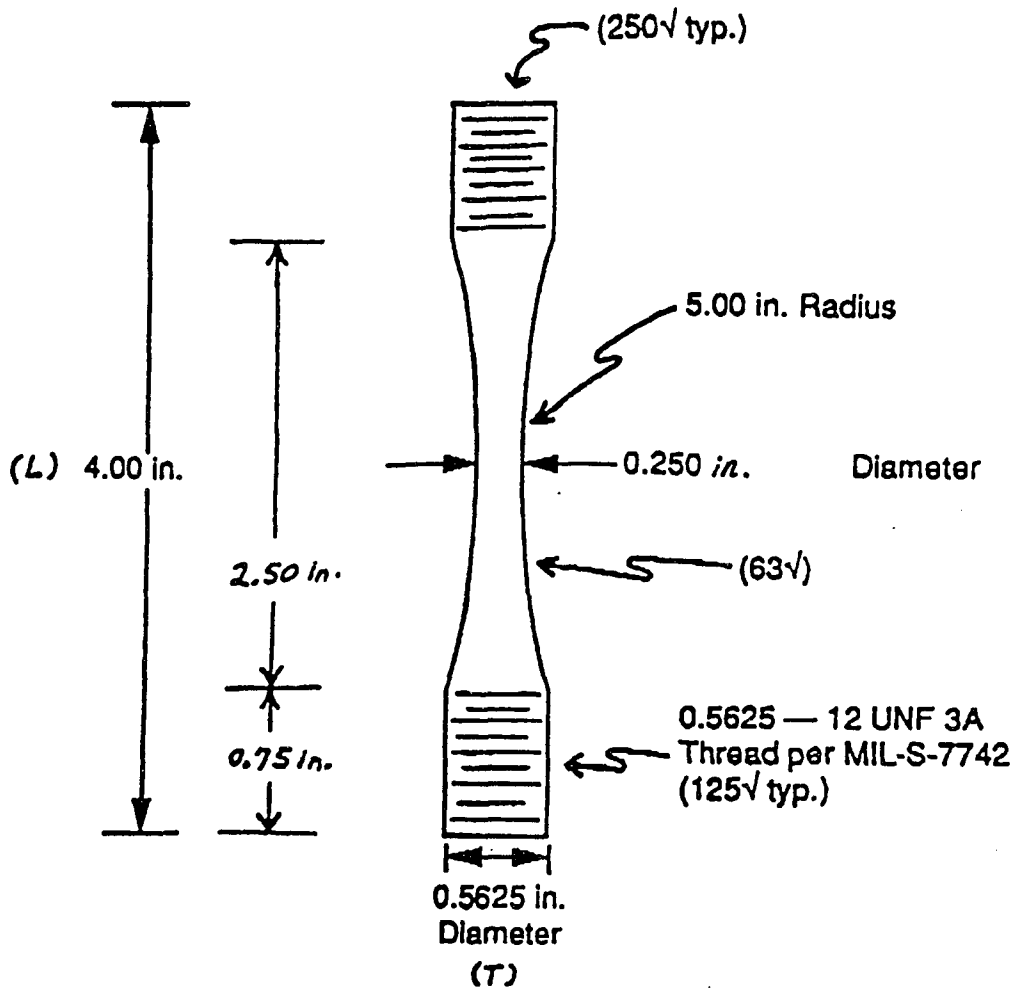


Fig. 9. Diagram of fatigue specimen.

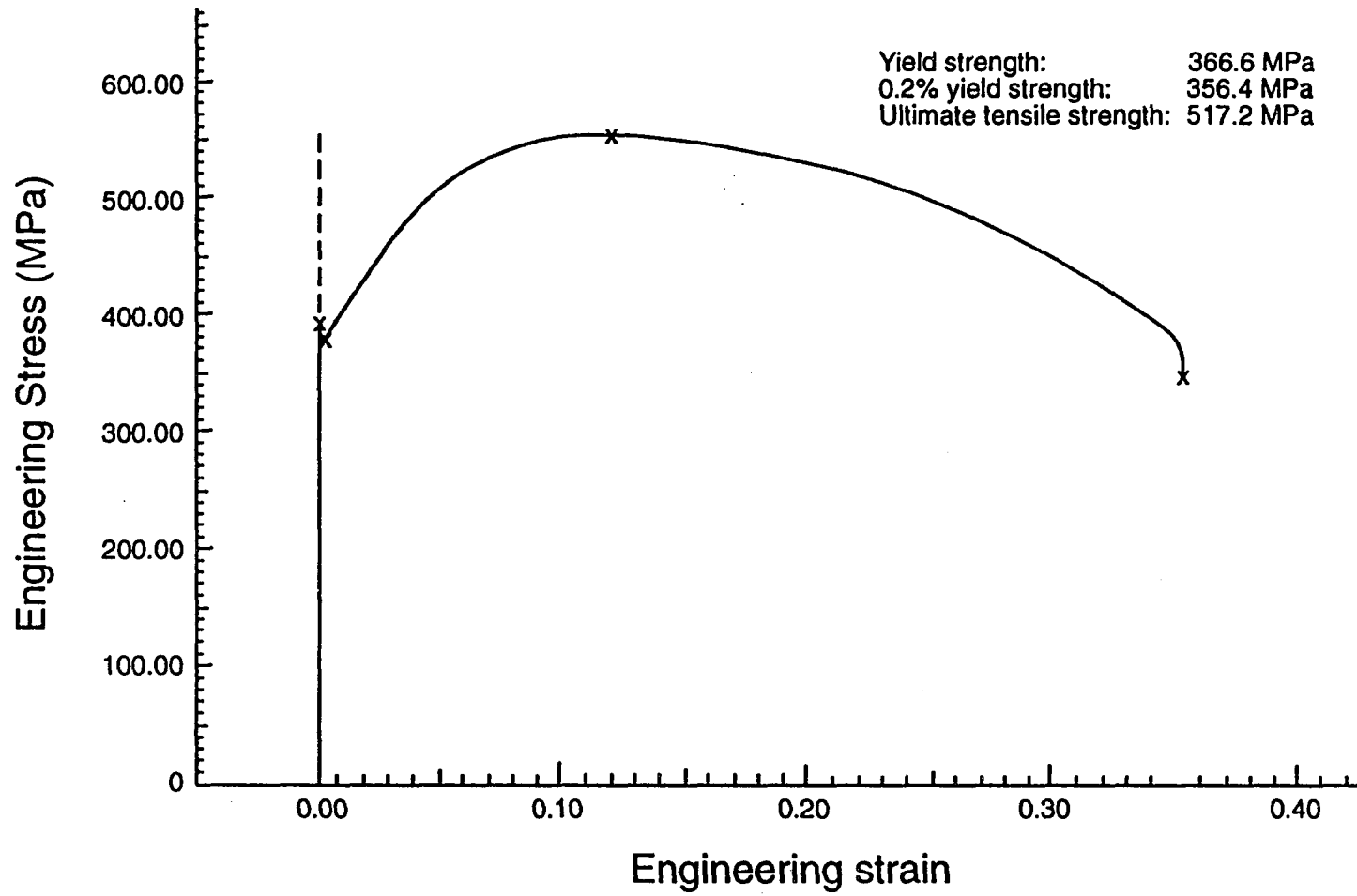


Fig. 10. Engineering strain-stress curve for Sample 1.

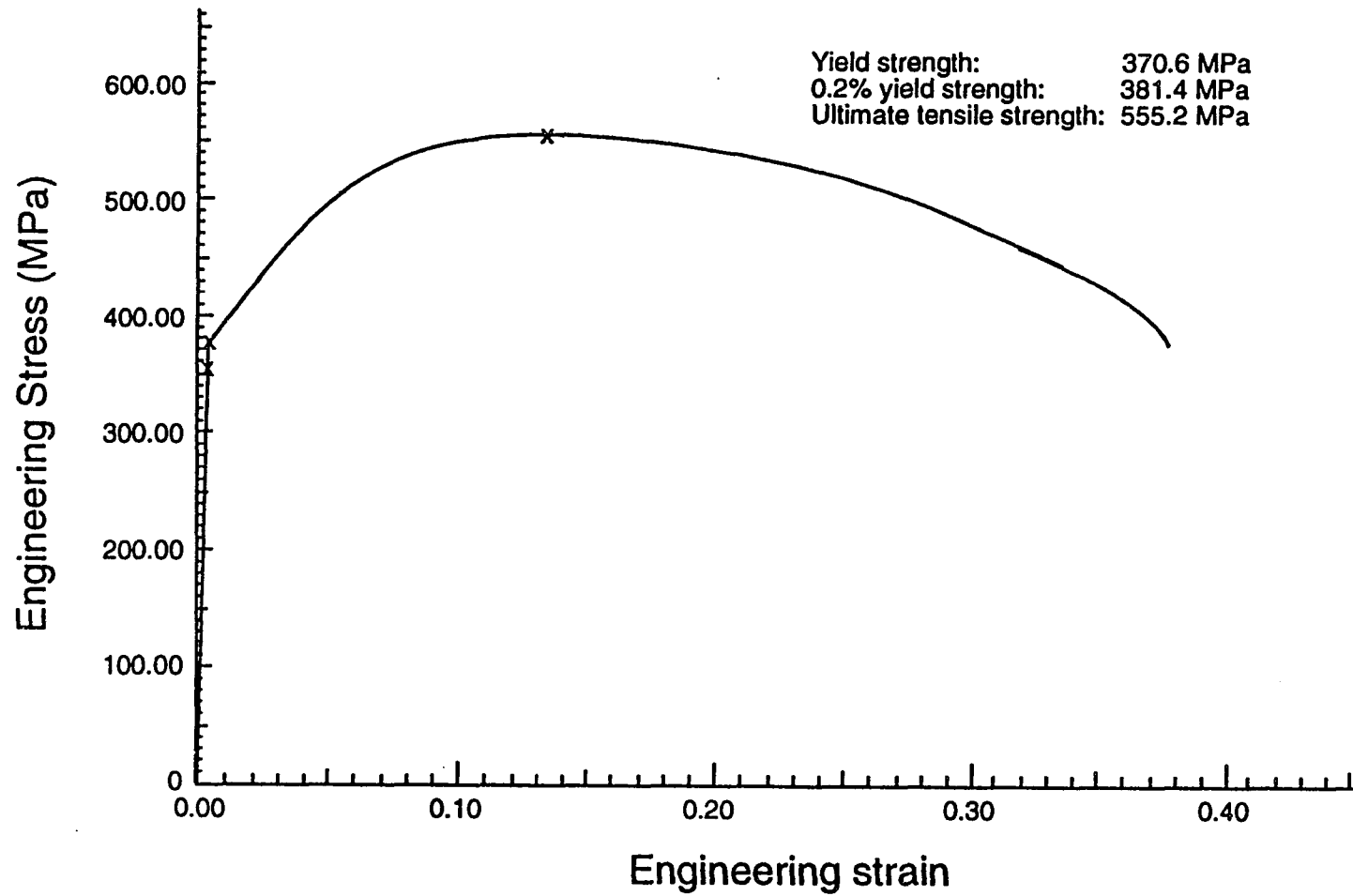


Fig. 11. Engineering strain-stress curve for Sample 2.

Table 5. Chemical composition of A533B steel

Element	Wt %
C	0.2
Mn	1.5
Ni	0.7
Cr	0.6
Mo	0.6
Si	0.2
P	0.035
S	0.04
Fe	Bal

Table 6. Mechanical properties of *ASTM A533B* steel

Young's modulus (GPa)	170
0.2% yield stress (MPa)	369
Ultimate tensile strength (MPa)	536
Hardness R _b	88

(Model 632.26B-21) at a frequency of 1-4 Hz. The unit was interfaced with data acquisition and control cards via a personal computer. The software was designed to carry out fatigue tests under load or strain amplitude control as well as to record load and strain data. Also the software was modified to start the fatigue cycle with an up-stroke and end up with a down-stroke in order to maintain a fixed external stress condition for magnetic inspection during fatigue interrupt.

Initial tests were performed at various strain levels from 0.0015 to 0.007. Later, the strain amplitude of 0.003 was chosen as a convenient condition for a systematic study of low cycle fatigue in strain control condition, and stress amplitude between 200 - 300 MPa was chosen for the study of high cycle fatigue in load control condition. Fatigue tests were also performed on prestrained specimens with pre-strain level from 0.008 to 0.021 to study the initial mechanical condition on both fatigue behavior and the magnetic properties of the material.

Inspection Head

A specially designed inspection head was made in this study for in situ magnetic property measurement. The core of the inspection head was made of Armco iron, a soft magnetic material, and its geometry was designed so that the demagnetization factor of the test magnetic circuit could be minimized by a good physical contact of the probe with the test tensile specimen. A power coil and a flux coil were wound on the inspection head to provide the magnetizing field and to measure the flux density inside the probe respectively. A Hall probe was used to measure the magnetic field on the surface of the test material. This

was carefully mounted on the inspection head so that the Hall probe was located at the center of the test sample. The configuration of the inspection head is shown in Fig. 12.

Magnetic Measurements

The magnetic properties were measured in situ by interrupting the fatigue test at predetermined intervals in the fatigue life without taking the tensile specimen off the MTS fatigue machine. (The intervals were chosen at either linear or logarithmic increments). Magnetic hysteresis measurement were taken under quasi d.c. conditions using the Magnescope [25], a portable magnetic inspection system, which consisted of a personal computer, a gaussmeter, a fluxmeter and a bipolar programmable power supply. An inspection head which was connected to the Magnescope, measured both magnetic flux density and magnetic field. The measurement procedures involved an initial demagnetization procedure followed by a hysteresis loop magnetization routine [26]. This routine acquired a single hysteresis loop from which most of the magnetic parameters such as initial permeability, coercivity, remanence and hysteresis loss were calculated.

Metallurgical Study

Metallurgical study consisted of scanning electron microscopy (SEM) examination and optical microscopy examinations. The SEM analysis of fatigue mechanism was performed by inspecting the surface conditions of test specimens at different stages of fatigue life. Electro polished samples were used for this study. Both surface replicas and actual specimens were studied under SEM. The SEM machine used in this study was Cambridge S-200. The

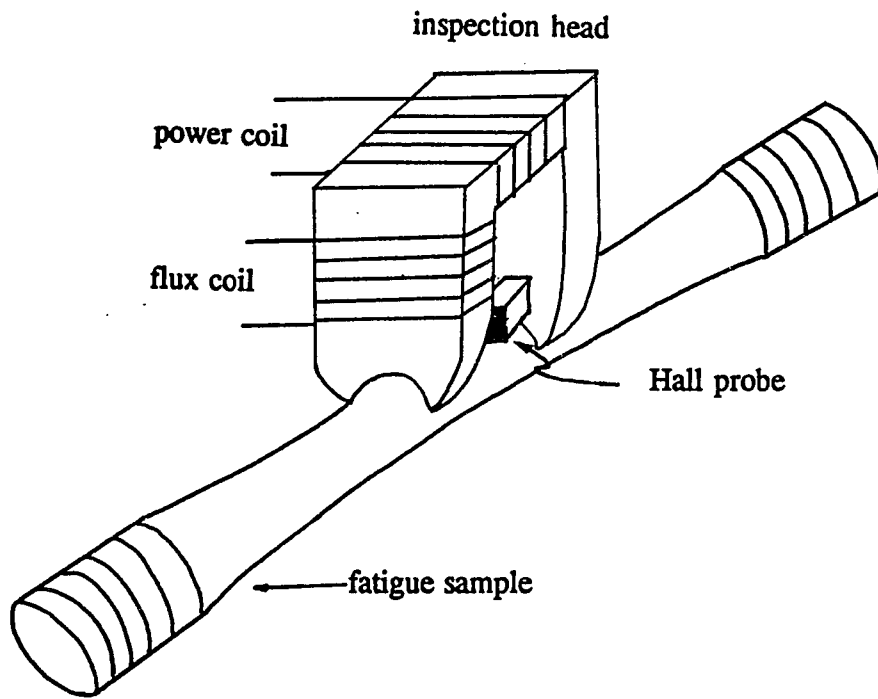


Fig. 12. Configuration of inspection head.

optical microscope analysis was performed to study the microstructure of the material under Zeiss 47 56 60-9902. The sample was prepared by mechanical polishing followed by chemical etching.

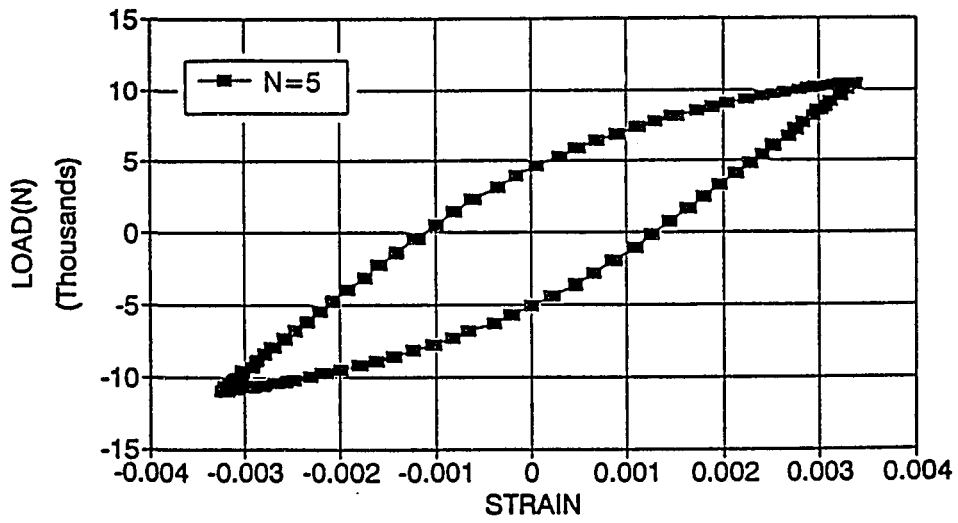
RESULTS AND DISCUSSIONS

Fatigue Analysis

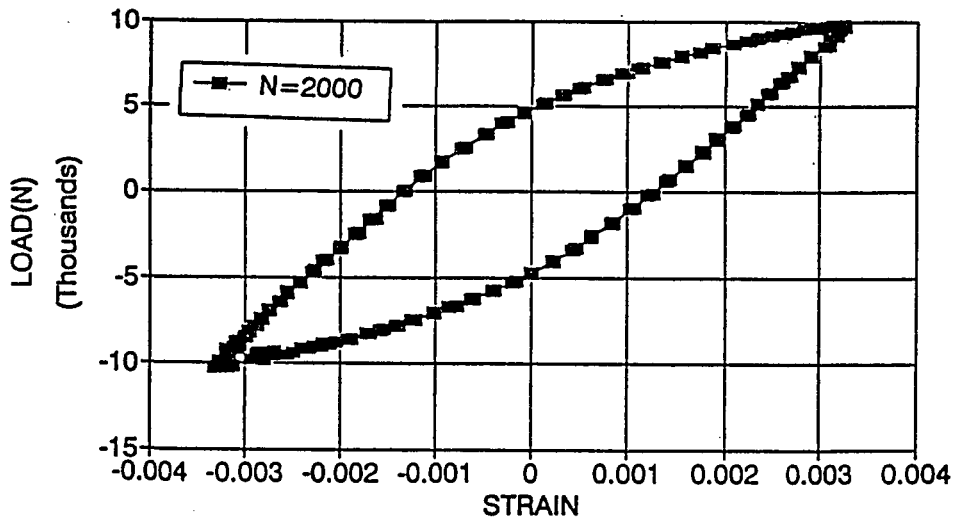
Fatigue life has been defined as the number of cycles needed for either complete failure of the specimen in load-control fatigue tests or over 50% decrease in load in strain-controlled fatigue tests.

During fatigue tests, the load and strain data were continuously recorded. Due to the formation of stable micro cracks at the later stages of fatigue life, a decrease in load level in strain-controlled fatigue tests and an increase in the strain data for load controlled fatigue tests usually occurred as a result of loss of stiffness. This information was recorded to compare with magnetic measurements in order to identify the source of variation in magnetic parameters and thus to study the sensitivity of magnetic NDE technology for fatigue damage evaluation.

Also, during fatigue tests, the mechanical hysteresis loops of stress versus strain were obtained for a single stress cycle at a predetermined number of fatigue cycles. These loops could be used to determine whether the fatigue test was conducted under low cycle fatigue or high cycle fatigue, and could also be used to find the onset of the formation of a macro crack by observing the distortion of the loop. A series of mechanical hysteresis loops for Sample EP05 with strain amplitude of 0.003 are shown in Fig. 13. It can be seen that under strain amplitude of 0.003, mechanical hysteresis occurred very early in the fatigue life and this implied that it was under a low cycle fatigue. As the distortion of the S-N curve was observed at the fatigue cycle of 16,000 it was believed that a macro crack had formed and

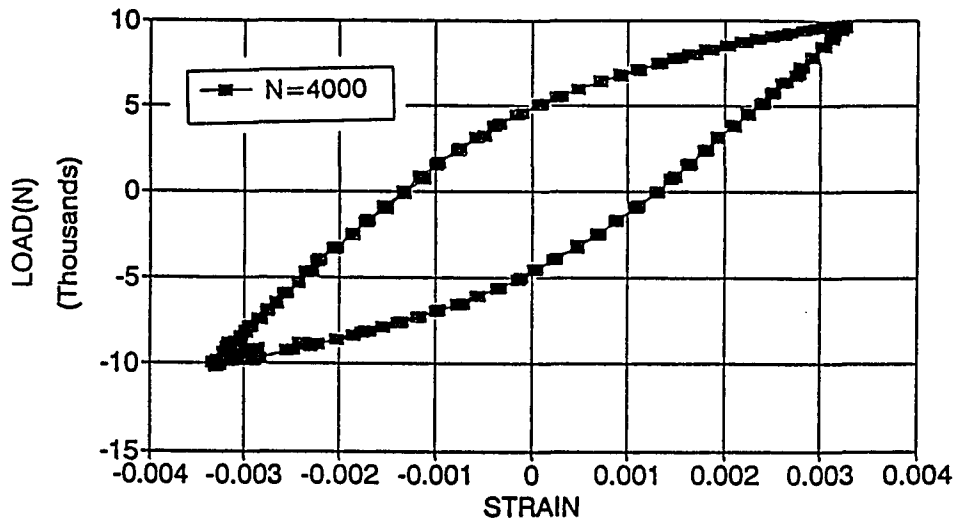


(a)

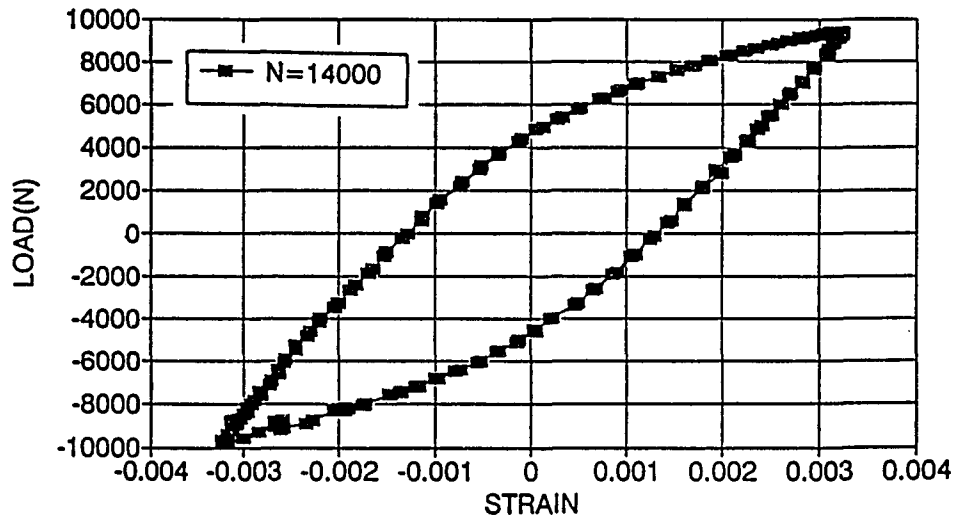


(b)

Fig. 13. Load-strain curve for Sample EP05 at fatigue cycle of (a) $N=5$ and (b) $N=2,000$.

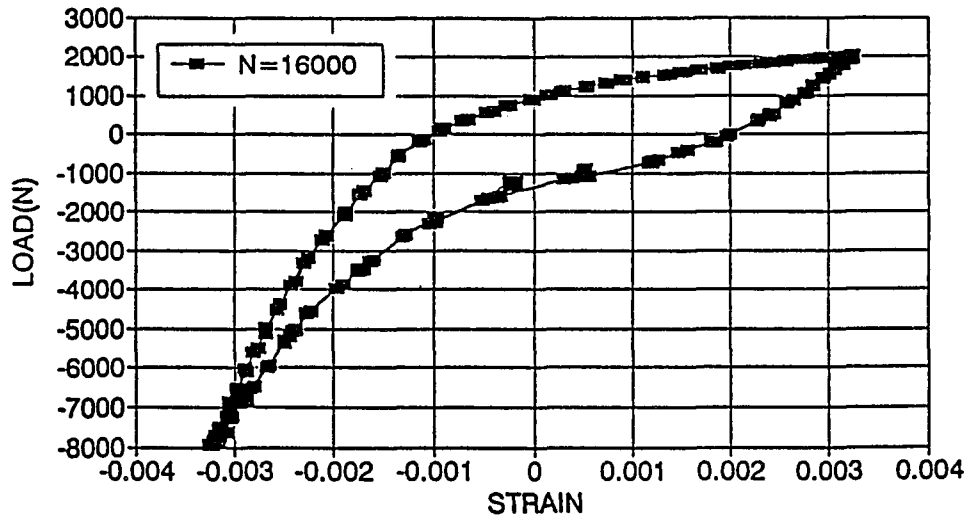


(c)

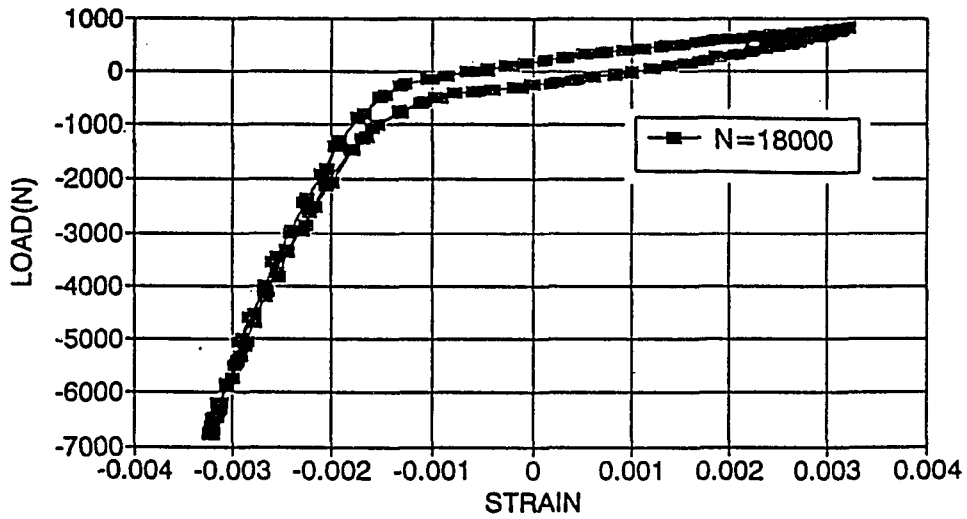


(d)

Fig. 13. (Continued) (c) $N=4,000$ and (d) $N=14,000$.



(e)



(f)

Fig. 13. (Continued) (e) N=16,000 and (f) N=18,000.

propagated before 16,000 stress cycles.

Magnetic Hysteresis Measurement

The magnetic hysteresis technique, under dc conditions, is a bulk property measurement. The magnetic parameters, such as coercivity, remanence, initial permeability and maximum differential permeability are sensitive to microstructure and bulk stress.

Low cycle fatigue: The strain amplitude of 0.003 was chosen as a convenient condition for systematic study of the effects of low cycle fatigue on magnetic properties. At this strain level, plastic strain was evident from the mechanical hysteresis curve (See Fig. 13) and the fatigue life was typically around 15,000 cycles. Test result of magnetic hysteresis parameters as a function of fatigue life are shown in Figs. 14 - 15 for specimen EP11. Similar results for Specimens EP09 and EP10 are shown in Figs. 16 - 19.

It can be seen that the coercivity decreased moderately in the early stages of fatigue life, as a result of fatigue softening. Then the coercivity and other magnetic properties remained quite stable over most of the fatigue life. This stable region amounted to 80-90% of the lifetime. Finally in the last 10-20% of fatigue life, the magnetic parameters changed dramatically. According to the load profile, the final stage which corresponded to the formation of a macro crack, was accompanied by a decreasing load that was needed to obtain the constant strain amplitude. It was expected that the microstructure would be stable after the initial fatigue softening. The invariance of the magnetic parameters throughout the intermediate range of fatigue life was consistent with such an interpretation.

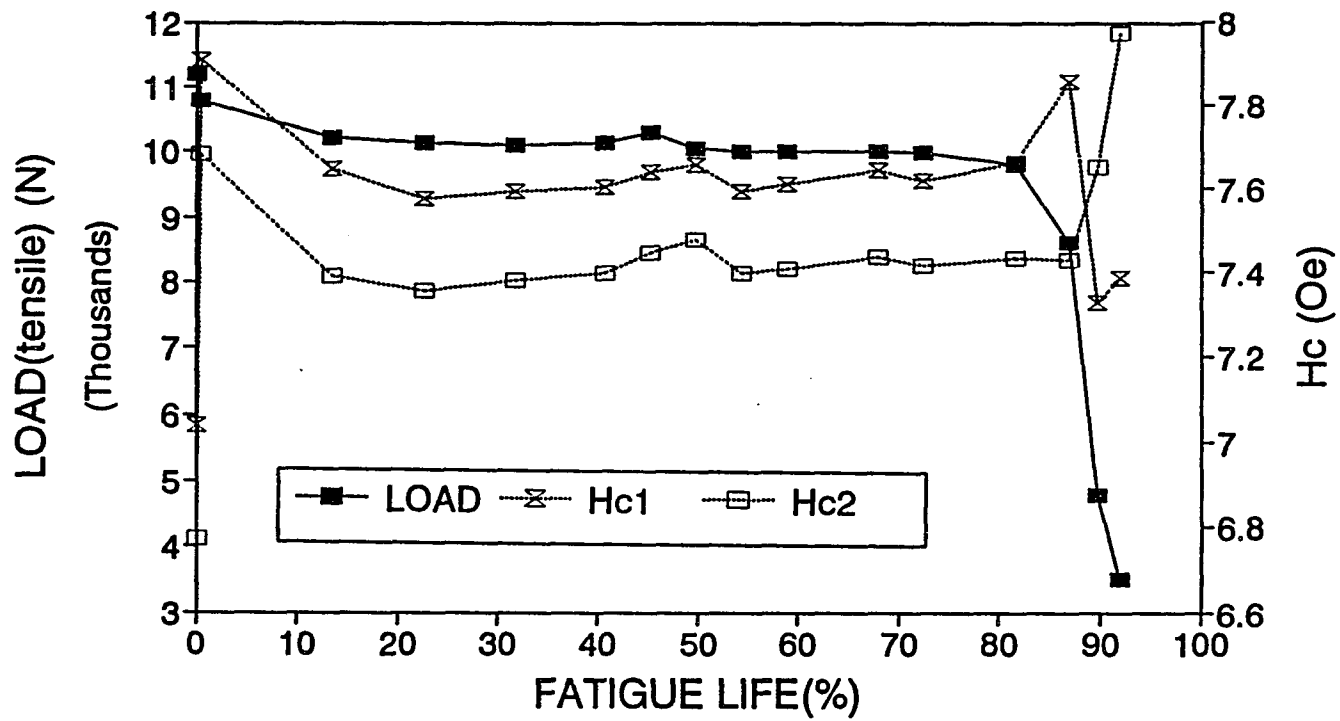


Fig. 14. Variation of tensile load and coercivity with expended fatigue life for Sample EP11 under fatigue test with strain amplitude of 0.003.

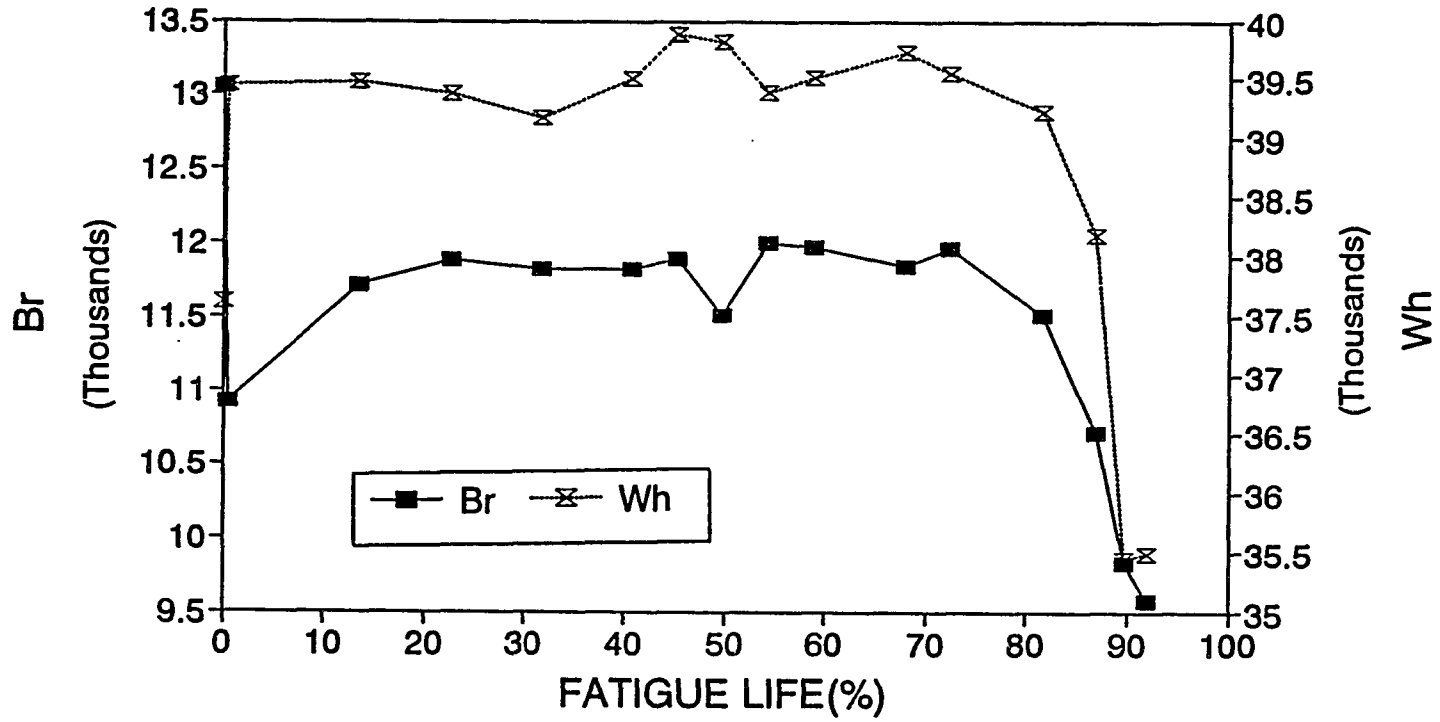


Fig. 15. Variation of remanence and hysteresis loss with expended fatigue life for Sample EP11 under fatigue test with strain amplitude of 0.003.

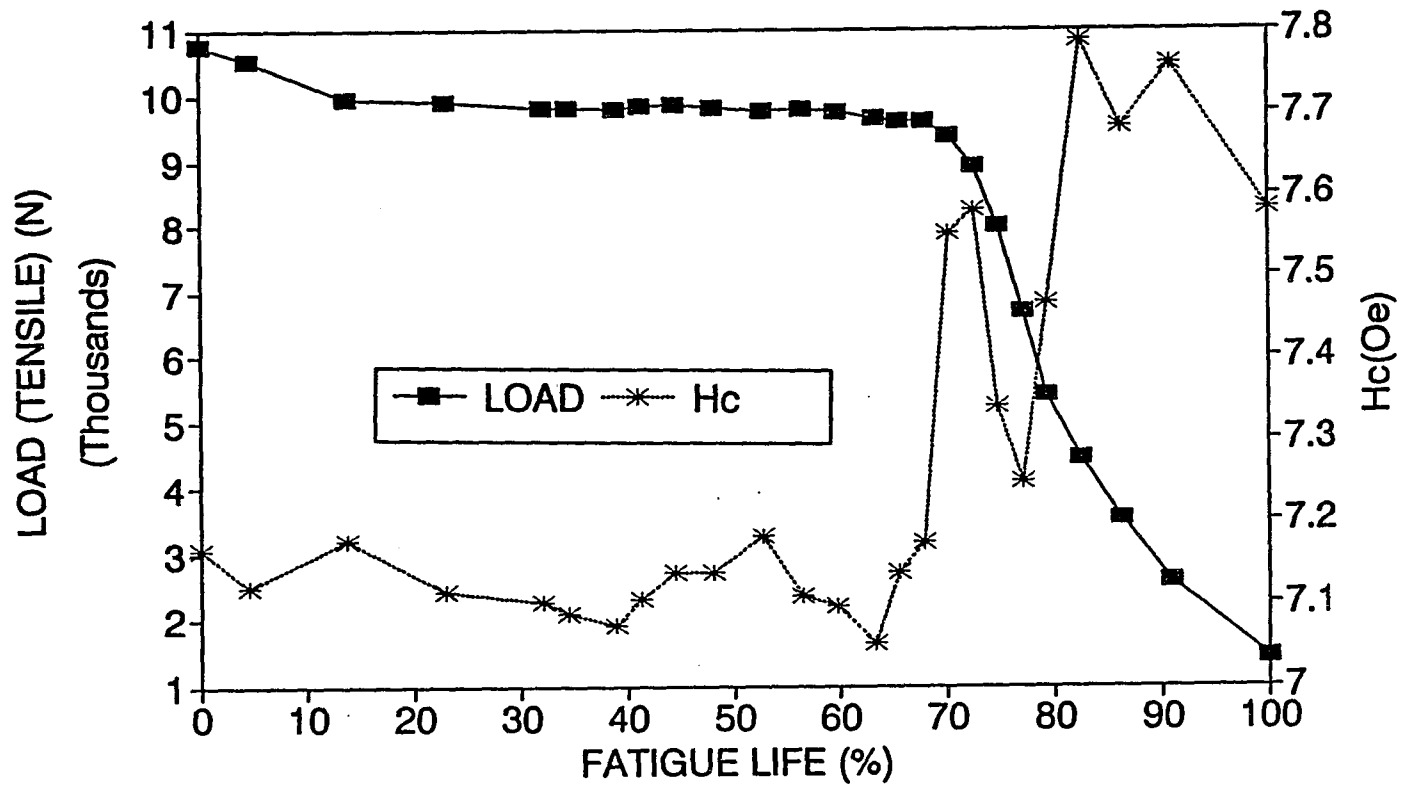


Fig. 16. Variation of tensile load and coercivity with expended fatigue life for Sample EP09 under fatigue test with strain amplitude of 0.003.

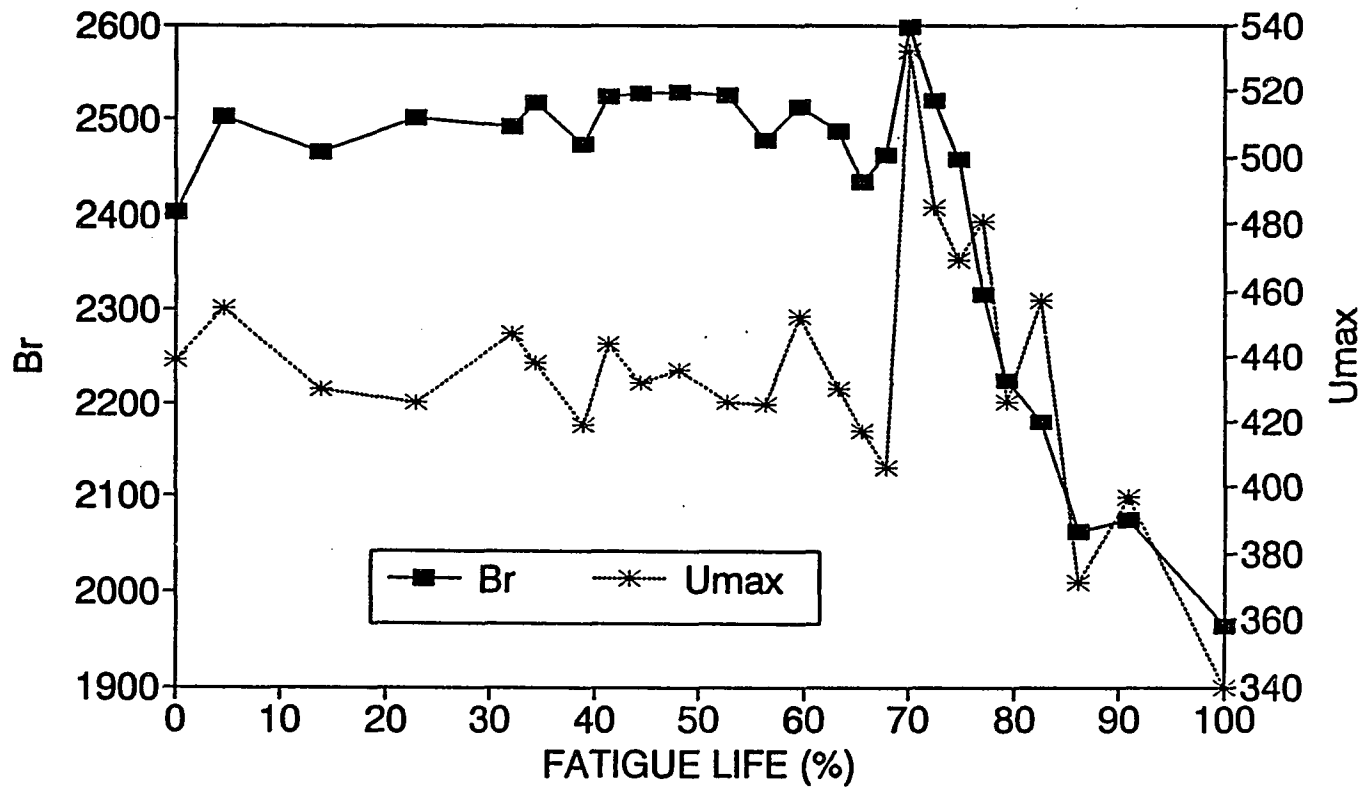


Fig. 17. Variation of remanence and maximum permeability with expended fatigue life for Sample EP09 under fatigue test with strain amplitude of 0.003.

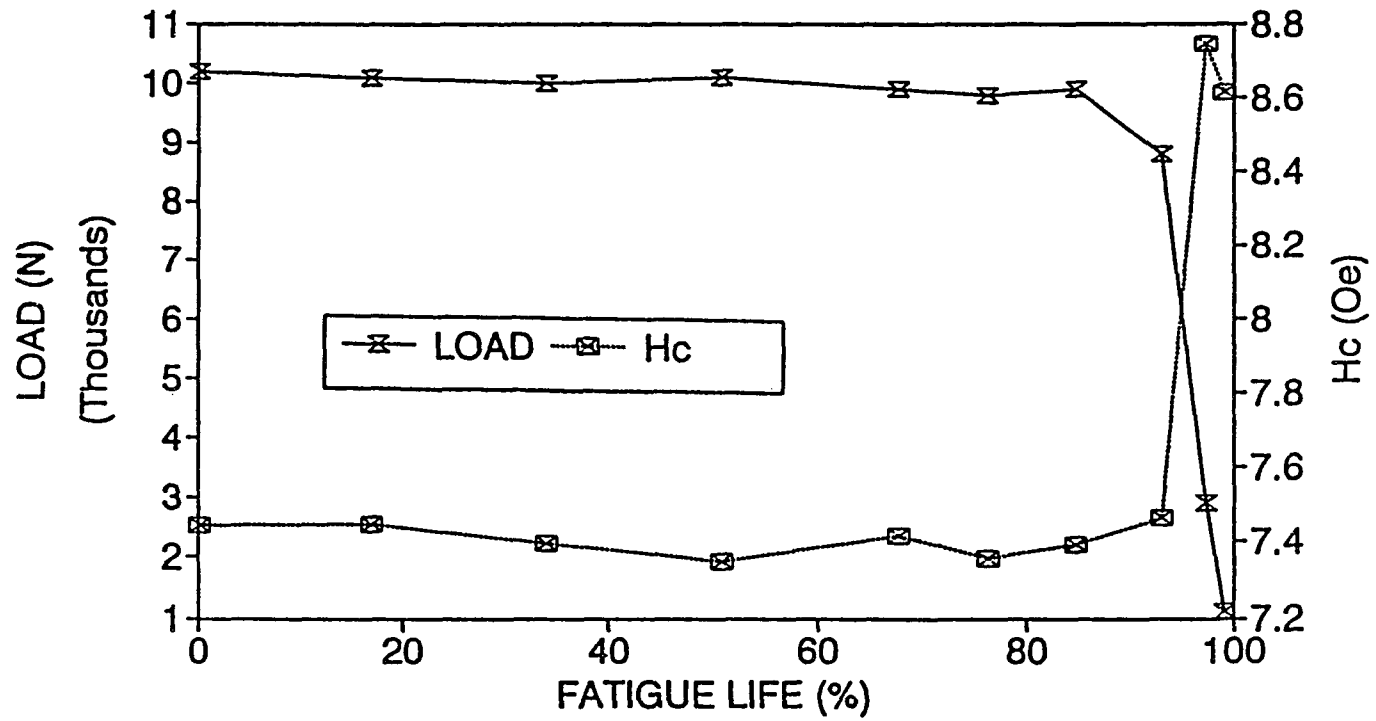


Fig. 18. Variation of tensile load and coercivity with expanded fatigue life for Sample EP10 under fatigue test with strain amplitude of 0.003.

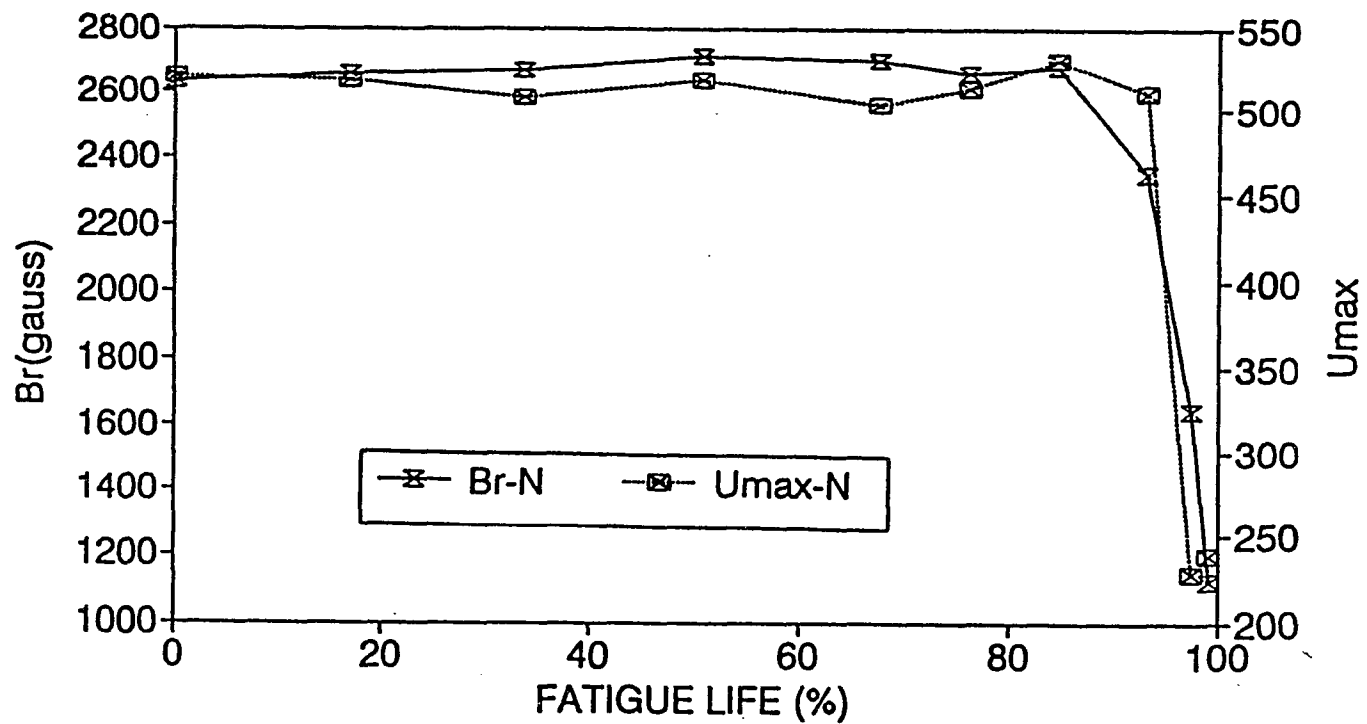


Fig. 19. Variation of remanence and maximum permeabilitytensile with expended fatigue life for Sample EP10 under fatigue test with strain amplitude of 0.003.

The variation of magnetic parameters in the later stages of fatigue were mainly caused by changes in the reluctance of the magnetic circuit due to macro cracking of the test material. The formation of the macro cracks in the magnetic circuit increased the magnetic reluctance and this was responsible for the decrease in coercivity, remanence and other magnetic parameters. However, if the Hall probe was located at the crack, the leakage field could bring about an apparent increase in coercivity.

A close look at load profile indicated that even in the intermediate region of fatigue life, there is a slight decrease in load amplitude. This can be explained by the fact that cyclic stressing introduced micro cracks at stress concentration centers and resulted in a decrease in material stiffness. The formation of micro cracks at this stage has been shown by SEM analysis.

High cycle fatigue: High cycle fatigue studies were conducted under load controls condition at different stress amplitudes. Magnetic properties were measured at pre-determined numbers of fatigue cycles throughout the expended fatigue life. A test result at stress level of 272 MPa is shown in Figs. 20 - 21. It was found that, unlike strain-controlled fatigue tests, the magnetic properties changed continuously even after initial fatigue softening. Coercivity appeared to be the most useful parameter for monitoring the progress of fatigue.

Further fatigue tests showed that during load-controlled fatigue tests, the maximum tensile and compressive strain accumulated linearly with the logarithm of the number of fatigue cycles. The results are shown in Figs. 22 - 23. It is general believed that magnetic properties of ferromagnetic material are affected by fatigue due to microstructural changes,

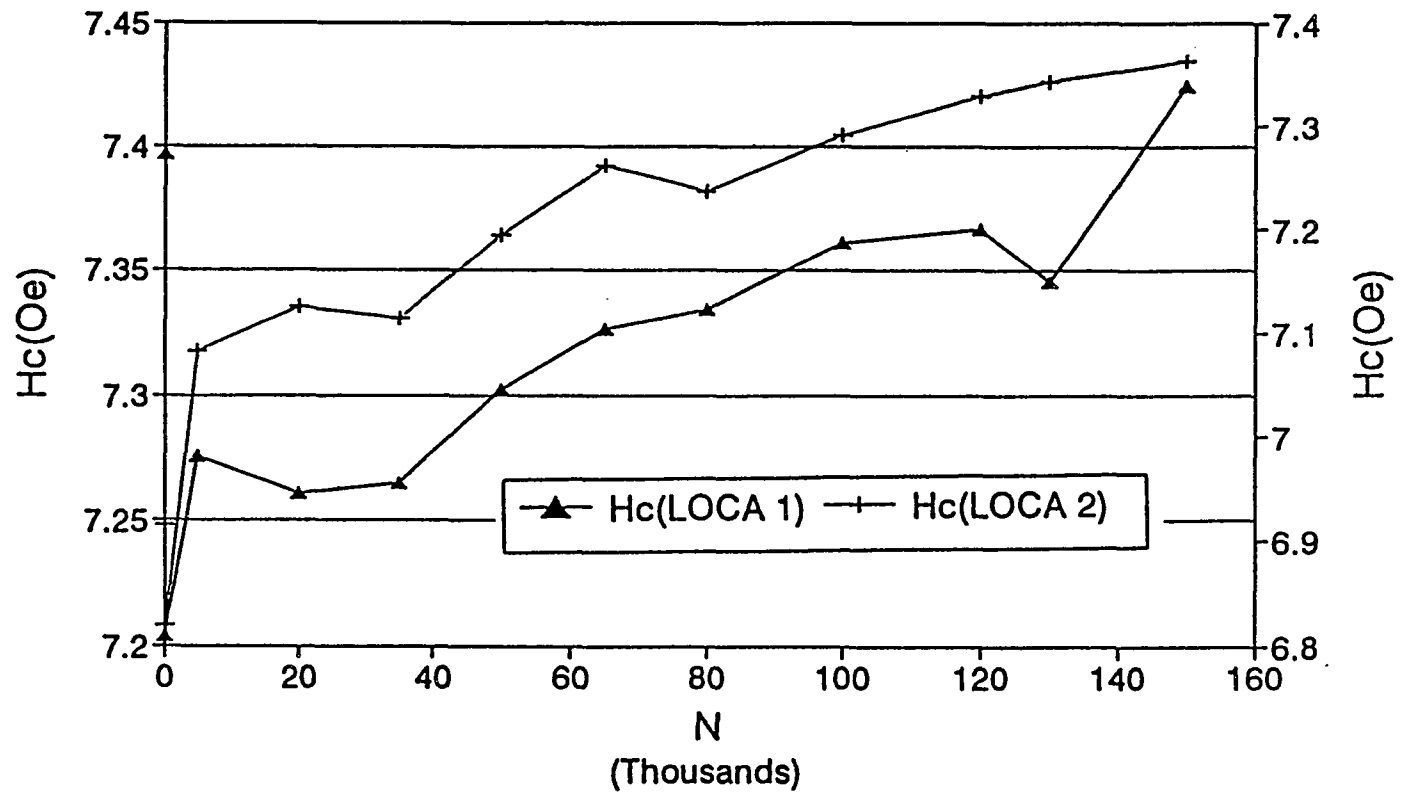


Fig. 20. Variation of coercivity at two different locations with expended life for Sample MP10 under fatigue test with stress amplitude of 272 MPa.

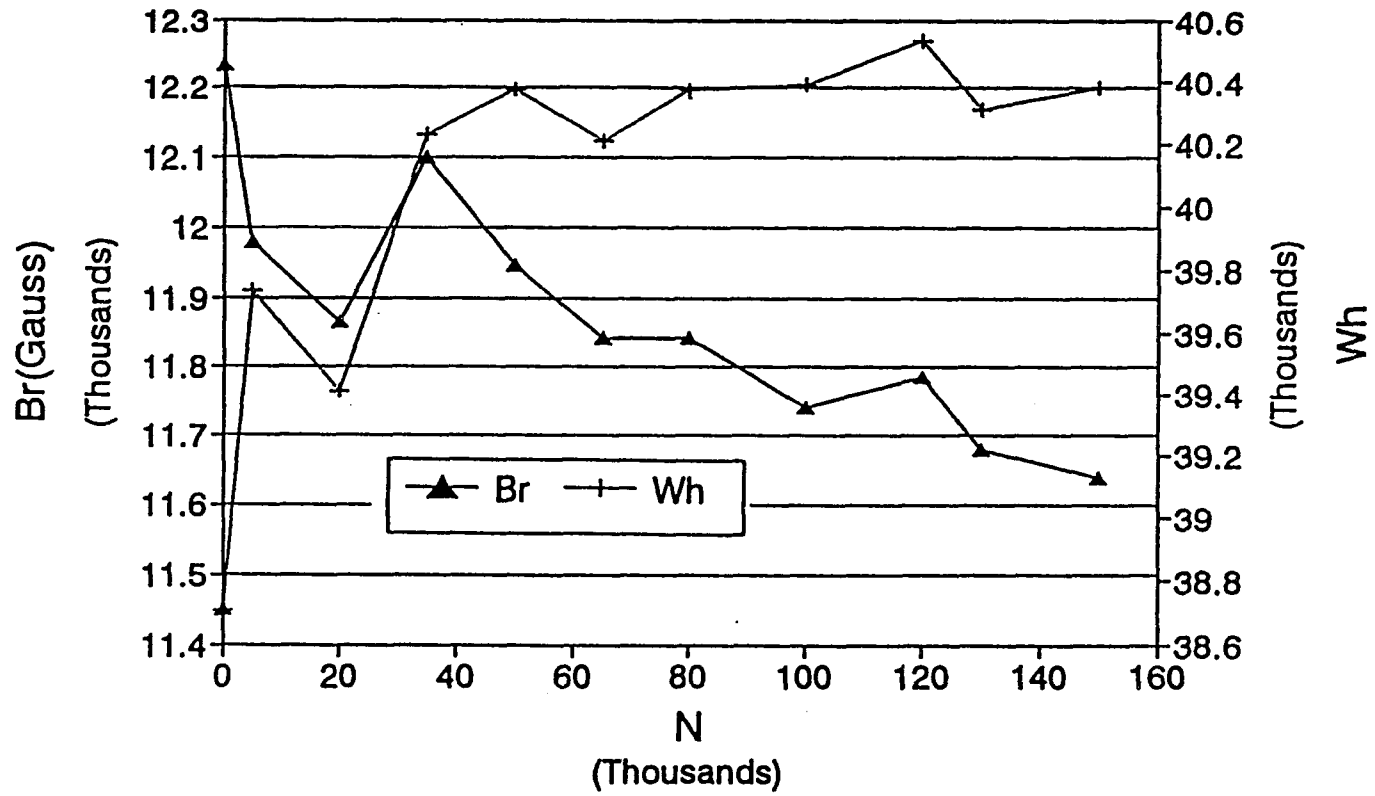


Fig. 21. Variation of remanence and hysteresis loss with expended fatigue life for Sample MP10 under fatigue test with stress amplitude of 272 MPa.

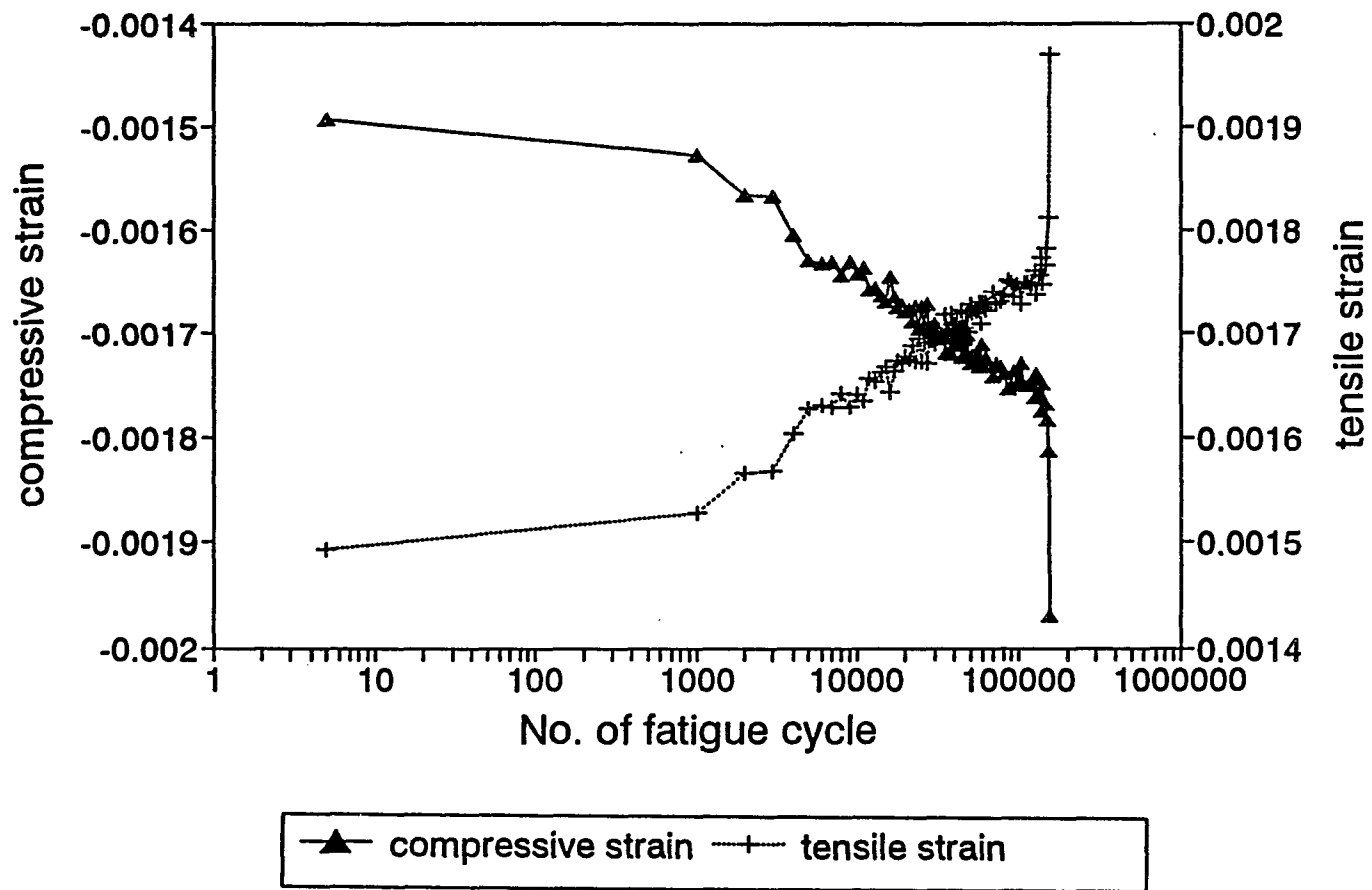


Fig. 22. Variation of compressive and tensile strain with expended fatigue life for Sample MP12 under fatigue test with stress amplitude of 272 MPa.

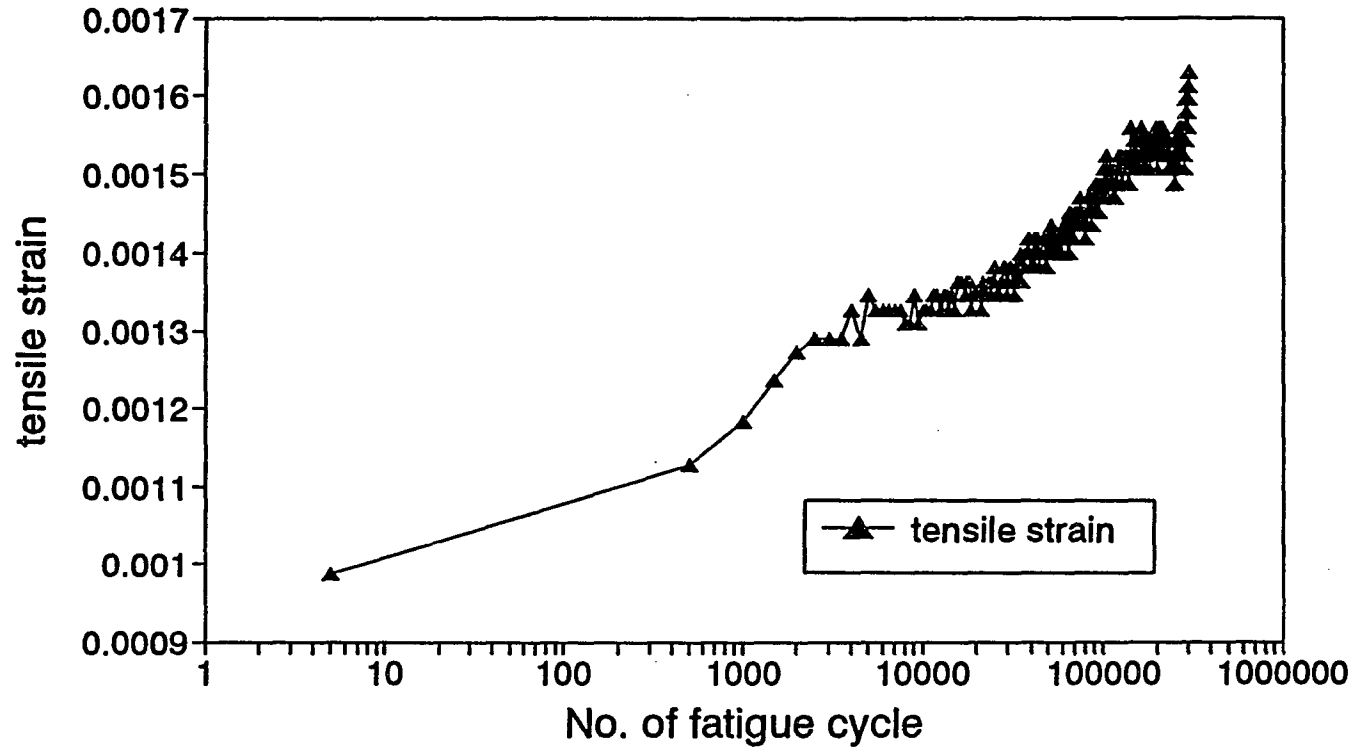


Fig. 23. Variation of tensile strain with expended fatigue life for Sample MP13 under fatigue test with stress amplitude of 243 MPa.

primary in form of dislocation activity [6, 15, 21]. Since plastic deformation generates dislocations, the observed strain data implied that dislocations were generated and dislocation density was increased during the load controlled fatigue test. This can be used to explain the increase in coercivity by domain wall dislocation interaction theory [27]. Two more specimens were fatigued under constant load amplitude, and magnetic measurements were taken at pre-determined intervals chosen according to the logarithm of the number of fatigue cycles. Results are shown in Figs. 24 - 25. It can be seen that coercivity was approximately linearly related to the logarithm of the number of fatigue cycles.

It was evident that the A533B material underwent fatigue softening when cyclically stressed. This was demonstrated for example under the strain-controlled fatigue process, when the load dropped significantly during the first few hundred cycles. However, under the load-controlled fatigue process, the coercivity increased, which implied that magnetic hardening occurred. Usually magnetic hardening is also accompanied by mechanical hardening. So the observation that the material underwent a mechanical softening accompanied by a magnetic hardening was unexpected. In fact this seemingly contradictory phenomenon can be explained by the Bauschinger effect [28]. When A533B material was fatigued, additional dislocations were generated which acted as pinning sites for domain wall motion, thus increasing the coercivity. However, during the cyclic stress, dislocations piled up at grain boundaries or precipitates, forming dislocation tangles. With reversed loading, the dislocations at the trailing edges of the tangles moved away from the grain boundary and precipitates more easily, causing an apparent softening of the mechanical properties.

Prestrain fatigue test: Since fatigue life and magnetic properties depend on the initial

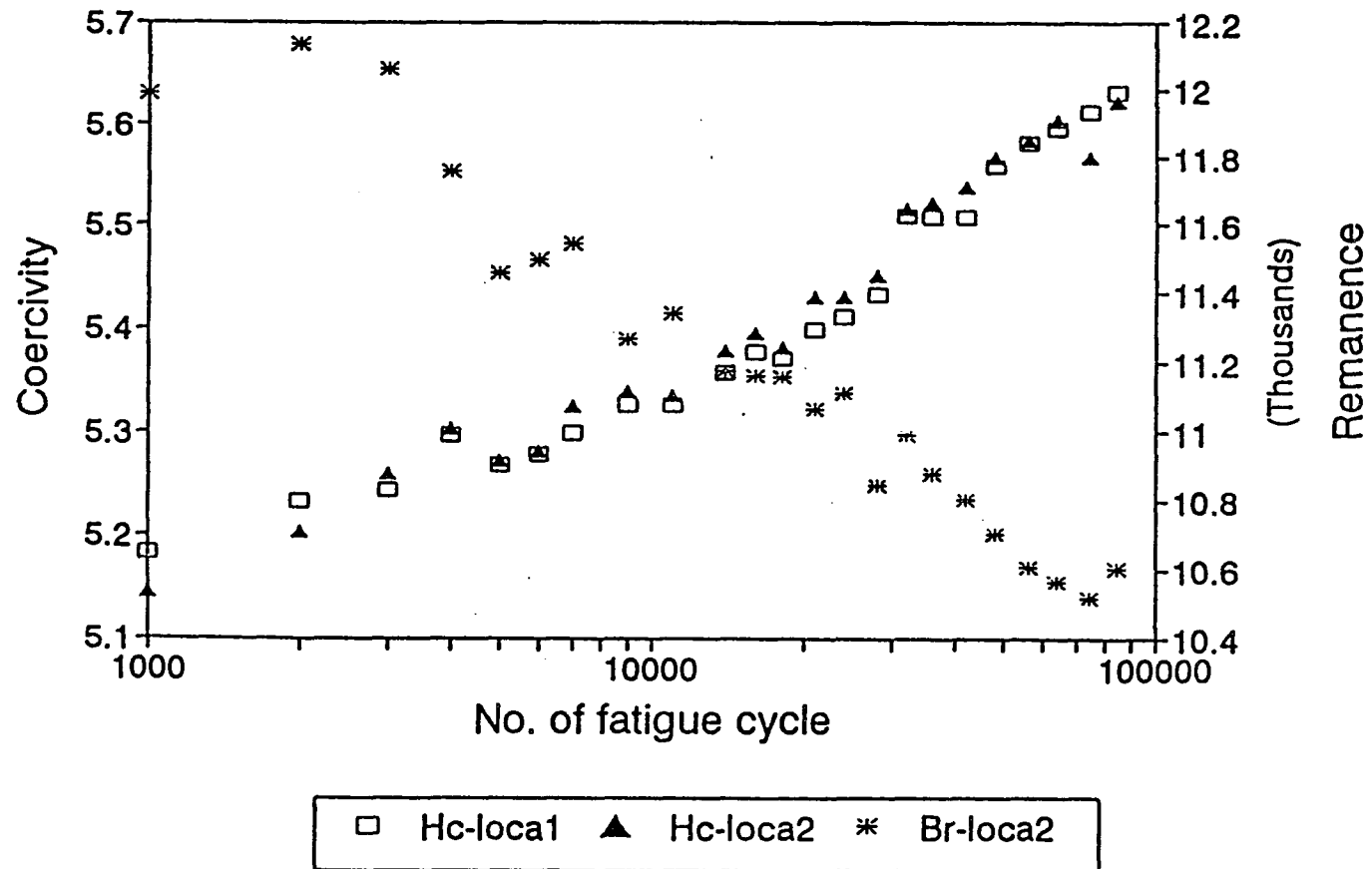


Fig. 24. Variation of coercivity and remanence with expended fatigue life for Sample MP15 under fatigue test with stress amplitude of 284 MPa.

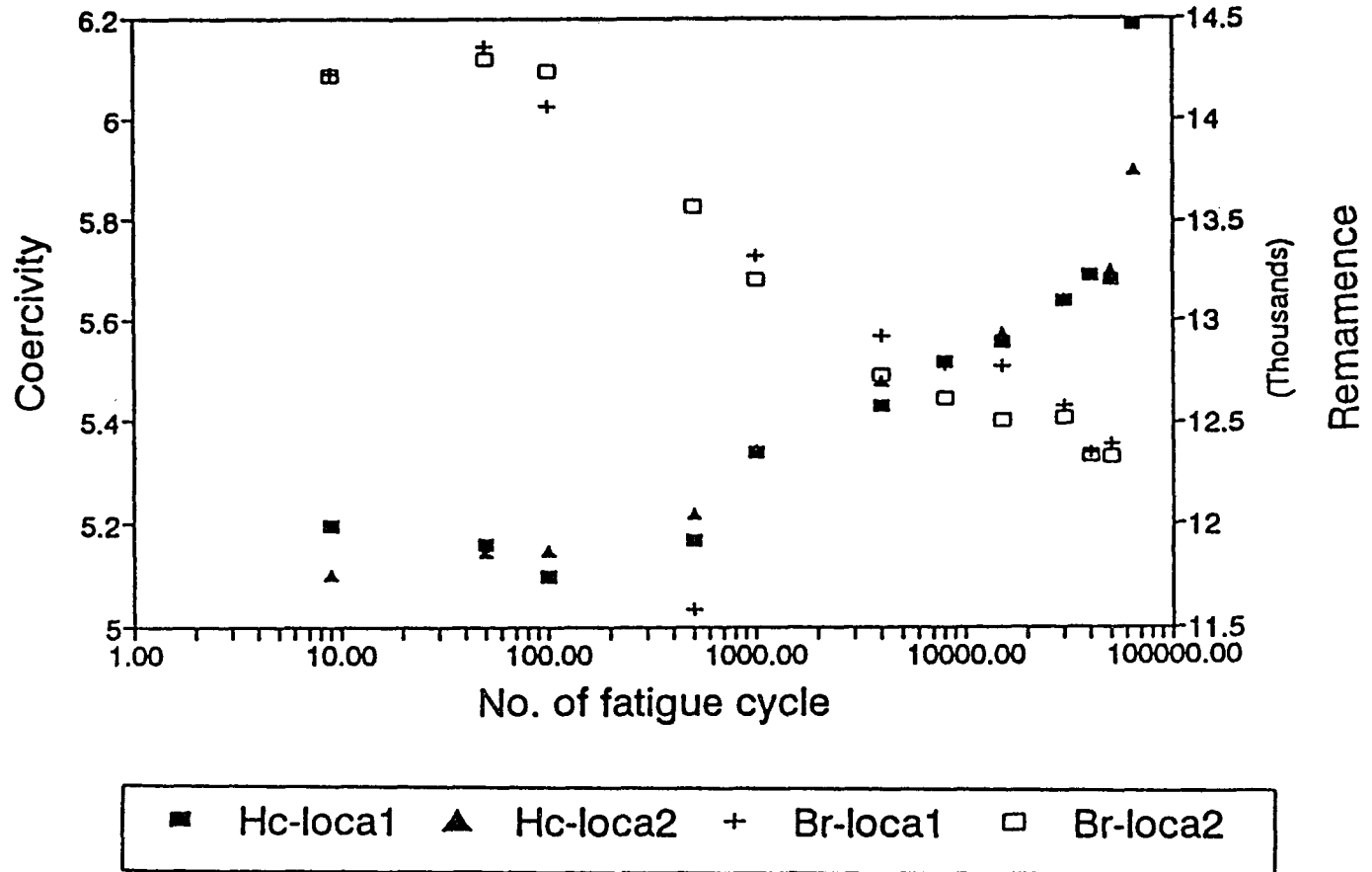


Fig. 25. Variation of coercivity and remanence with expended fatigue life for Sample MP16 under fatigue test with stress amplitude of 284 MPa.

state of the material, the role of stress history (i.e. residual stress or any previous dislocation substructure due to the plastic straining) on fatigue lifetime were examined. Five specimens were prestrained to different strain level from 0.008 to 0.021. Fatigue tests and magnetic measurements were performed under different fatigue conditions. Test results are shown in Figs. 26 - 29 . It can be seen that in strain-controlled fatigue processes, the coercivity and hysteresis loss decreased and the remanence increased. The load also showed a decrease during the fatigue life which implied fatigue softening. All these results can be explained by the fact that a large number of dislocations was created by the initial plastic deformation. When the specimens were cyclically stressed, dislocations recombined as well as piling up on the grain boundary and precipitates, resulting in a decrease in dislocation density and therefore leading to both mechanical softening and magnetic softening.

The test results again showed that the decrease in coercivity was related to the logarithm of the number of fatigue cycles. This was in agreement with the result implied from high cycle fatigue tests that is: the logarithm of the number of fatigue cycles determined the accumulation of fatigue damage in these materials.

Metallurgical Study

Scanning electron microscopy analysis: Fatigue damage is generally believed to be started with surface deformation followed by slip bands, microcracks formation and finally macro crack propagation. In order to correlate the fatigue damage with magnetic properties, metallographic studies were performed by inspecting the surface condition of specimens under SEM. Three polished samples were fatigued at constant strain amplitude of 0.003. The

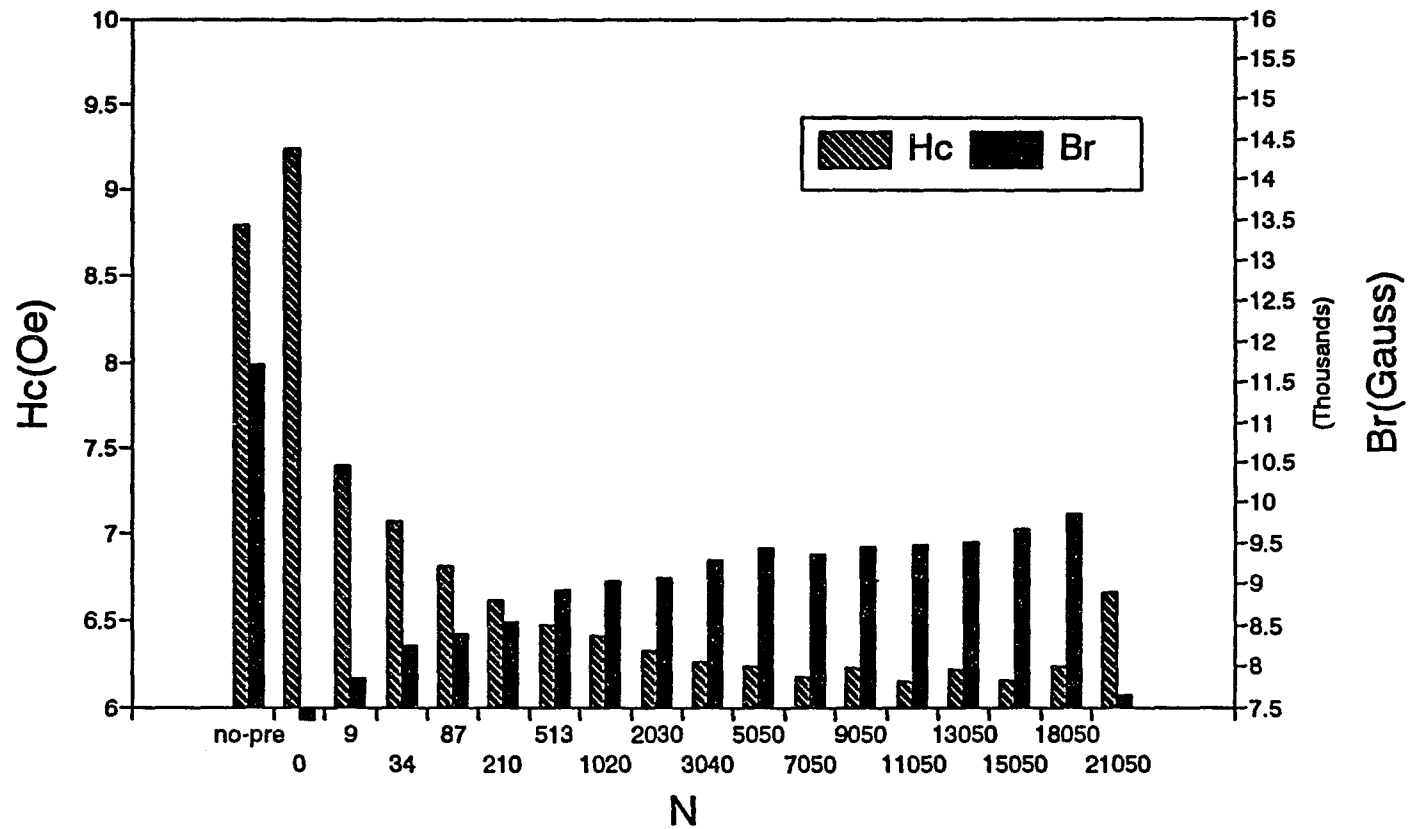


Fig. 26. Variation of coercivity and remanence with expended fatigue life for Sample PRE05 under fatigue test with strain amplitude of 0.003. The sample was prestrained with residue strain of 0.01.

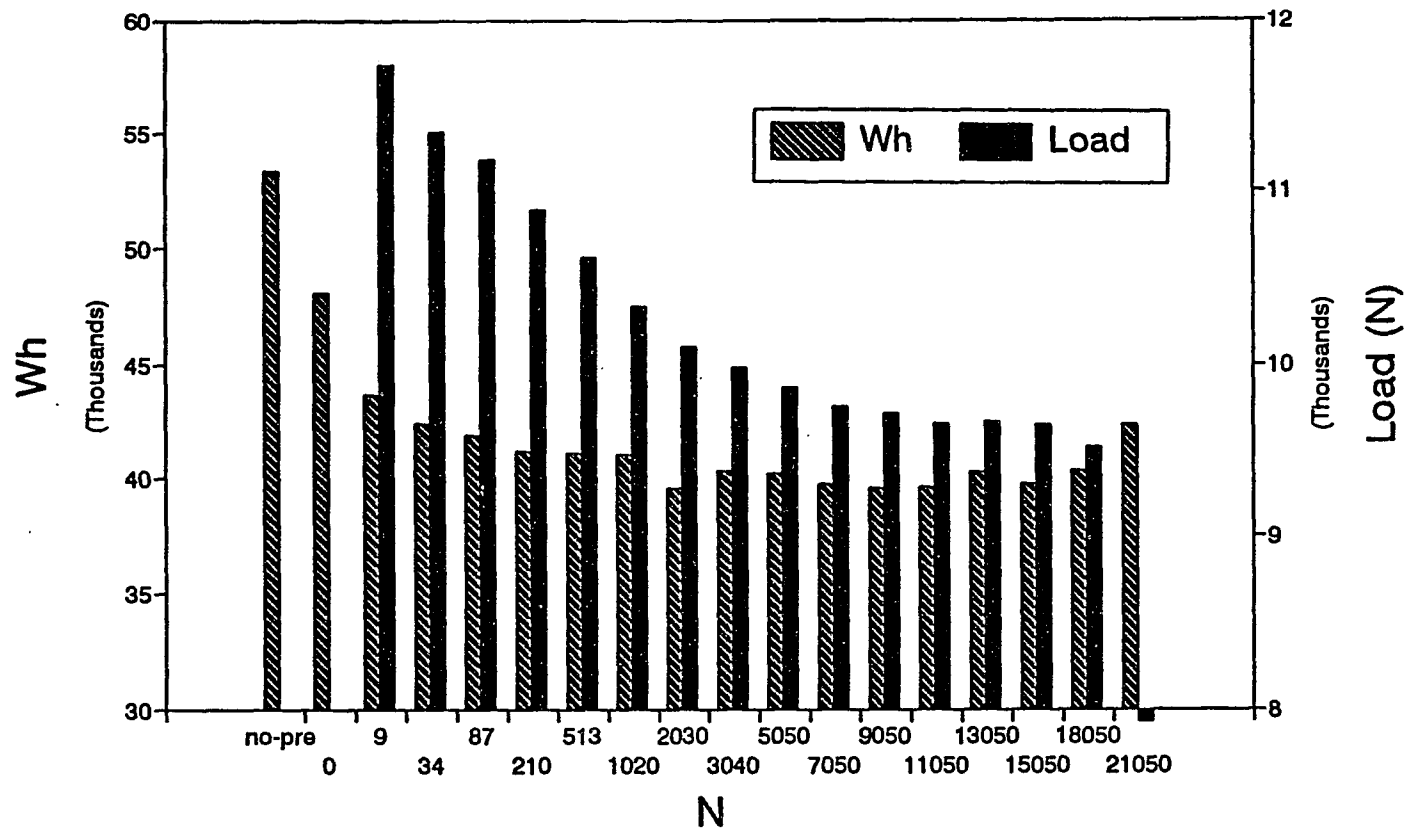


Fig. 27. Variation of hysteresis loss and tensile load with expended fatigue life for Sample PRE05 under fatigue test with strain amplitude of 0.003. The sample was prestrained with residue strain of 0.01.

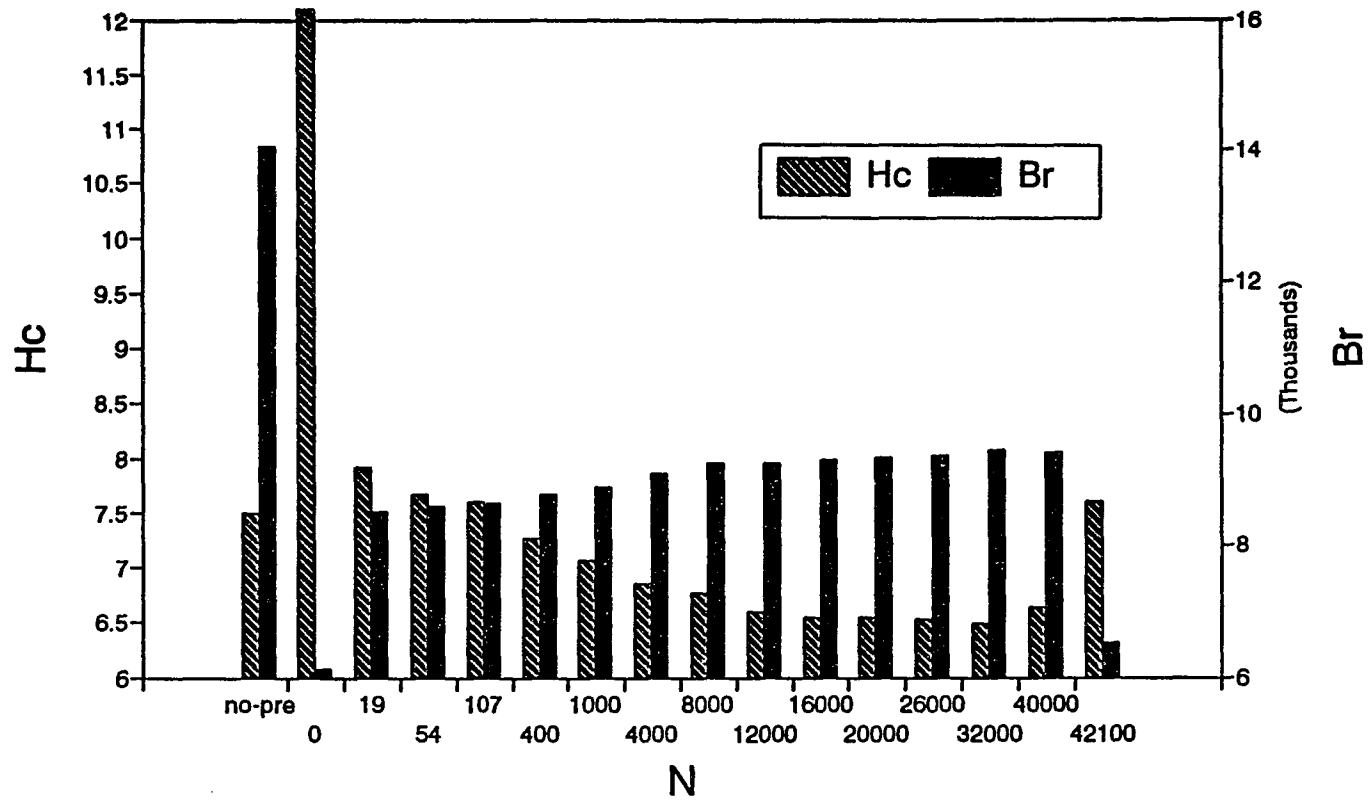


Fig. 28. Variation of coercivity and remanence with expended fatigue life for Sample PRE01 under fatigue test with strain amplitude of 0.003. The sample was prestrained with residue strain of 0.021.

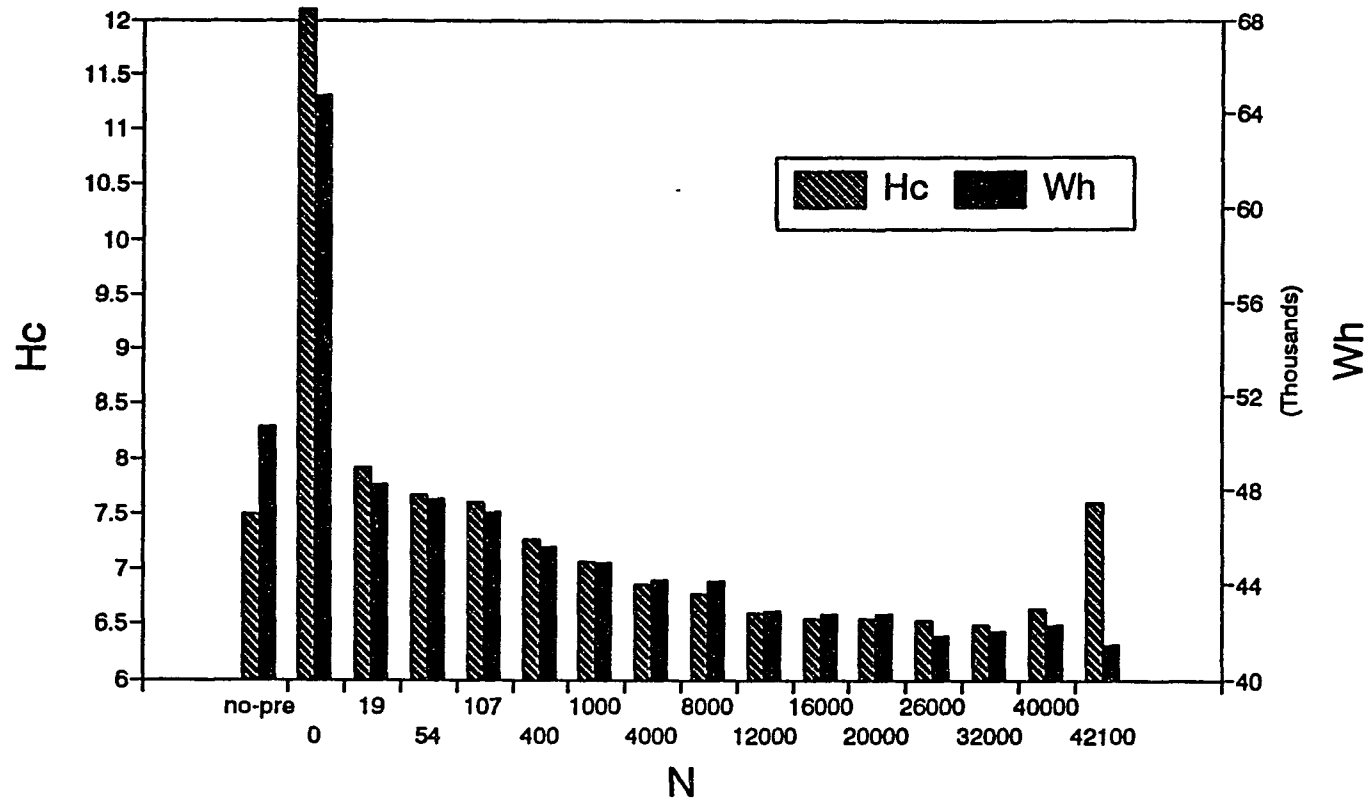


Fig. 29. Variation of coercivity and hysteresis loss with expended fatigue life for Sample PRE01 under fatigue test with strain amplitude of 0.003. The sample was prestrained with residue strain of 0.021.

surface replication technique was used to inspect the surface condition of the first two samples. The objective was to detect surface damage, such as slip band formation or surface roughening. But the results showed no such evidence in the early stages of fatigue life up to 70% of fatigue. Therefore, for the third specimen, we inspected the surface condition directly under the SEM by removing the sample from the MTS machine at predetermined cycles throughout the fatigue life.

In this latter case, SEM analysis showed that surface deformation was a relatively slow process. The formation of slip bands due to fatigue was not very obvious. In fact, it was the brittle inclusions, such as MnS, that initiated the micro cracks. These micro cracks were observed at least as early as 40% of expended fatigue life. This explained why the load began to drop even in the intermediate region of fatigue life under strain controlled fatigue tests. The formation of micro cracks at brittle inclusions resulted in a decrease in the compliance of the material. Later one of the micro cracks grew continuously to form a macro crack and led to the final mechanical failure. The progress of crack initiation and growth are shown in Figs. 30 - 33.

Optical microscopy analysis: Since inclusions played an important role in micro crack initiation, the configuration and morphology of these inclusions were of great interest. Two samples were mechanically polished and chemically etched, and examined under an optical microscope. It was found that the distribution of inclusions was inhomogeneous as shown in Figs. 34 - 37. This explains why, although most specimens had a crack initiated at the surface during fatigue, there was a case in which the load began to drop and no surface crack was observed. In that case, the crack was initiated at an inclusion inside the

Fig. 30. Microcrack initiated inside the brittle inclusion at about 40% fatigue life.

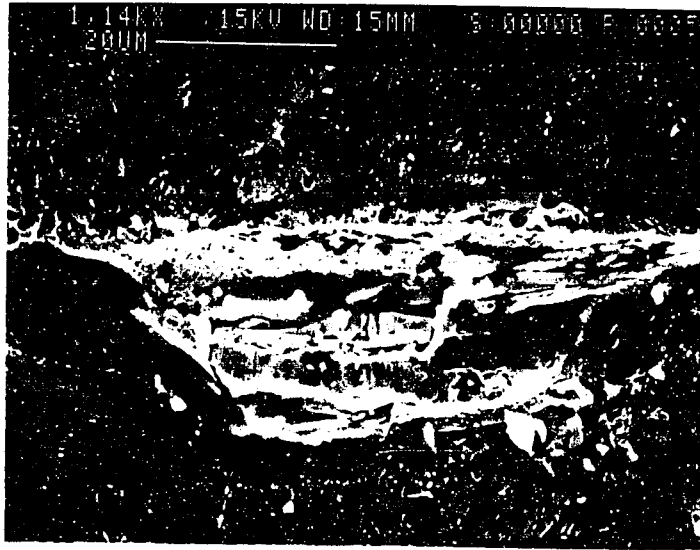


Fig. 31. Microcrack initiated at the brittle inclusion at about 40% fatigue life.

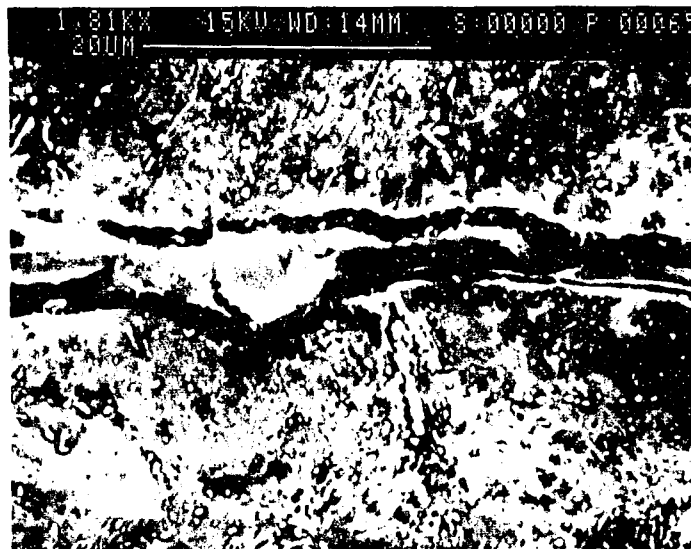
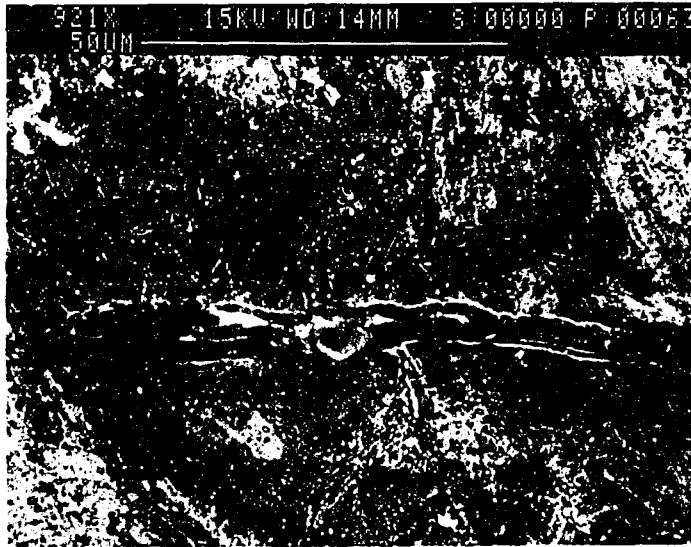


Fig. 32. Growth of microcrack due to fatigue (at about 60% of fatigue life).

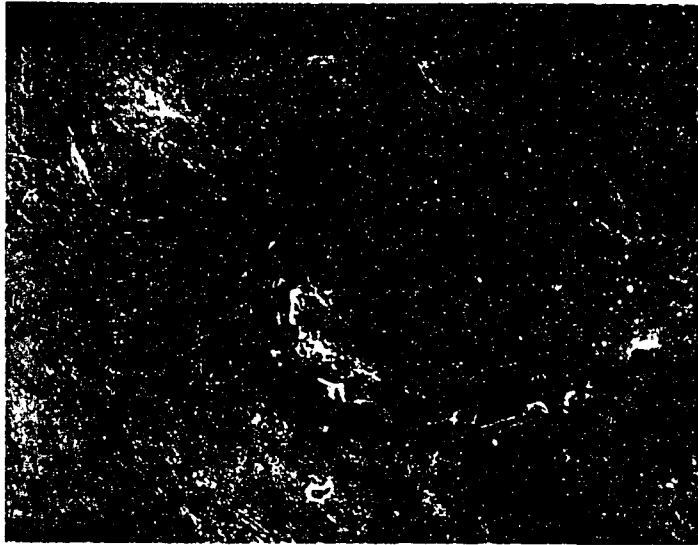


Fig. 33. Growth of microcrack due to fatigue (at about 70% of fatigue life).



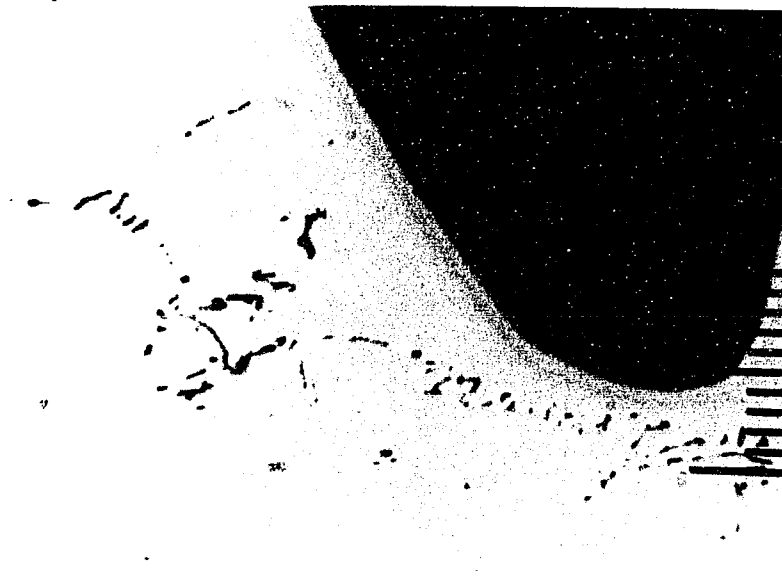


Fig. 34. Distribution of inclusion inside A533B steel (with magnification of 65).

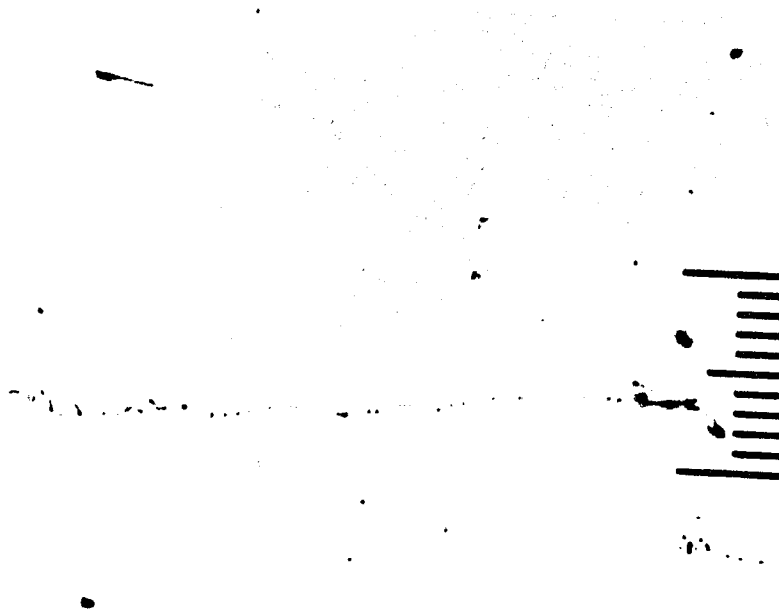


Fig. 35. Line distribution of inclusion inside A533B steel (with magnification of 65).

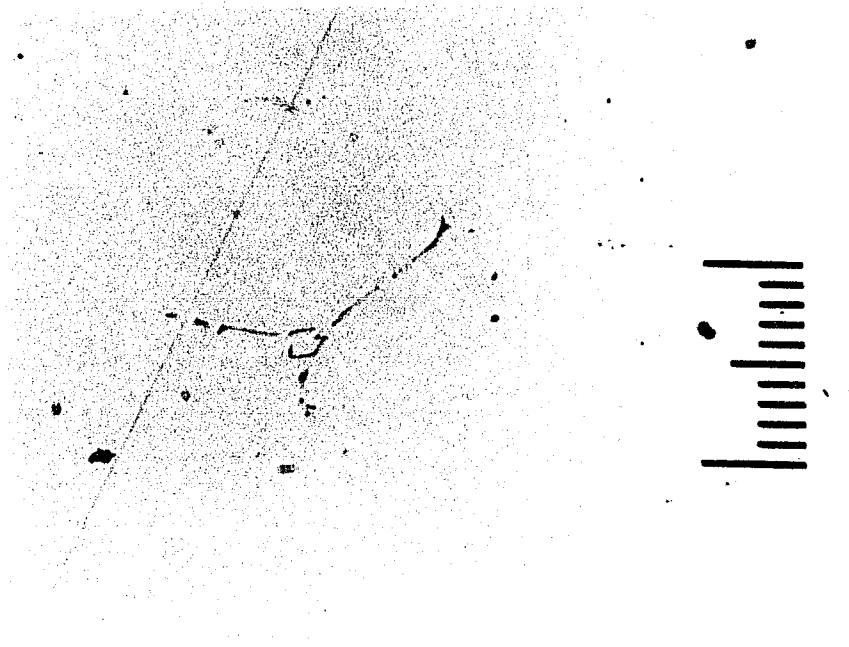


Fig. 36. Distribution of inclusion on grain boundary inside A533B steel (with magnification of 65).



Fig. 37. Shape of inclusion (with magnification of 520).

sample and then grew towards the surface.

Dependence of Coercivity on the Number of Fatigue Cycles

Although much research has been conducted previously to study the effect of fatigue on magnetic properties, a direct relation between a magnetic parameter (such as coercivity or remanence) and the level of fatigue was lacking, even for well controlled fatigue conditions. Under cyclic stress at constant load amplitude, it was found that the maximum tensile and compressive strain increased continuously throughout the whole fatigue life, after the initial few hundred stress cycles which caused fatigue softening. A linear relationship between the magnitude of the strain amplitude and number of stress cycles was observed on a semi-log graph, as shown in Figs. 22 - 23. This result indicated that the plastic strain accumulated logarithmically with the number of stress cycles.

Correlations between mechanical properties and magnetic properties have been studied previously [29, 30]. It was found for example that the coercivity H_c was generally linearly related to the plastic strain of a material, and this relationship can be understood theoretically because increased plastic strain results in a linear increase in dislocation density, which increases the pinning term k in the theory of hysteresis [31]. If this relation also holds in the fatigue process, then according to the experimental discovery of the logarithmic relationship between plastic strain and number of stress cycles, the same logarithmic relation between coercivity and number of stress cycles should be expected.

From Figs. 22 - 23, the strain amplitude and the number of stress cycles N can be related by following equation:

$$\varepsilon - \varepsilon_0 = a \ln(N) \quad (20)$$

where ε_0 is the intercept along the strain axis and a is the slope of the line. Assuming the linear relationship between the coercivity and the plastic strain, the following equation is obtained:

$$H_c - H_{c0} = b \ln(N) \quad (21)$$

Where H_{c0} and b are constants under the specific test condition. This relation fits experimental observation shown in Figs. 20 - 21 very well. Eq. 21 can also be expressed as:

$$N = c_1 \exp(c_2 H_c) \quad (22)$$

where C_1 and C_2 are determined by H_{c0} and b . The parameters C_1 and C_2 in Eq.22 can be experimentally determined by three measurements of (N_0, H_{c1}) , $(N_0 + \Delta N, H_{c2})$, $(N_0 + \Delta N', H_{c3})$, where ΔN , and $\Delta N'$ are two intervals of number of fatigue cycles between successive measurement. Although Eq. 22 does not indicate the final value of fatigue life, it does show how to estimate accumulated fatigue damage by measuring coercivity. If the total fatigue life can be predetermined by an alternative method, then this model can be used to monitor fatigue damage. It is believed that for the first time a magnetic parameter has been shown to be directly related to the number of fatigue cycles. This demonstrates that the quantitative assessment fatigue damage by a magnetic NDE method is possible.

CONCLUSIONS

The effects of fatigue on the magnetic properties of A533B steel have been investigated. Results of this investigation indicate that magnetic properties were very sensitive to fatigue induced microstructure changes and therefore demonstrated that the magnetic hysteresis method is viable NDE technique for detecting the fatigue damage in ferromagnetic structural materials. Results show that the changes in the magnetic properties, especially the variation in coercivity and remanence, can be used as a measure of fatigue damage. In strain controlled low cycle fatigue, impending failure can be predicted from the rapid changes in the magnetic properties. In high cycle fatigue with constant load amplitude, the accumulated fatigue damage can be estimated by measurements of coercivity base on experimental relation between the coercivity and the number of fatigue cycles. This relation enables one to estimate fatigue exposure of a material by a magnetic measurement, and to gain an insight into the relationship between the magnetic properties and fatigue damage.

REFERENCES

- [1] Mirko Klesnil and Petr Lukas, Fatigue of Metallic Materials (Elsevier Science Publishing Company, New York, 1992).
- [2] M.S.C. Bose, NDT International, 19(2), 83 (1986).
- [3] K. Titto, Nondestr Test Eval. 5, 27 (1989).
- [4] T.W. Wlodek, Canad. Mining metallurgy, (Bull) 47, 5 (1944)
- [5] P.E. Cavanach, Pro. ASTM 47, 639 (1947).
- [6] F. Vicena, Czech. J. Phys. 9, 187 (1957).
- [7] R. Salkin, Materialprufung, 6, 201 (1964).
- [8] G. Iliescu, Rev. Roum. Sci. Tech., Ser. Met. 11(2), 207 (1966).
- [9] H.D. Schumann, Phys. Stat. Sol (a) 18 K27 (1973).
- [10] H. Mughrabi, R. Kutterer, K. Lubitz and H. Kronmuller, Phys. Stat. Sol (a) 38, 261 (1976)
- [11] M.B. Shah and M.S.C. Bose, Phys. Stat. Sol (a), 86, 275 (1984).
- [12] M.S.C. Bose, NDT International, 19(2), 83 (1986).
- [13] C.H.A. Sanford-Francis, Bri J NDT, 23, 241 (1981).
- [14] C.H.A. Sanford-Francis, Bri J NDT, 29, 83 (1987).
- [15] V.A. Demkin, Scripta metall. Mater. 27, 319 (1992).
- [16] L.P. Karjalainen and M. Moilanen, NDT International, 12(2), 51 (1979).
- [17] L.P. Karjalainen, M. Moilanen and R.Rautioaho, Mater. Eval. 37(9), 45 (1979).
- [18] J.C. McClure, Jr., S. Bhattacharya and K. Schroder, IEEE Trans. Mag. MAG-10, 913 (1974).

- [19] G.A. Matzkanin and C.G. Gardner, "Measurement of residual stress using magnetic Barkhausen noise analysis," In Proc. ARPA/AFMI Review of Quantitative NDE, Tech. Rep. AFML-TR_75-212, CA, 971 (1976).
- [20] L. Pentti Karjalainen and Markku Moilanen, IEEE Trans. Mag. MAG-16, 514 (1980).
- [21] M.K. Devine, D.C. Jiles and S.Hariharan, J. Magn. Magn. Mat., 104, 377 (1992).
- [22] M.R. Govindaraju, A. Strom, D.C. Jiles, S.B. Biner and Z.J. Chen, J. Appl. Phys, 73(10), 6165 (1993).
- [23] Z.J. Chen, A.Strom and D.C. Jiles, IEEE Tran. Mag. MAG-29, 3031, 1993.
- [24] M.R. Govindaraju, Z.J. Chen, A. Strom, S.B. Biner and D.C. Jiles, "SEM and TEM investigation of fatigue induced microstructural changes and resulting effect on magnetic properties of structural steels", Proceedings of the 1993 ASM Material Week, Pittsburgh, Pennsylvania, 18-21 October, 1993.
- [25] D.C. Jiles, S.Hariharan and M.K. Devine, IEEE Tran. Mag. MAG-26, 2577 (1990).
- [26] A.R. Eichmann, M.K. Devine and D.C. Jiles, IEEE Tran. Mag., MAG-28, 2462, (1992).
- [27] H.R. Hilzinger and H. Kronmuller, J. Magn. Magn. Mater. 2, 11(1976).
- [28] G.E. Dieter, Mechanical Metallurgy (McGraw-Hill, New York, 1986).
- [29] D.C. Jiles, Phys. Stat. Sol.(a), 108, 147 (1988).
- [30] D.C. Jiles and D. Utrata, Review of Progress in Quantitative Nondestructive Evaluation (Edited by D.O. Thommpson and D.E. Chimenti, Plenum Press, New York, 1988), 7, p. 1255.
- [31] D.C. Jiles, J. Magn. Magn. Mater. 61, 48 (1986).

PART III.

**MAGNETIC HYSTERESIS MEASUREMENTS IN THE DETECTION
OF CREEP DAMAGE**

INTRODUCTION

Creep damage is the slow plastic flow of metal under stress and at high temperature. These temperatures are typically about 50% of the absolute melting temperature. The result is a very slow viscous flow of the metal which ends in sudden failure. This problem has been recognized in alloy steels that have been used in steam generators, turbines, and pipelines in power plants operating at high temperatures, typically in the range 500 - 600°C, and under stress for an extended period of time. Creep failure occurs by a process of cumulative damage which involves plastic deformation, nucleation and growth of cavities at the grain boundaries, subsequent linkage of these cavities to form microcracks and finally the propagation of these microcracks until failure.

A typical creep curve, showing the variation of strain with time, for elevated temperature creep is shown in Fig. 38. The applied load produces an initial strain. The material then deforms with time at first with rapid rate (primary creep), but this rate of strain gradually decreases until it becomes independent of time (secondary or steady state creep). Eventually, the strain rate again increases with time (tertiary creep) and deformation continues at an accelerating rate until the material fails. While the creep process may be formulated in terms of detailed mechanisms [1] or continuum damage parameters [2], the predictive ability of available models is not yet of sufficient accuracy, even for simple loading conditions. Therefore prediction of material lifetime based on available creep damage models is not reliable. Actually creep damage is affected by various transient conditions, arising from cyclic, thermal and mechanical loadings, constraints and the crack growth itself.

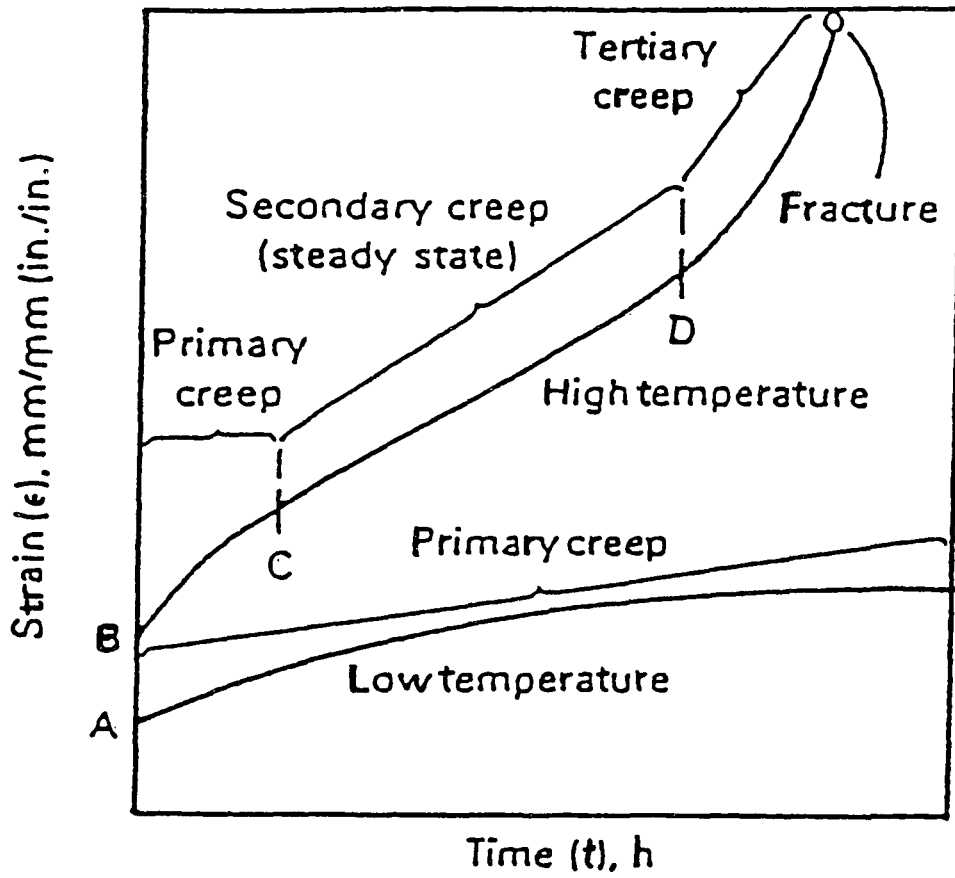


Fig. 38. Dependence of creep-induced strain on time.

This is especially true in complex structures in which the local histories of stress, temperature and microstructure vary over time and throughout the material. As a result, physical testing a component for creep damage is usually required for each local area of interest.

At present, the most widely used method to evaluate creep damage is the replication technique [3-4]. This technique employs a high resolution device such as a scanning electron microscope (SEM) to indirectly look at the material microstructure by inspecting a replica of a highly polished portion of the component surface. The replica is made using an epoxy film. This is sputtered with gold and then examined under a SEM. This technique is sensitive to all stages of the microstructural changes, but it requires a plant shutdown and substantial amount of time and effort to perform the replica examination.

During the creep process, the microstructures of materials, such as defect (impurity and dislocation) density in the matrix and cavitation and microcracks at grain boundaries, undergo continuous change before catastrophic failure. Being sensitive to microstructure [5], effects of stress [6-7] and thermal history [8] of ferromagnetic material, magnetic property measurements have recently been investigated as an NDE method to detect creep damage. Devine et al. [9] used magnetic hysteresis measurement to inspect the heat affected zone (HAZ) and the weld metal of serviced-aged Cr-Mo steel pipeline, and found that the coercivity and remanence of creep damaged samples were smaller than those in undamaged specimens. They also found that the orientation of the inspection head with respect to the weld line affected the sensitivity of magnetic inspection. Govindaraju et al. [10] performed an on-site investigation into the variation of the magnetic properties of creep damaged Cr-Mo

steel welds at thermal power plants operated by Ontario Hydro. They found that although there was a considerable scatter in the measured parameters due to many unknown material and process variables, a general decreasing trend in coercivity, remanence and their product were observed resulting from creep damage. Recently Mitra et al.[11] studied creep effect by magnetic Barkhausen emission measurement. They found that Barkhausen parameters such as RMS voltage and number of Barkhausen events per hysteresis cycle were sensitive to creep damage. In addition, a direct correlation between Barkhausen parameters and magnetic hysteresis parameters was found, in which a low coercivity was always accompanied by a high Barkhausen voltage in creep damaged materials.

Although previous results were encouraging, the systematic study of creep damage by magnetic NDE methods is only at an early stage. This work is concerned with a recent study of determining creep damage on Cr-Mo base steel from hysteresis measurements. It is found that structure sensitive parameters such as coercivity, remanence and hysteresis loss decrease with creep damage. This could be due to the total effects of (1) reduction of domain wall pinning by moving impurity and dislocations to the grain boundaries and (2) creation of local demagnetization fields due to cavity formation. A numerical calculation based on these effects using a modified Jiles-Atherton model [12] was performed to corroborate the experimental results. The microstructure of the creep damaged sample has also been studied by scanning electron microscope (SEM) and energy-dispersive spectrometry (EDS) to determine the metallurgical changes occurring during creep damage of the material.

EXPERIMENTAL

Materials and Specimens

Two sets of specimens were used in this investigation. They were both Cr-Mo pipe steels. The first set consisted of three pieces of P22 Cr-Mo steel from Arizona Public Service Company, labelled as B, C, D respectively as shown in Fig. 39. They were cut from three steam pipes with different degrees of stress histories but the same thermal history. The degrees of creep damage characterized by their remaining service life were estimated by destructive metallurgical evaluation [13] and the result is shown in Table 7. The chemical compositions of these specimens were very close as can be seen in Table 8.

The second set specimens were cut from a steam header, supplied by the General Atomics, with an inside diameter of 9.5" and outside diameter of 17". The materials were service-aged 2.25 Cr - 1.0 Mo pipe steel. The test samples were prepared by cutting seven flat specimens with thickness of 3/10" from different layers of the pipe steel, so that the inner surfaces of the sections represented respectively planes at 1.3", 1.7", 2.1", 2.5", 2.9", 3.3" and 3.7" from the outside surface of the pipe. Samples are labelled as layers 0, 1, 2, 3, 4, 5, 6 respectively, and their locations are shown in Fig. 40. The chemical compositions of these specimens were expected to be the same, as they were all cut from the same pipe.

Inspection Head

A specially designed inspection head was made in this study for the in situ measurement of magnetic properties. A diagram of the inspection head is shown in Fig. 41.

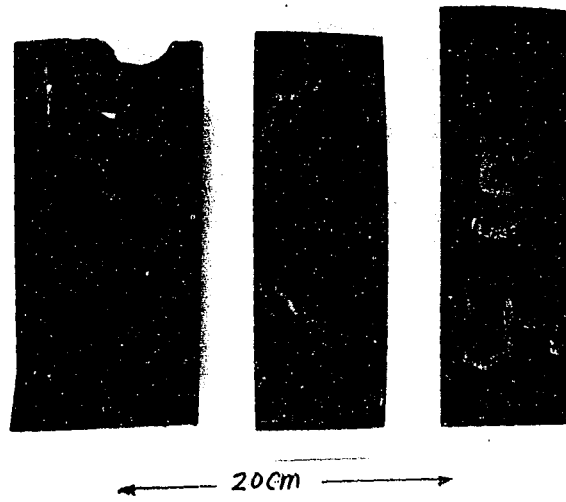
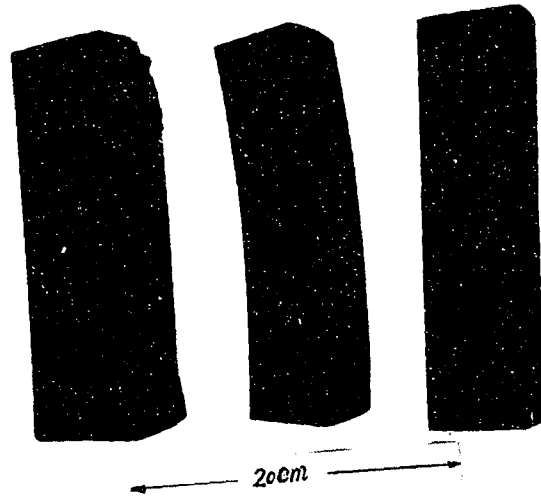


Fig. 39. Creep samples cut from steam pipes.

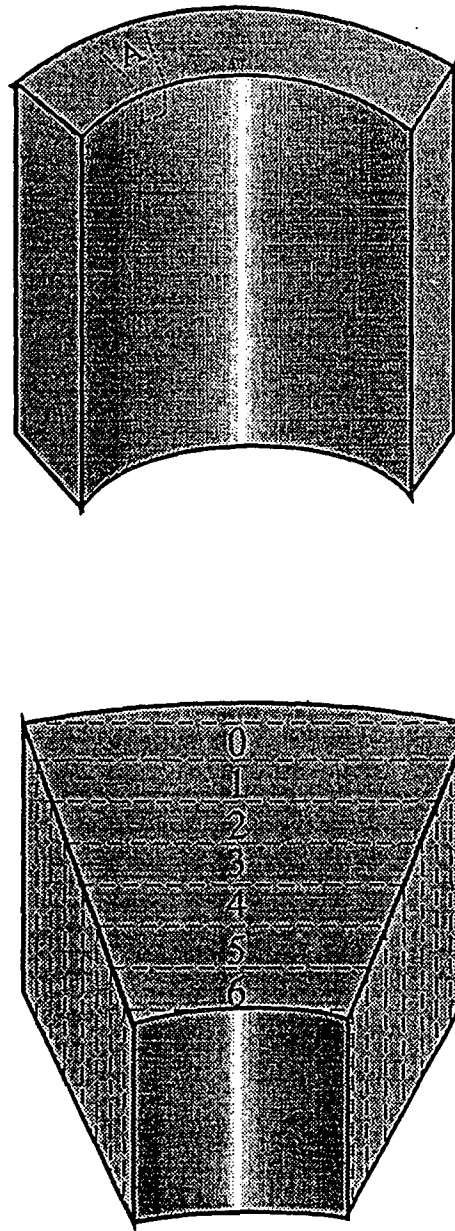


Fig. 40. Location of creep specimens taken from steam header.

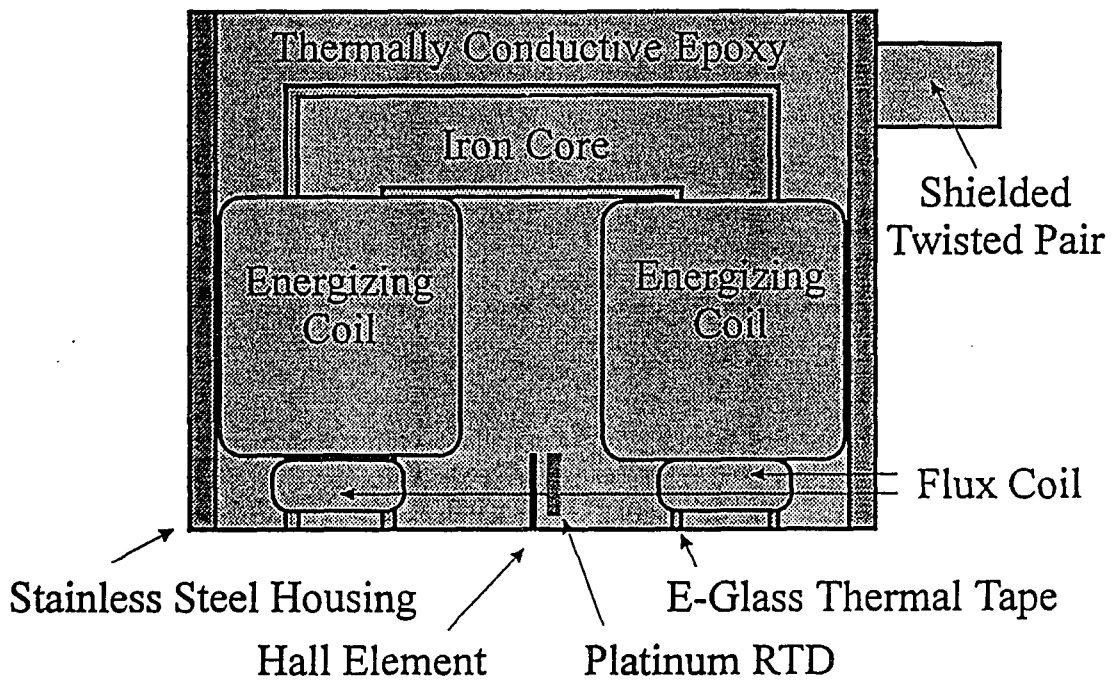


Fig. 41. Configuration of inspection head.

Table 7. Degree of creep damage of specimens of Set I

Pipe Sample	Estimated Remaining Life (year)
B	2.2
C	1.5
D	10.0

Table 8. Chemical composition of creep specimens of Set I

Element	Sample B	Sample C	Sample D
C	0.11	0.12	0.11
Mn	0.42	0.41	0.41
P	0.010	0.008	0.009
S	0.018	0.019	0.019
Si	0.22	0.22	0.21
Cr	2.11	2.08	2.11
Mo	0.94	0.93	0.94
Al	0.03	0.02	0.01
Sn	0.01	0.01	0.01
Cu	0.13	0.12	0.12
Ni	0.15	0.15	0.15
Cb	0.01	0.01	0.01

It consisted of a C-shaped core embedded in epoxy inside a stainless steel case. The epoxy served to fix the relative position of the C-shaped core and Hall probe with respect to the outer steel-case, which was a cylinder which was elliptical in cross-section with a major axis of 1.5" and a minor axis of 1.25". The case was 0.125" thick. The C-shaped core, made of soft Armco iron with cross section of 1/4" x 1/4", was centered along the long axis of the steel case. The Hall probe was fixed in the middle of the space between the poles of the C-core. A primary coil was wrapped around the core across the top. The sensing coil was split so that one half was on the bottom of each pole piece. The integration of the inspection head inside the steel case had certain advantages in a magnetic measurement. Specifically this (1) made the inspection head easy to hold, (2) reduced unsteadiness in holding the inspection head to the sample, (3) eliminated the tilting of the inspection head with respect to the test sample, and (4) provided a fixed lift-off distance Δl for all the measurements. The inspection head used here was made with zero inherent lift-off distance ($\Delta l=0$).

Magnetic Measurements

Magnetic hysteresis parameters, such as coercivity, remanence and hysteresis loss were measured by the Magnescope [14], which is a computer controlled magnetic inspection system together with an inspection head which can detect the magnetic field on the surface of a specimen and the magnetic flux through the core of the inspection head with minimal preparation.

Measurements on specimens belonging to Set I were performed on two radial surfaces and the outer surface of each specimen. Due to the curvature and roughness of the

specimens, a magnetic coupling gel was used to improve the conduction of magnetic flux and to minimize the effective air gap due to lift off. A statistical analysis was performed to show the standard deviation of measurement results. Measurements on specimens belonging to Set II were performed on the inside surface of each sample.

Metallurgical Study

Metallurgical studies, which consisted of SEM analysis, EDS study and optical microscopy analysis, were only performed on the specimens of Set II. Specimens belonging to Set I were restricted only for nondestructive testing by the supplier. Since creep damage is believed to be associated with grain boundary cavitation, in order to correlate the creep damage with magnetic properties, direct observation of grain boundaries under SEM and EDS was made. In doing this, a small piece of steel was cut from each sample belonging to Set II. Each piece was then cooled in liquid nitrogen and then fractured. The function of the low temperature was to make the material brittle so that intergranular fracture occurred as a result. This is important for the study of grain boundary cavitation. The fracture surface was then examined under the SEM (model Cambridge S-200). In order to distinguish fracture induced cavity from creep induced cavity, polished specimens were also examined under SEM without mechanical fracture. In optical microscopy studies, micrographs were taken on each sample under a Zeiss 47 56 60-9902 optical microscope after mechanical polishing and chemical etching.

RESULTS

Magnetic Hysteresis Measurements

The magnetic hysteresis technique, under dc conditions, measures bulk properties. For specimens belonging to Set I, test results taken on the sides and the outer surface of specimens showed consistent magnetic properties. A general decrease in coercivity, remanence and hysteresis loss was found from samples D to B to C, following the sequence of increasing creep damage. This implies that as creep progressed, the Cr-Mo steel underwent a magnetic softening process. Typical test results on coercivity, remanence and hysteresis loss are shown in Figs. 42 - 43. Fig. 43 also shows the statistical analysis of the magnetic measurements. It can be seen that the variation of magnetic properties due to the creep is significant compared to the variation in measurements due to the different surface conditions of these specimens. This confirms the early measurement results on the effects of creep damage by Govindaraju et al.[10]

For specimens of Set II, magnetic measurements were performed with the inspection head oriented at 5 different angles (0° , 22.5° , 45° , 67.5° and 90°) with respect to the long axis of the pipe. In each case, six hysteresis loops were taken at different locations of each sample. Except for one case, all the experimental results were quite similar, showing a general decrease in coercivity H_c and hysteresis loss W_h from the outside layer to the inside layer while remanence B_r and maximum flux density B_{max} showed little evidence of change. Typical test results of magnetic properties at different layers are shown in Fig. 44 for cases of 90° orientation. Fig. 44(a) shows an approximately 12% reduction in coercivity from

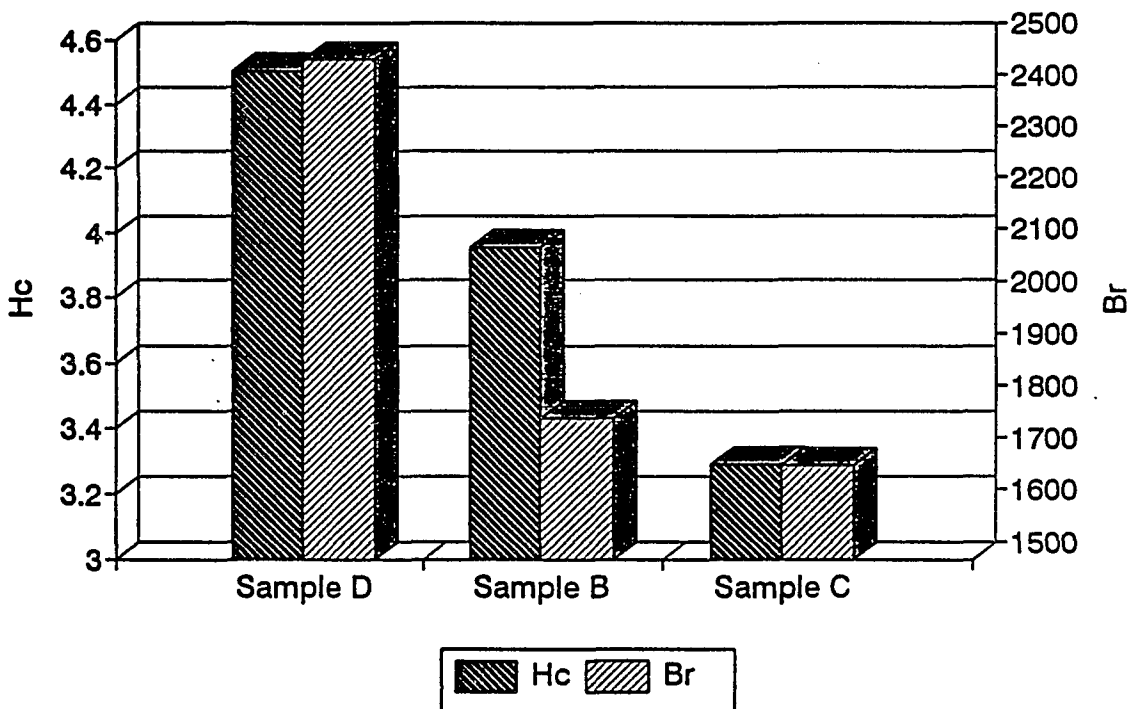


Fig. 42. Coercivity and remanence measured on radial sections of specimens in Set I.

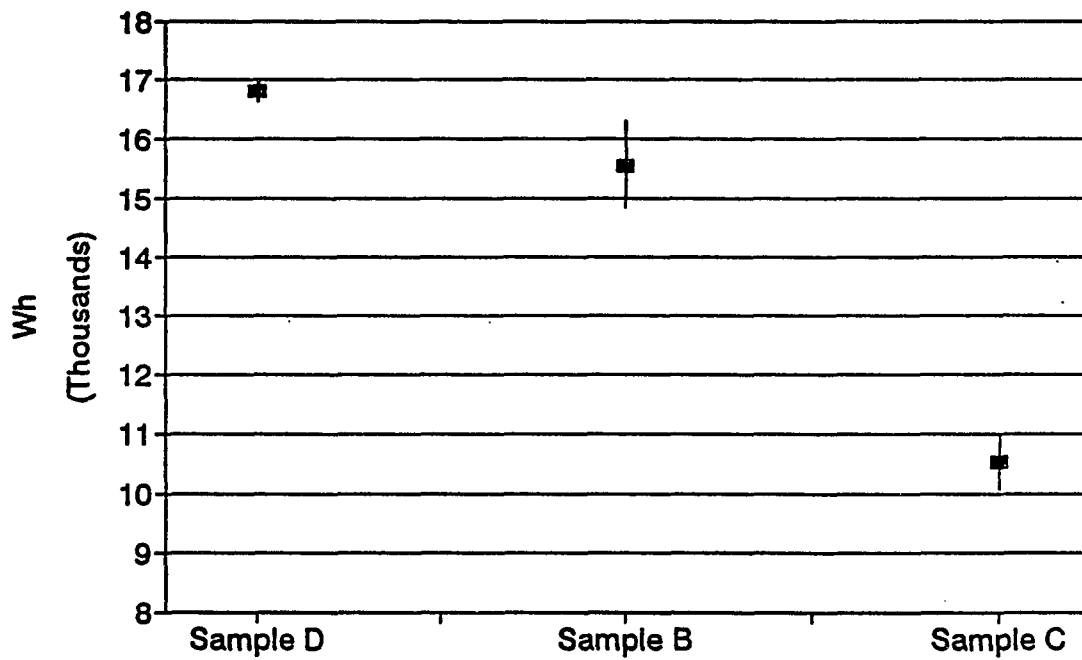


Fig. 43. Hysteresis loss measurement at the outer surface of specimen of Set I. Error bar stands for \pm one standard deviation.

outside to inside while in Fig. 44(b) W_n shows about a 6% reduction. In Fig. 44(c) and 44(d), B_r and B_{max} remain essentially constant.

Metallurgical Study

In searching for creep-induced microstructure changes, metallurgical studies of Set II specimen were performed. Typical optical micrographs for polished samples are shown in Fig. 45. It can be seen that there was little difference in microstructure in terms of grain size between the different layers of the pipe. Also, no significant grain boundary cavitation was observed in these samples.

However under SEM with high power resolution, creep induced cavitation was observed. On fractured surface, while most of the surface area was quite smooth, representing intra-granular fracture, a few rough surface areas were found which indicated inter-granular fracture. The inter-granular fracture was caused by the reduction in fracture energy due to the formation of grain boundary cavitation. A close inspection of the rough area at higher magnification did reveal some cavity-like defects. Typically SEM micrographs for Sample 3 were shown in Fig. 46. To verify that location A was a real cavity, EDS studies were performed at A, B, C. Results are shown in Fig. 47. and compared Table 9.

One might doubt that the observed cavities on fracture surface could be caused by mechanical fracture due to sample preparation rather than creep damage. In order to exclude this possibility, directly examination of mechanically polished samples under SEM was performed. Special attention was focused on grain boundaries. As a result, grain boundary cavities were also observed. Results on Sample 1 are shown in Fig. 48.

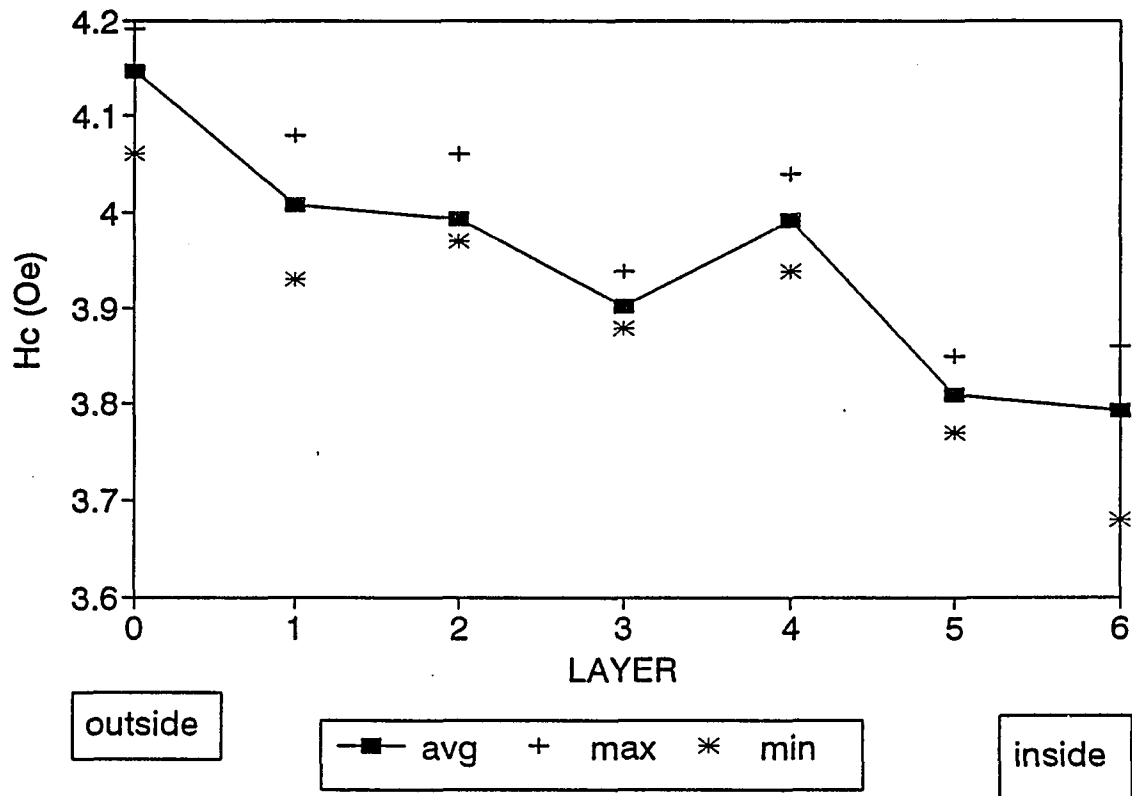


Fig. 44. Magnetic properties at different layers, (a) coercivity.

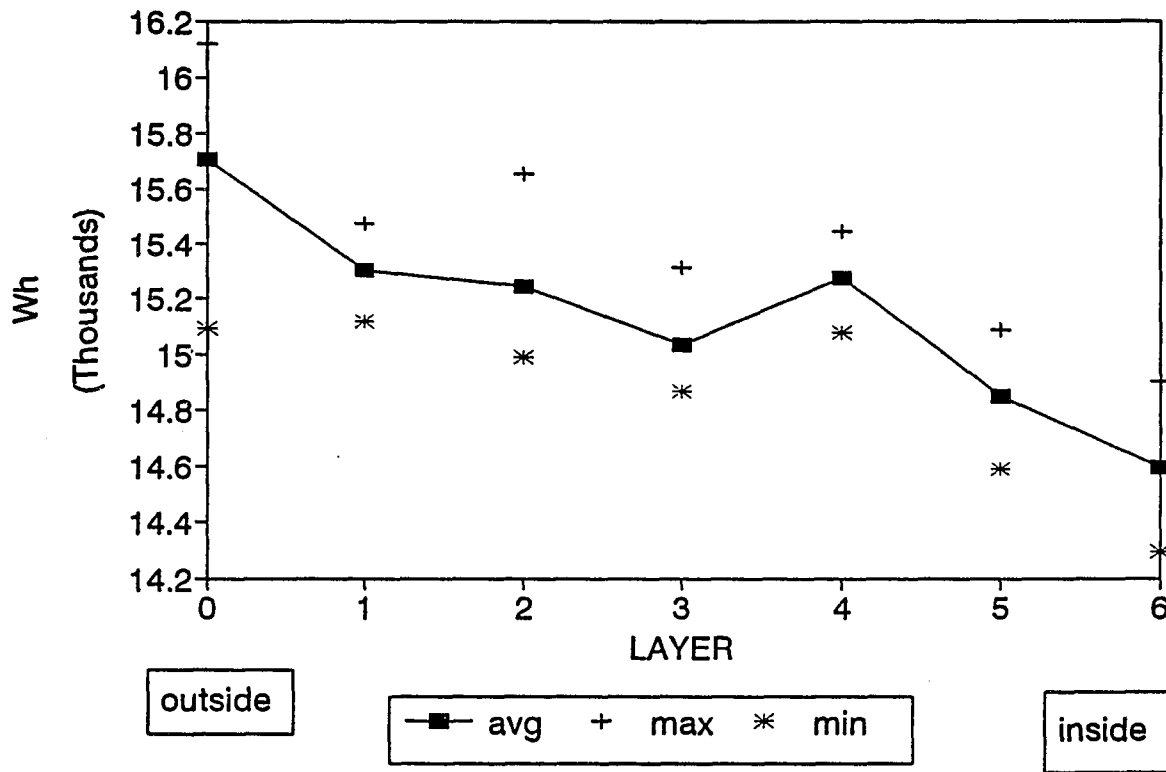


Fig. 44. (Continued) (b) Hysteresis loss.

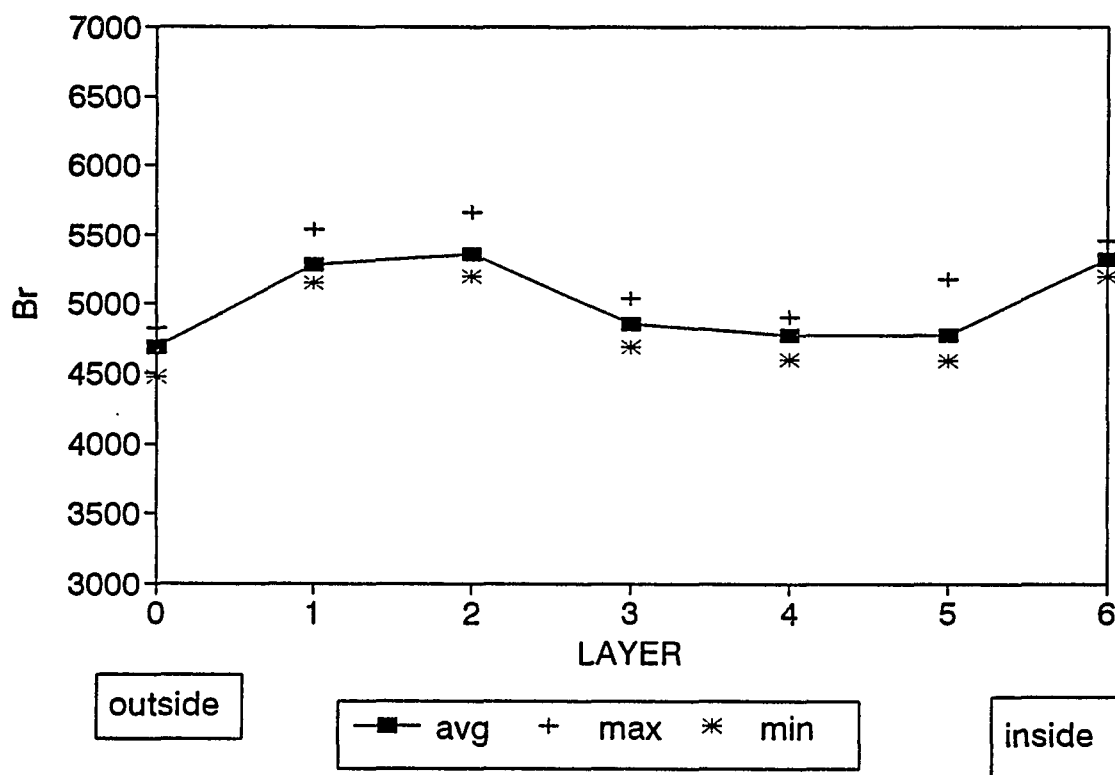


Fig. 44. (Continued) (c) Remanence.

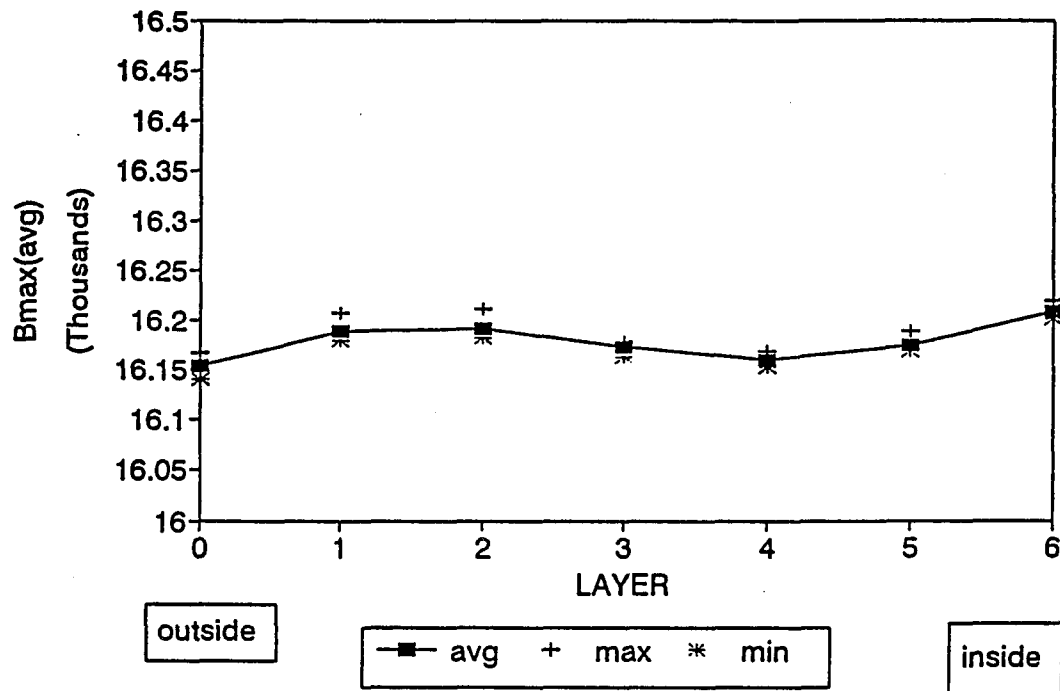
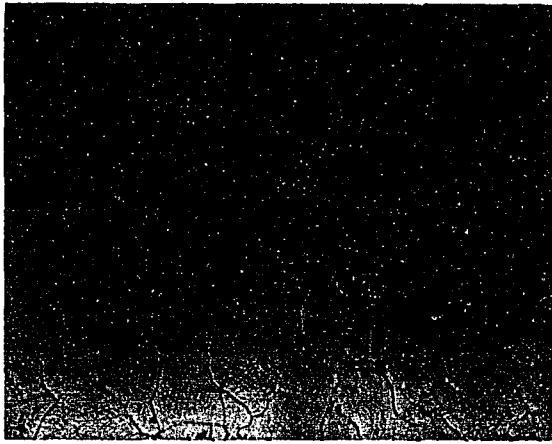
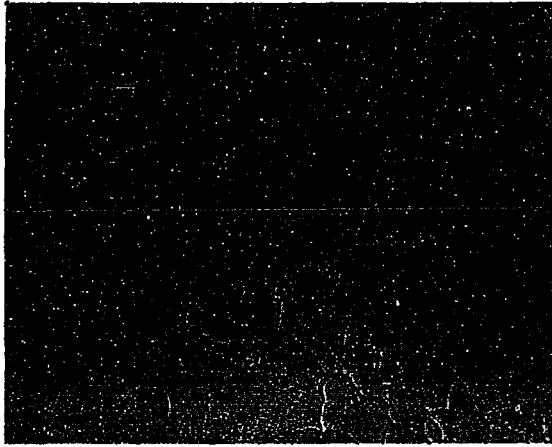
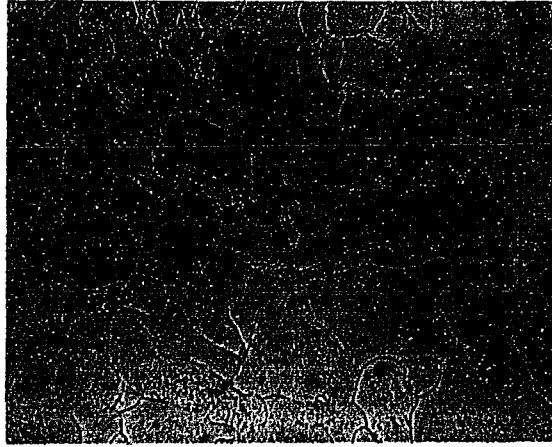
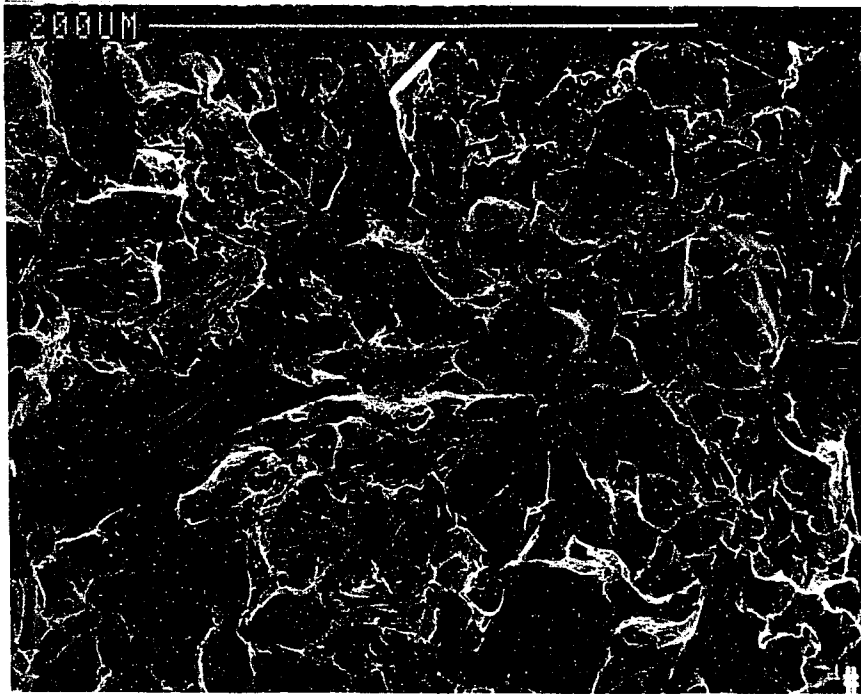


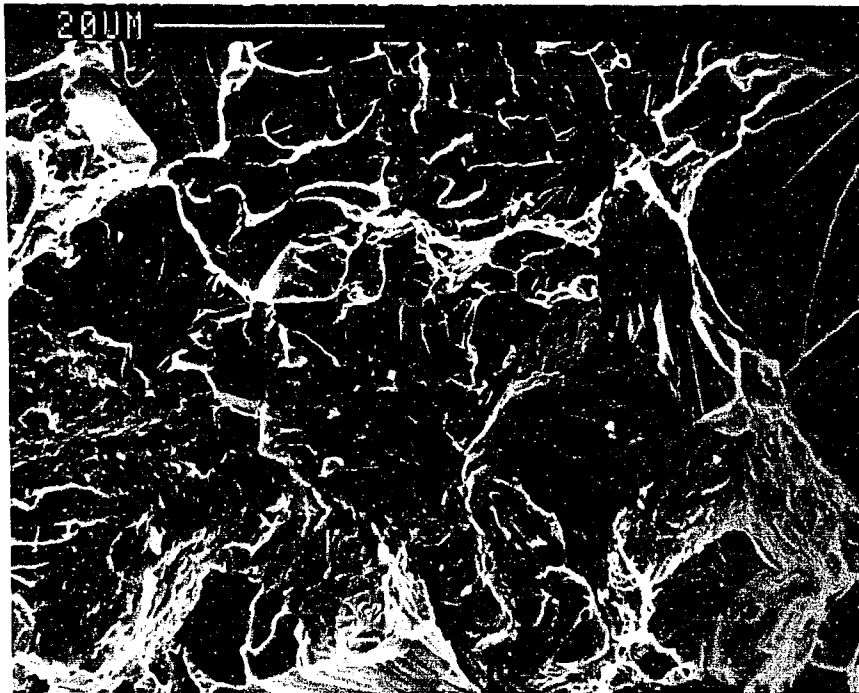
Fig. 44. (Continued) (d) Maximum magnetic induction.

Fig. 45. Optical micrograph of pipe steel (a) at inside layer, (b) at middle layer and (c) at outside layer.



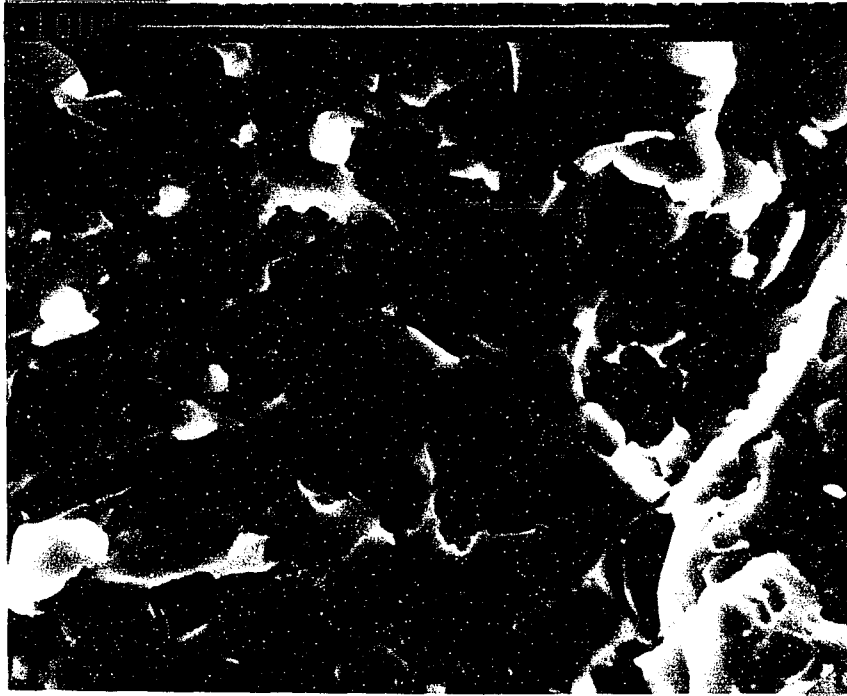


(a)

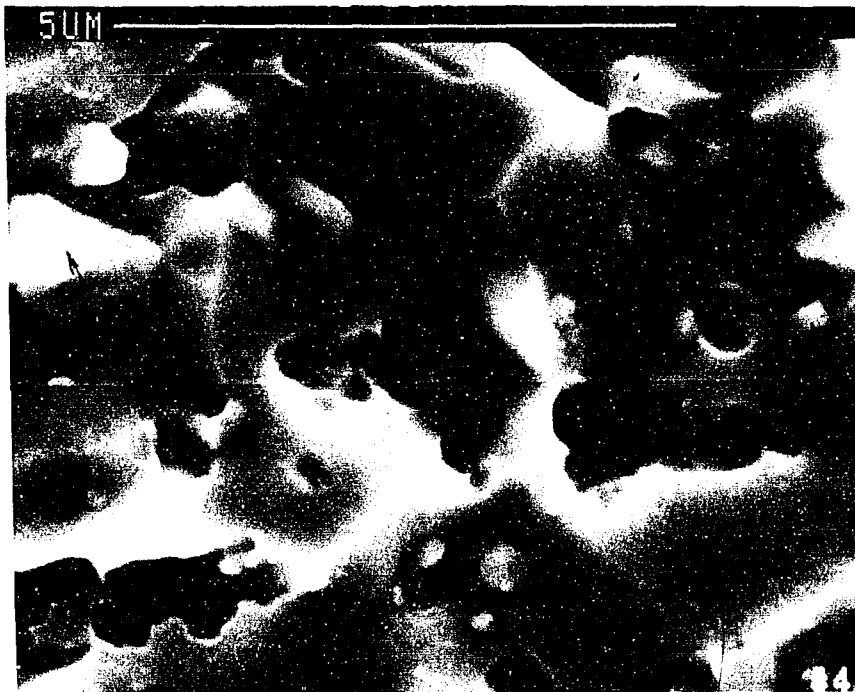


(b)

Fig. 46. Fracture surface of Sample 3 (a) with magnification of 251, (b) with magnification of 1050.

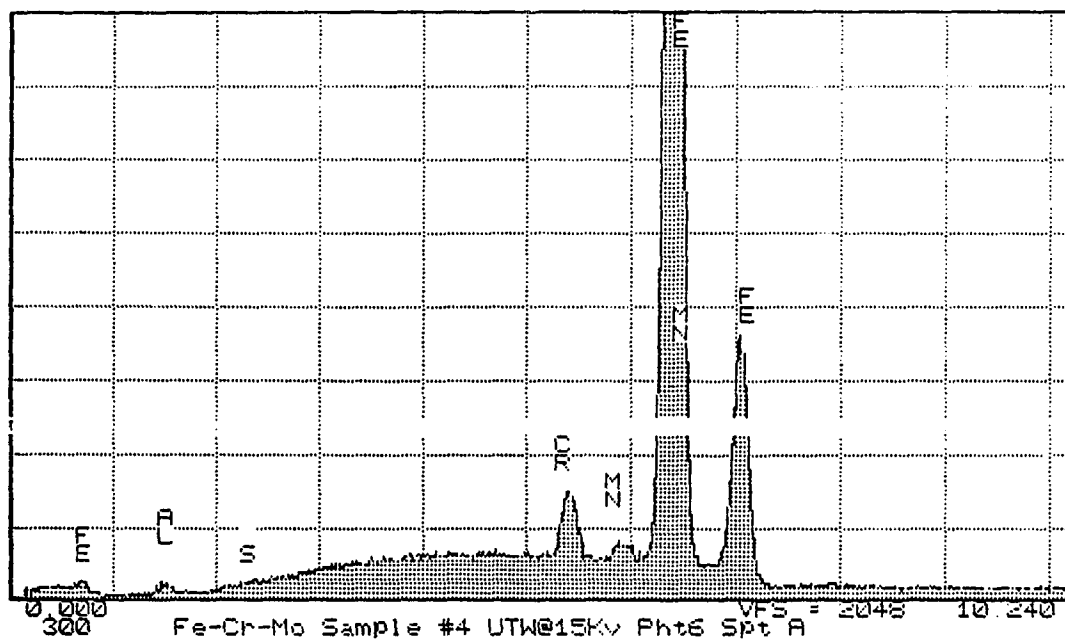


(c)



(d)

Fig. 46. (Continued) (c) with magnification of 4990, (d) with magnification of 10200.



SEMI-QUANTITATIVE ANALYSIS: Fe-Cr-Mo Sample #4 UTW@15Kv Pht6 Spt A
EL NORM. K-RATIO

FE-K 0.96014 +- 0.00322
CR-K 0.03488 +- 0.00050
MO-L 0.00002 +- 0.00001
SI-K 0.00000 +- 0.00000
O -K 0.00069 +- 0.00004
C -K 0.00425 +- 0.00019

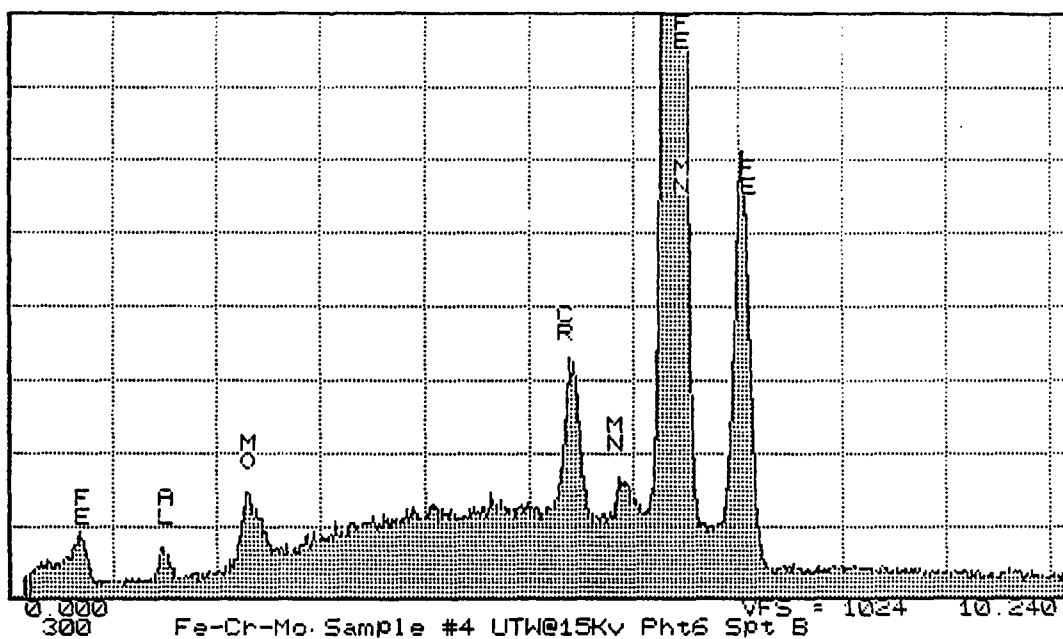
ZAF CORRECTION 14.95 KV 35.00 Degs

No. of Iterations 1

----	K	[Z]	[A]	[F]	[ZAF]	ATOM.%	WT.%
FE-K	0.960	1.000	1.002	1.000	1.003	96.63	97.13
CR-K	0.034	0.999	1.006	0.779	0.783	2.95	2.76
MO-L	0.000	1.090	1.151	0.996	1.252	0.00	0.00
SI-K	0.000	0.890	1.736	0.999	1.546	0.00	0.00 G *
O -K	0.000	0.856	1.643	0.999	1.407	0.34	0.10 *
C -K	0.004	0.839	0.044	0.999	0.037	0.07	0.02

* - High Absorbance

Fig. 47. EDS analysis at (a) spot A.



SEMI-QUANTITATIVE ANALYSIS: Fe-Cr-Mo Sample #4 UTW@15Kv Pht6 Spt B
 EL: NORM. K-RATIO

FE-K 0.94018 +- 0.00350
 CR-K 0.04392 +- 0.00062
 MO-L 0.00846 +- 0.00023
 SI-K-0.00000 +- 0.00000
 O -K 0.00076 +- 0.00004
 C -K 0.00665 +- 0.00026

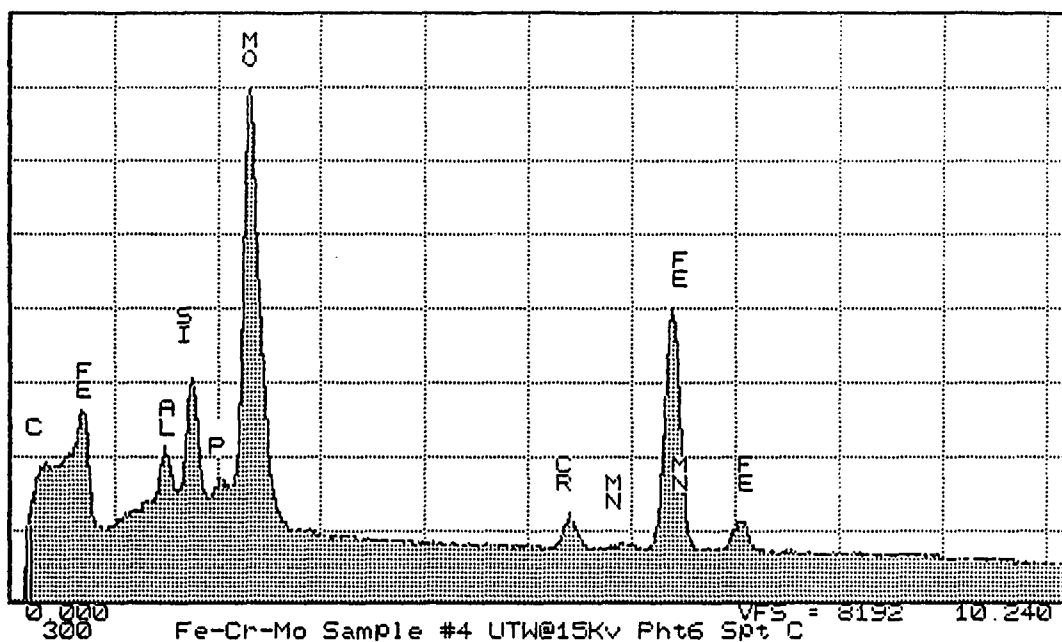
ZAF CORRECTION 14.95 KV 35.00 Degs

No. of Iterations 0

----	K	[Z]	[A]	[F]	[ZAF]	ATOM.%	WT.%
FE-K	0.940	0.999	1.004	1.000	1.003	95.08	95.27
CR-K	0.043	0.998	1.007	0.790	0.794	3.79	3.52
MO-L	0.008	1.089	1.149	0.996	1.248	0.62	1.07
SI-K	0.000	0.890	1.730	0.999	1.539	0.00	0.00 G *
O -K	0.000	0.855	1.689	0.999	1.445	0.39	0.11 *
C -K	0.006	0.839	0.046	0.999	0.039	0.12	0.03

* - High Absorbance

Fig. 47. (Continued) (b) at spot B.



SEMI-QUANTITATIVE ANALYSIS: Fe-Cr-Mo Sample #4 UTW@15kv Pht6 Spt C
EL NORM. K-RATIO

FE-K 0.44512 +- 0.00210
CR-K 0.00000 +- 0.00000
MO-L 0.32991 +- 0.00129
SI-K 0.02085 +- 0.00019
O -K 0.03069 +- 0.00026
C -K 0.17340 +- 0.00117

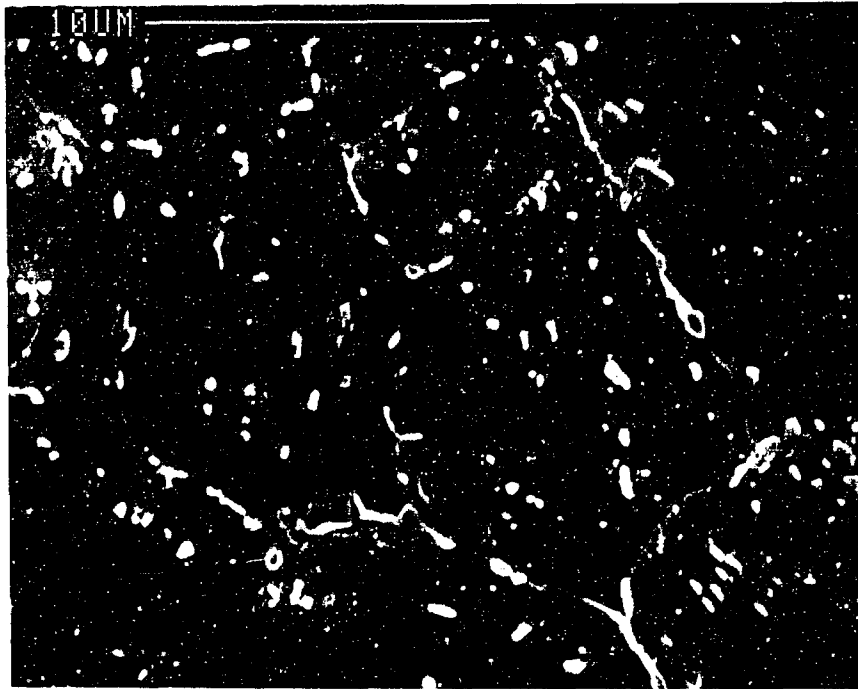
ZAF CORRECTION 14.95 KV 35.00 Degs

No. of Iterations 2

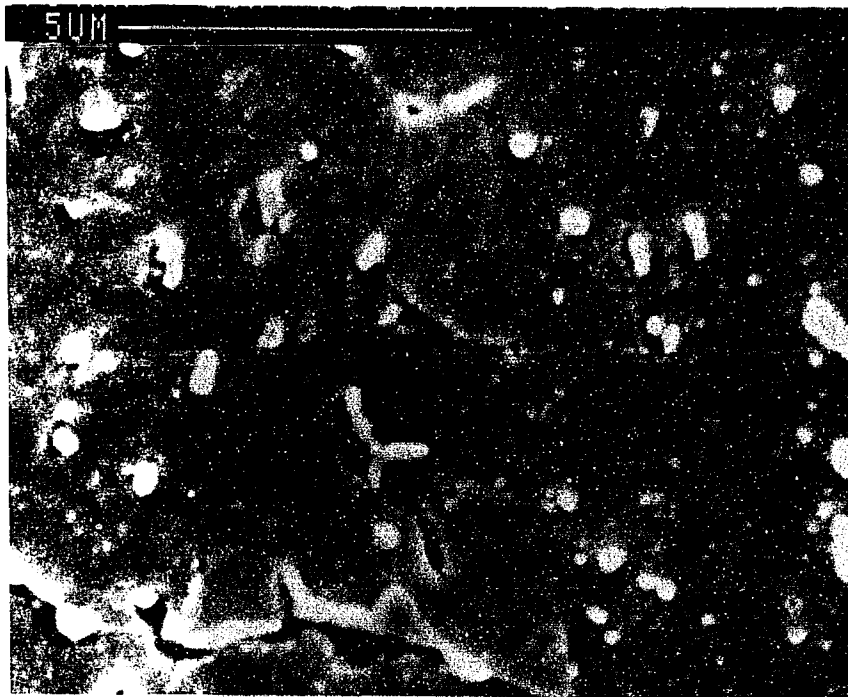
----	K	[Z]	[A]	[F]	[ZAF]	ATOM. %	WT. %
FE-K	0.445	0.977	1.024	1.000	1.001	37.34	45.21
CR-K	0.000	0.978	1.048	0.935	0.959	0.00	0.00 G
MO-L	0.329	1.092	1.077	0.998	1.175	18.94	39.32
SI-K	0.020	0.892	1.498	0.991	1.323	4.63	2.80 *
O -K	0.030	0.858	3.786	0.999	3.249	29.24	10.12 *
C -K	0.173	0.841	0.172	0.999	0.144	9.84	2.55

* - High Absorbance

Fig. 47. (Continued) (c) at spot C.

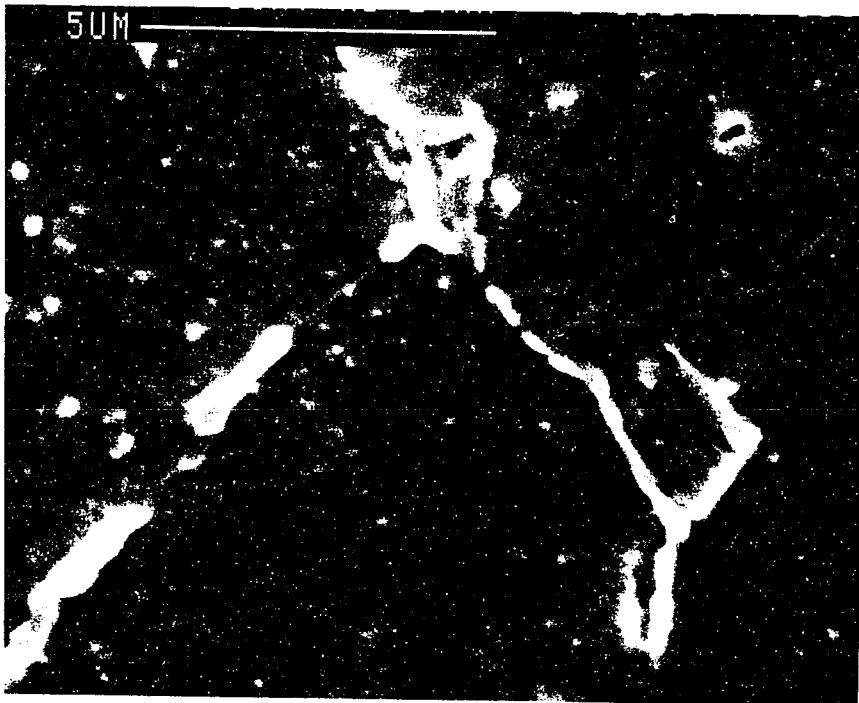


(a)



(b)

Fig. 48. Grain boundary cavitation observed on Sample 1 (a) with magnification of 3160, (b) with magnification of 6540.



(C)

Fig. 48. (Continued) (c) with magnification of 6540.

During the metallurgical study, it was found that grain boundary cavities were much easier to identify on the sample from the inside layer than that from outside layer. This indicated that creep damage were more severe on the inside than on the outside. This conclusion was in agreement with our expectations based on the thermomechanical history of the material.

Table 9. Chemical composition of structure features on fracture surface.

Element (Wt%)	Base Material	A	B	C
Fe	96.83	97.13	95.27	45.21
Cr	2.16	2.76	3.52	0.00
Mo	0.06	0.00	1.07	39.32
Si	0.24	0.00	0.00	2.80
O	0.63	0.10	0.11	10.12
C	0.08	0.02	0.03	2.55

DISCUSSION

Creep Analysis

During the creep process, impurities and dislocations are believed to segregate out of the grains and accumulate on grain boundaries. As this process continues, two effects on microstructure are introduced: (1) The density of defect, such as impurities, inside materials is decreased; (2) as impurities accumulate on grain boundaries, grain boundary cavities are nucleated and developed. It is known that when a domain wall interacts with an impurity (or other kinds of defect), the magnetostatic energy of the wall is reduced, and therefore, the impurity impedes the domain wall motion. As the defect density decreases during the creep process, the domain wall experiences less pinning and hence a lower coercivity of the material is expected. Also, as grain boundary cavities nucleate and develop, local demagnetization fields form in the vicinity of the cavities. Besides, cavities can also act as domain nucleation sites for magnetization reversal. Therefore, as creep damage continues, the remanence is expected to decrease.

Of two external primary factors (stress and temperature) which determine creep damage, stress is the major factor accounting for the different degree of creep damage for both sets of specimens under this investigation. In specimens from Set I, the thermal histories of three steam pipes were the same, while the stress history of each pipe was different. When in service, Sample C experienced the highest level of stress, Sample D experienced the lowest level of stress while Sample B had an intermediate stress level [13]. In specimens from Set II, the service temperature of the pipe was essentially uniform across the diameter

varying by perhaps one or two degrees Celsius, as the pipe was operated under heavy insulation. However, the stress inside the pipe was not uniform. When the pipe was in operation, the pressure on the inside wall of the pipe was much higher than that one on the outside wall, and therefore, the stress experienced by the inside layer was consistently higher than that of outside layer [15].

Analysis of Magnetic Measurement

Within each set of specimens investigated, the chemical composition of samples was similar. Therefore it was assumed that the difference in magnetic properties was mainly due to the difference in their microstructures resulting from the different degree of creep damage.

Since creep damage increases with applied stress at a fixed temperature or within same thermal history, a general decrease in coercivity from Sample C to B to D in specimen of Set I and from outside to inside pipe wall in specimen of Set II were expected. This agrees with magnetic measurements. In Set I, according to the remaining service life, Sample B and C were believed to be in their later stages of creep damage. In Sample C, significant grain boundary cavitations were observed [13]. As grain boundary cavitation increases, the demagnetization field due to the cavities will increase, and a consequent decrease in remanence occurs. A general decrease in remanence from Sample C to B to D were also observed, which is consistent with this interpretation.

However, in specimens of Set II, no significant decrease in remanence was observed from the outside layer of pipe to the inside layer. Using the fact that remanence and maximum flux density remained constant from inside to outside, one might interpret that this

material was in an early stage of creep damage, since no significant local demagnetization effects were present. Metallurgical examination corroborates this explanation since no detectable amounts of cavitation were seen on optical micrographs. Even under SEM with high resolution, grain boundary cavitation was very difficult to locate.

Although the decrease in coercivity could be caused by increasing residual tension remaining inside the pipe wall after being taken from service, the expected corresponding remanence increase with tension [7,16] did not occur. Therefore residual stress could not be the cause of the decrease in coercivity. It is concluded that the behavior of the coercivity could be an indication of early creep damage, in which the first changes are a decrease of pinning site density in the grains, as defects begin to migrate to the grain boundaries and later coalesce to form cavities.

PHYSICAL MODEL AND NUMERICAL CALCULATION

Cavities produced by creep damage inside a magnetic material will produce a demagnetization field $H_d = -DM$ which tends to oppose the applied field H , resulting in an effective field

$$H_e = (H + \alpha M) + H_d \quad (23)$$

inside the bulk material. The αM term in the effective field is produced by the interaction of domains, according to the Jiles-Atherton model [12]. The constant D is smaller or larger depending on the volume fraction of the material occupied by cavities. Thus,

$$D = k_1 (V_c/V) \quad (24)$$

where V_c/V is the volume fraction that is cavities and k_1 is a constant.

Also, during creep, defects (impurities and dislocations) tend to move to and pile up on the grain boundaries. This is accompanied by a reduction of pinning site density inside the grains and hence a reduction of k , the pinning strength. Thus, the effective pinning strength after creep damage is

$$k^* = k(1 - k_2 (V_c/V)) . \quad (25)$$

We note that reduction in pinning strength, according to this, results from an increase in cavitation.

Eqs. 24 and 25 form a simple model, which can be tested against experimental data from specimens of Set I. Clearly, for a very large amount of creep damage, with V_c/V

approaching a fraction sufficiently close to 1, one might expect a deviation from the linear relationships seen in Eqs. 24 and 25.

If one substitutes the above relationships into the Jiles-Atherton model [12], one finds that magnetization is given by

$$M = M_i + c(M_a - M_i) \quad (26)$$

where c is a constant equal to the ratio between the initial permeability and the anhysteretic permeability in the demagnetized state. M_i is the irreversible contribution to the magnetization due to domain wall pinning and unpinning and is found by solving the differential equation

$$\frac{dM_i}{dH} = \frac{M_a - M_i}{\frac{k^* \delta}{\mu_0} - \alpha^* (M_a - M_i)} \quad (27)$$

where $\delta = \pm$, depending on whether field H is increasing or decreasing, and where

$$\alpha^* = \alpha - D \quad (28)$$

M_a is the anhysteretic magnetization and is given by

$$M_a = M_s (\coth(H_e/a) - a/H_e), \quad (29)$$

where a is a constant which scales the effective field. Eqs. 26 -29 parallel those of Jiles and Atherton, but with the substitution of α^* for α and k^* for k in the original Jiles-Atherton equations.

Numerical substitution into the model produces the predictions for coercivity and remanence seen in Fig. 49(a) and (b) as functions of cavity volume fraction V_c/V . It is seen

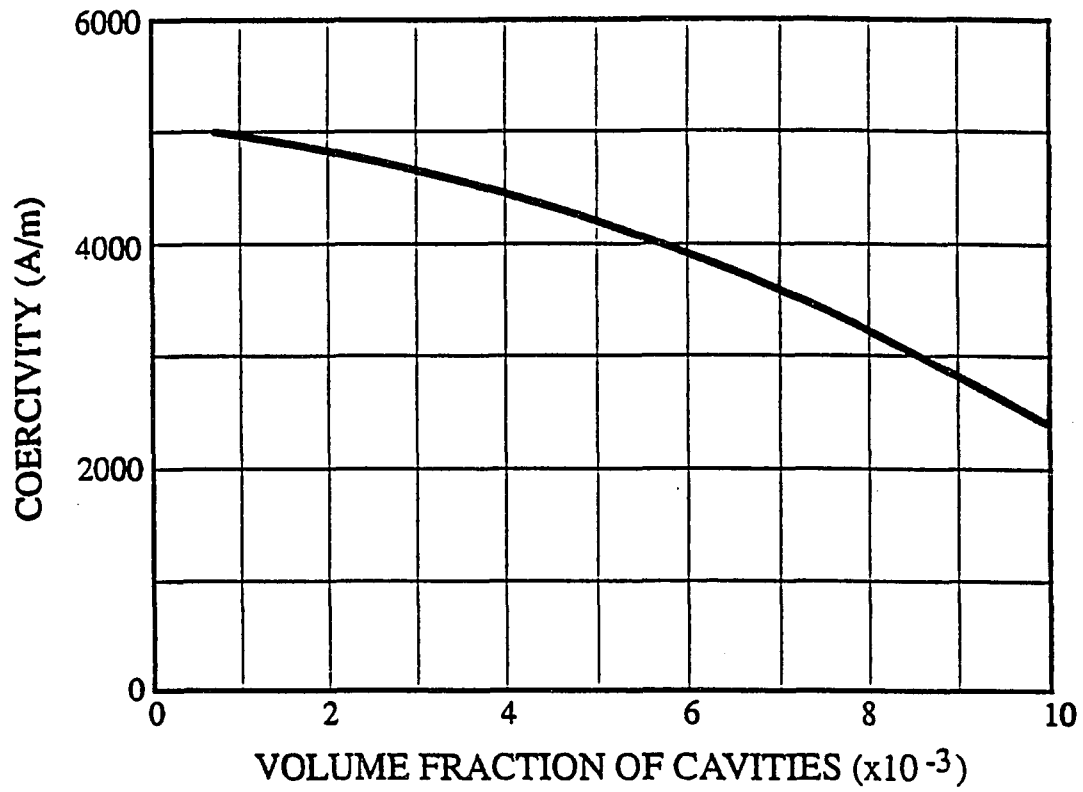


Fig. 49. Magnetic properties as a function of cavity volume fraction (a) coercivity.

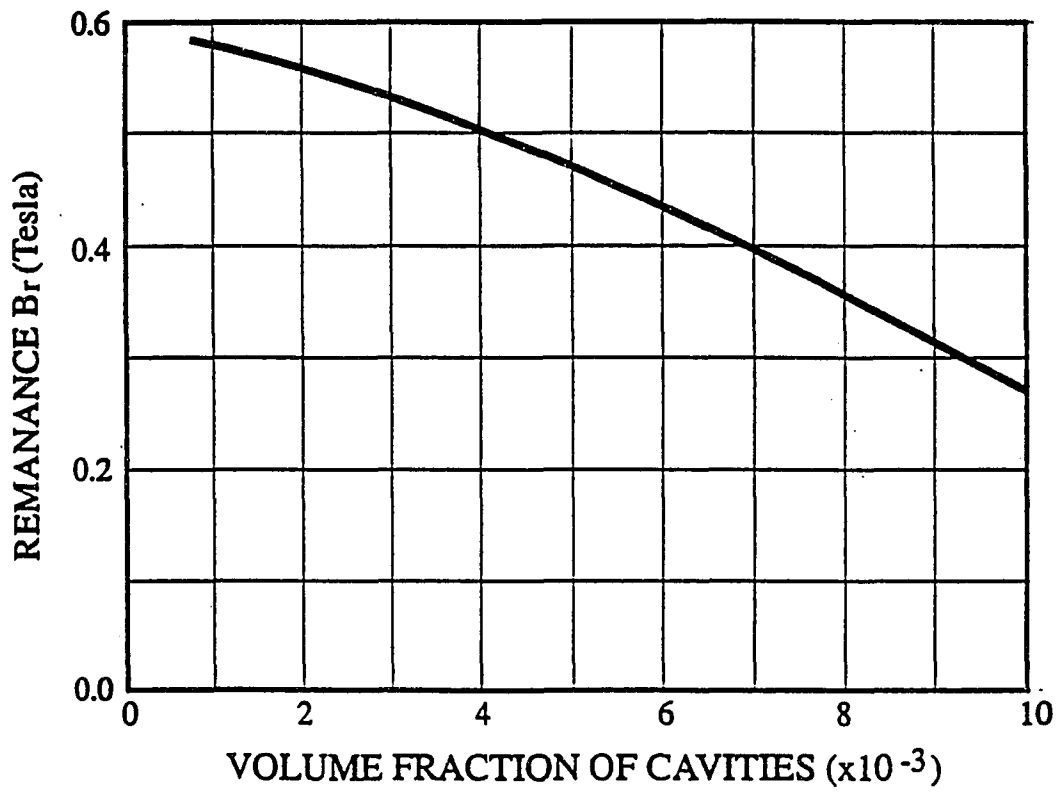


Fig. 49. (Continued) (b) Remanence.

that increase in cavity volume fraction, and concurrent decrease in pinning site density in the grains, leads to a simultaneous decrease in remanence and coercivity. This is unlike the magnetic effects of stress, which causes opposite changes in remanence and coercivity. For example, in steels an increase in compression causes remanence to decrease, but causes coercivity to increase [7,16].

The experimental results indicate that creep damage tends to cause a decrease in both remanence and coercivity, which is in an agreement with the theoretical model. Since hysteresis loss is proportional to both remanence and coercivity, the hysteresis loss also decreases with creep damage.

CONCLUSIONS

Magnetic hysteresis measurements have been investigated as an NDE method for detection of creep damage in Cr-Mo steel. Test results showed that coercivity, remanence and hysteresis loss can be used to characterize creep damage, even in the early stages of the creep process. The decrease of coercivity, remanence and hysteresis loss can be explained by the reduction in pinning sites for the domain wall motion and by the introduction of demagnetization effect due to a distribution of voids. A numerical calculation based on an extension of the Jiles-Atherton model and its proposed mechanisms was presented to describe the trends in the data.

REFERENCES

1. D.S. Wilkinson and V. Vitek, *Acta Met.* 30, 1723 (1982).
2. S.B. Biner and D.S. Wilkinson, Time dependent fracture, (Edited by A.S. Krausz, Martinus Nijhoff Publishers, Boston, 1985), p. 1.
3. B.M. Strauss, *Hydrocarbon Processing*, 68(10), 77 (1989).
4. N.L. Loh, *Brit. J. NDT*, 31, 437 (1989).
5. D.C. Jiles and J.D. Verhoeven, Review of Progress in Quantitative Nondestructive Evaluation (Edited by D.O. Thommpson and D.E. Chimenti, Plenum Press, New York, 1987) 6, p. 1681.
6. D.L. Atherton and D.C. Jiles, *NDT International*, 19, 15 (1986).
7. M.J. Sablik, S.W. Rubin, D.A. Kaminski, D.C. Jiles and S.B. Biner, *J. Appl. Phys.* 74, 480 (1993).
8. D.J.Bracci, D.C. Jiles and O. Buck, Review of Progress of Quantitative Nondestructive Evaluation (Edited by D.O. Thommpson and D.E. Chimenti, Plenum Press, New York, 1987) 6, p. 1395.
9. M.K. Devine and D.C. Jiles, *IEEE Trans. Mag.* Mag-29, 2465 (1992).
10. R.M. Govindaraju, M.K. Devine and D.C. Jiles, Final project report for Ontario Hydro Power Co., Toronto, Canada.
11. A. Mitra, Z.J. Chen and D.C. Jiles, To be published in Review of Progress of Quantitative Nondestructive Evaluation.
12. D.C. Jiles and D.L. Atherton, *J. Magn. Magn. Mater.* 61, 48 (1986).
13. Private conversation between Z.J. Chen of Ames Laboratory, Ames, Iowa and Dan Nass of Arizona Public Service Company, Phoenix, Arizona.
14. D.C. Jiles, S. Hariharan and M.K. Devine, *IEEE Trans. Mag.* MAG-26, 2577 (1990).
15. S.P. Timoshenko and J.N. Goodier, Theory of elasticity (McGraw-Hill Book Company, New York, 1969).

16. M.J. Sablik and D.C. Jiles, IEEE Trans. Mag. MAG-29, 2113 (1993).

PART IV.

**PRACTICAL TECHNIQUES TACKLING PROBLEMS IN SURFACE
MAGNETIC HYSTERESIS MEASUREMENT**

INTRODUCTION

Surface inspection of magnetic properties by a two-pole magnetic surface sensor is a useful and practical technique because it is a rapid, non-invasive and requires minimum material preparation. Recently, work has been performed on the application of this technique to the detection of fatigue damage [1], creep damage [2] and stress effects [3]. However, this technique is handicapped by the practical problem of calculating the intrinsic magnetic properties of the material from such a measurement. The problem arises from the flux leakage effect, non-uniform field distribution inside test specimen and the lift-off effect. These effects make the measurement of B and H fields extremely complicated under these circumstances

Most of the flux leakage effects arise from the discontinuity of magnetic properties. In the past, the detection of magnetic leakage field has found its application in the detection of surface flaws [4] and stress [5], either by visual techniques such as magnetic particle [6] or magnetometers [7, 8]. However, in a c-shaped inspection head, the flux leakage effect invalidates the assumption of flux continuity, which means that the total flux inside the inspection head is not the same as that inside test specimen. Therefore, the determination of the amount of flux leakage is important in calculating the flux and hence the magnetic induction B field in the test specimen. In this paper, an experimentally determined parameter is defined to calibrate the flux leakage inside the inspection head. As a result, within the first approximation, which assumes that the magnetic flux inside test material is uniform, a transfer function has been derived for correction of flux leakage effects.

The geometry effect manifests itself by presenting different B-H curves for different geometries of the test samples or inspection heads, even when the intrinsic magnetic properties of the test specimens and inspection heads are the same. This is mainly due to the non-uniform field distribution inside the test specimen, which is a more general case than the first approximation. It is believed that the distribution of magnetic field is determined by the effective magnetic pole strength of the inspection head and geometries of both the test specimen and the inspection head. In the present work, a simple physical description of the field distribution inside the specimen is presented. This model is analytic and based on the apparent surface magnetic charge. Although a more precise description should be based on finite element methods, this simple model enables us to get a transfer function with geometrical corrections to the first order.

The lift-off effect causes changes in the magnetic measurements due to the positioning of the inspection head with respect to the test specimen. It can also be due to the difference in surface condition of specimens. In most NDE applications, where the relative changes in magnetic properties are more important than their absolute value, the lift-off effect plays a more important role than flux leakage and geometry effects. In the recent field testing for the assessment of creep damage [9], Govindaraju et al. found that although the general trend in magnetic properties could be correlated with creep effects, the overwhelming fluctuation due to lift-off effects, and possibly other effects detrimental to the test result, precluded a definite conclusion. A similar problem was also found in the field testing of stress effects [10]. However, as with the demagnetization effect, lift-off is not always detrimental and it can be utilized to improve the surface inspection by reducing the influence

of the surface condition. In this paper, it will be shown that the lift-off problem can be resolved by two new techniques: using a magnetic coupling gel and pre-lifting the probe a certain known distance above the specimen. Analytic magnetic circuit modelling supports this conclusion.

The following discussion consists of two parts. Section A focuses on the problem of deriving a transfer function with the correction of flux leakage and geometry effects. Section B addresses the effect of lift-off on the measurement result, and concentrates on the techniques to reduce the measurement variation and thereby maximizing intrinsic specimen information.

A. DEVELOPMENT OF TRANSFER FUNCTION TO MEASURE INTRINSIC MAGNETIC PROPERTY FROM SURFACE INSPECTION

Background

The most precise hysteresis measurement of the hysteresis curve of a material is performed in a closed magnetic circuit, which could be a ring-shape specimen as shown in Fig. 50. In a closed magnetic circuit, there is no macroscopic demagnetizing field, and therefore, it is fairly easy to calculate both the H and B fields in the material. However, in practice, especially in NDE applications, minimal material preparation is a prerequisite and this means that it is usually not possible to provide closed circuit specimens consisting all of the same material.

The most convenient way of making a hysteresis measurement is to directly contact an inspection head with a power coil, a flux coil and a Hall probe on the test material (see Fig. 51). The power coil is used to provide driving magnetic field, the Hall probe measures magnetic field on the sample surface H_{surface} and the flux coil measures the magnetic flux B_h inside the inspection head. In the case of a surface inspection, the field distribution can be quite complicated. An example of the magnetic flux distribution under these circumstances has been calculated by finite element method and this is shown in Fig. 52. The difficulty of extracting the intrinsic hysteresis curve from a surface measurement arises mainly from two effects: flux leakage and non-uniform field distribution.

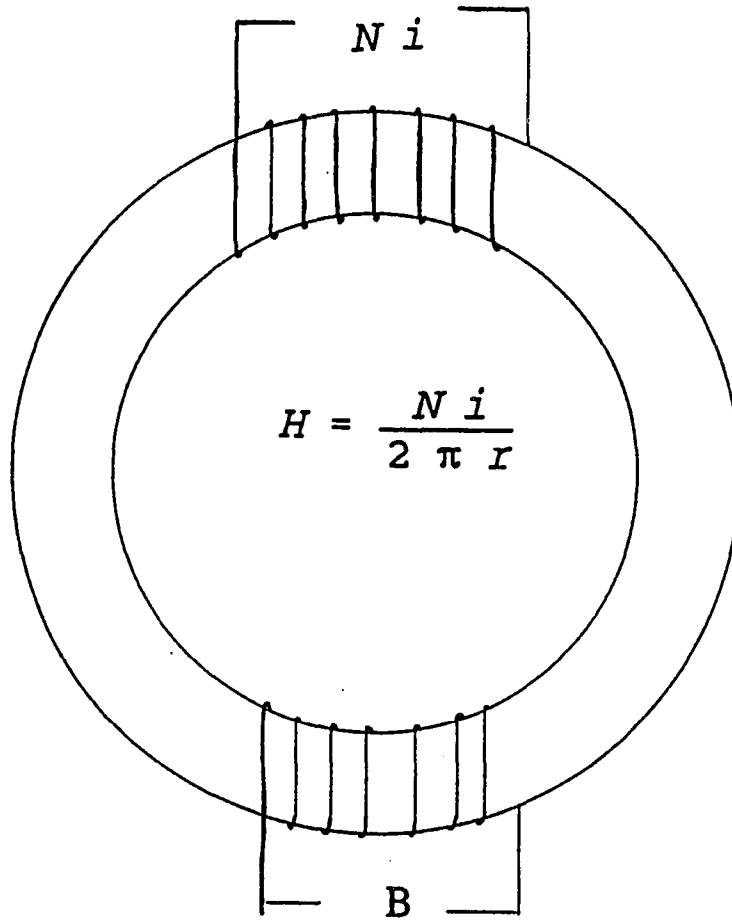


Fig. 50. Magnetic hysteresis measurement on a ring specimen.

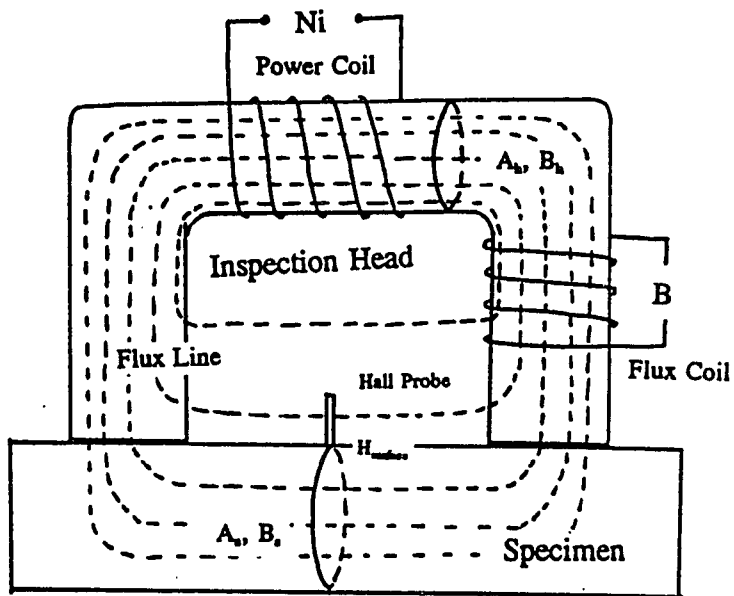


Fig. 51. Magnetic hysteresis measurement using a surface inspection head.

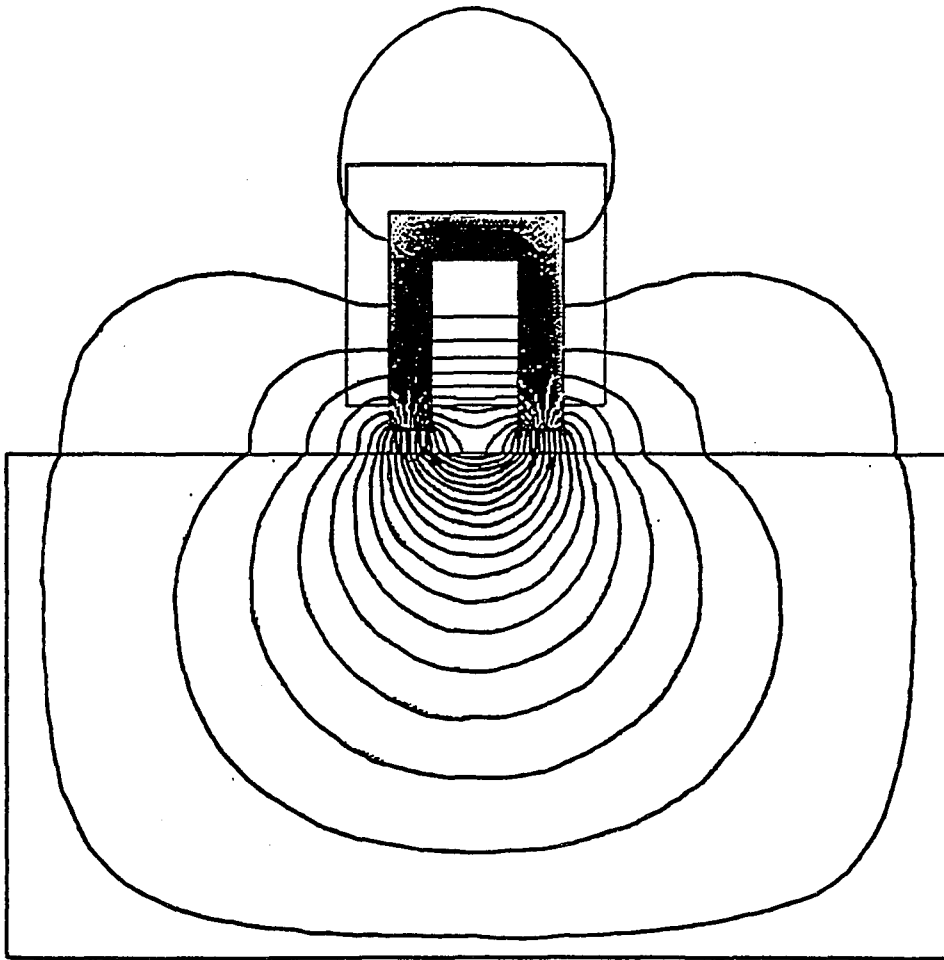


Fig. 52. Magnetic flux distribution calculated by finite element method.

First Approximation and Leakage Coefficient

The purpose of deriving a transfer function of the inspection head/material magnetic circuit is to express the magnetic flux density B_s and magnetic field H_s inside a test sample (which are not directly measurable), in terms of two directly measurable quantities which are flux density inside the inspection head B_h and magnetic field on the surface of the sample $H_{surface}$. Due to the discontinuity of the magnetic circuit at the interface and non-uniform distribution of magnetic field inside the test material, this is a quite complicated problem. Even when finite element methods are used, it is difficult to get a rigorous numerical solution. However, within the first approximation, which assumes that B and H fields inside samples are uniform, this problem can be solved. From Fig. 51, the measured magnetic quantities, $H_{surface}$ and B_h are related to H_s and B_s by the following equations:

$$H_s = H_{surface} \quad (30)$$

$$B_s = B_h \times \frac{A_h}{A_s} \quad (31)$$

where A_h , A_s are the cross sectional area of inspection head and sample respectively. The first equation comes from the assumption of uniformity of H field inside the test sample and the continuity of the tangential component of H field. The second equation comes from the continuity of flux. However, some flux leakage always occurs in magnetic circuits involving surface inspections. Therefore, both Eq. (30) and Eq. (31) need to be made more sophisticated for practical applications.

Due to leakage field between the legs of inspection head, the magnetic field detected

on the surface of a sample will always be a little larger than that inside the sample. By using a Hall plate of high spatial resolution and mounting it in such a way that close contact with the sample surface is assured, and with wide separation of the legs of the inspection head, the H field measured by Hall probe can be thought as $H_{surface}$. Nevertheless Eq. (31) needs modification. The actual flux inside the test material is only a portion of the flux inside inspection head. A parameter called leakage coefficient η is defined as the ratio of total flux inside sample to total flux inside inspection head to characterize the efficiency of inspection head. Therefore the transfer function turns to be:

$$H_s = H_{surface} \quad (32)$$

$$B_s = \eta \times B_h \times \frac{A_h}{A_s} \quad (33)$$

Surface Magnetic Charge Model

Magnetic field distribution By contacting a two-pole magnetic inspection head on a test material (see Fig. 53), a magnetic circuit is formed. The field distribution inside the material is significant for magnetic measurement. Due to the discontinuity of the magnetic circuit at the interface of the inspection head and the test material, we can consider from a phenomenological viewpoint that surface magnetic charges are formed. This problem is similar to the electric field distribution inside a material due to two electric charges, and therefore the two calculations can be treated as analogous. If the thickness of the test material is very large compared with the distance between the two charges, then the

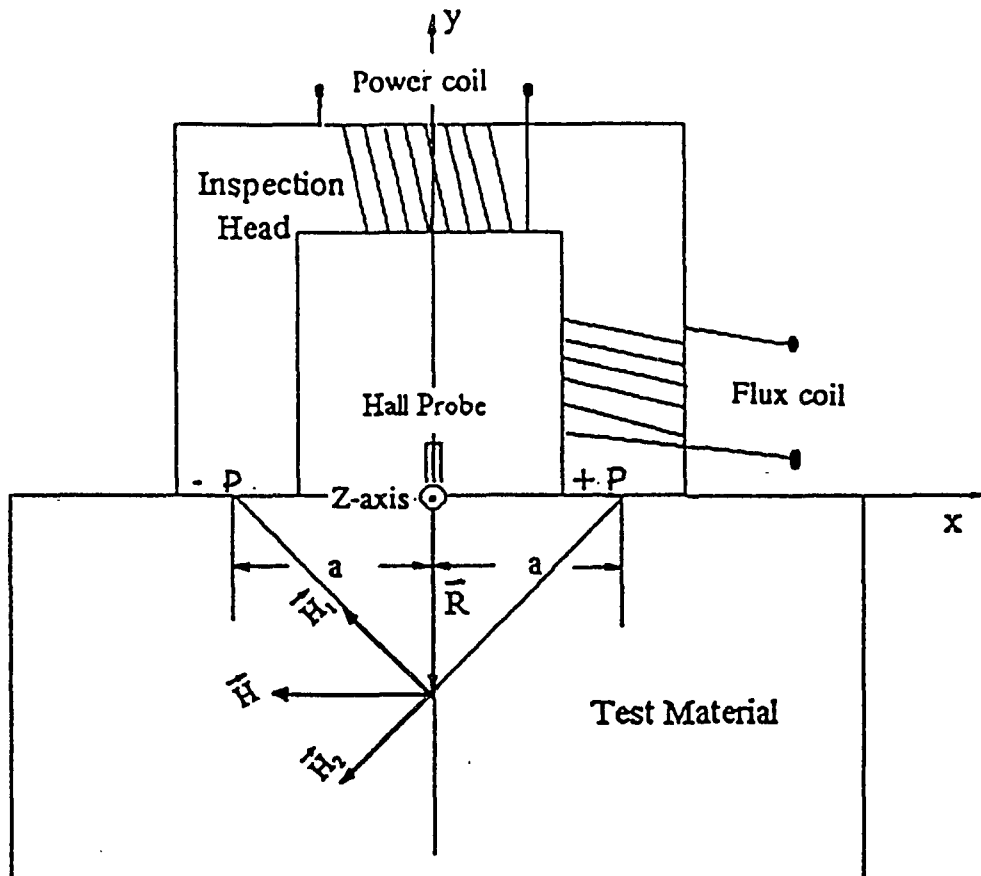


Fig. 53. Surface magnetic charge model. The coordinate system is defined so that two poles of inspection head are along x-axis, y represents the depth of the material and z parallel the surface of the test material.

boundary condition for field distribution on the far surface can be approximately treated as:

$$\lim_{R \rightarrow \infty} H(R) = 0 \quad (34)$$

Thus the magnetic field in the half space of the test material is:

$$\begin{aligned} H(\mathbf{R}) &= \frac{1}{4\pi} \int \frac{\mathbf{r}}{|\mathbf{r}|^3} dP \\ &\approx \frac{1}{4\pi} \frac{P}{|\mathbf{R}-\mathbf{a}|^3} (\mathbf{R}-\mathbf{a}) - \frac{1}{4\pi} \frac{P}{|\mathbf{R}+\mathbf{a}|^3} (\mathbf{R}+\mathbf{a}) \end{aligned} \quad (35)$$

where P (in units of A.m) is magnetic pole strength. If the inspection head is aligned on x-axis, then the field along y-axis in the lower half space is:

$$\begin{aligned} H(y) &= \frac{2a}{4\pi} \frac{P}{(\sqrt{a^2+y^2})^3} \mathbf{x} \\ &= H(0) \frac{a^3}{(\sqrt{a^2+y^2})^3} \mathbf{x} \end{aligned} \quad (36)$$

where H(0) is the surface field when y=0. In the above derivation, the influence of volume magnetic charge $\rho = -\mu_0 \nabla \cdot \mathbf{M}(\mathbf{r})$ on the magnetic field inside the test specimen is neglected for simplicity.

Field penetration depth and average permeability From (7), it can be seen that the magnetic field is not uniform inside the test material. It decays as y increases. The penetration depth l_p is defined as the distance by which the magnetic field has decayed to 1/e of its surface value H(0). From this definition of penetration depth: $H(l_p) = H(0)/e$, it is found $l_p = 0.974 \times a \approx a$. Therefore, the penetration depth of the field depends on the distance between the two poles of the inspection head and is about half of the pole separation. This is a useful practical result for designing inspection heads for different depths

of penetration.

The permeability μ of ferromagnetic materials varies as a function of magnetic field during initial magnetization as shown in Fig. 54. This also shows magnetic field as a function of distance below the surface. Clearly, in surface magnetic inspection, μ is a function of y .

An average permeability μ_{avg} is defined on Fig. 54 so that $\mu_{avg} \times H(0)$ equals the area under $\mu(H)$ curve from 0 to $H(0)$. It can be seen that μ_{avg} depends only on $H(0)$. Here we define a dimensionless parameter β such that:

$$\mu(\beta a) = \mu(H) \mu_{avg} \quad (37)$$

Clearly, β is determined by $H(0)$ and will be a constant if we keep $H(0)$ fixed by adjusting the current to the power coil when surface measurements are taken.

Magnetic induction and flux Magnetic induction \mathbf{B} describes the response of the test material due to a magnetic field. It is the product of permeability and magnetic field. In our surface inspection case:

$$B(y) = \mu(H(y)) H(y) = \frac{\mu(H(y)) H(0) a^3}{(\sqrt{a^2 + y^2})^3} \quad (38)$$

The magnetic flux passing through the test material in the y - z plane is:

$$\Phi = \int_0^t B(y) dA = \int_0^t B(y) w dy \quad (39)$$

where t is the thickness of the test material in the y direction and w is the average width of flux distribution in the z direction, which is mainly determined by the width of the inspection

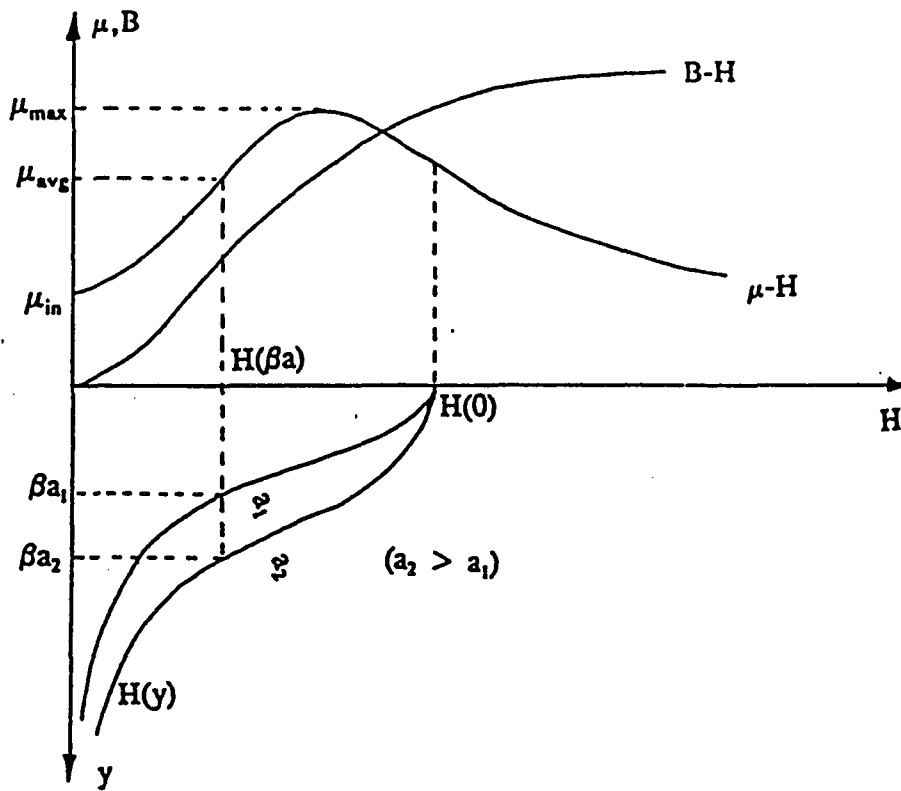


Fig. 54. Diagram of $\mu(H)$ curve and $H(y)$ curves.

head. So:

$$\begin{aligned}
 \phi &= H(0) w a^3 \int_0^t \frac{\mu(H(y))}{(\sqrt{a^2 + y^2})^3} dy \\
 &\approx H(0) w a^3 \mu_{avg} \int_0^t \frac{1}{(\sqrt{a^2 + y^2})^3} dy \\
 &= H(0) w a \mu(\beta a) \frac{t}{\sqrt{a^2 + t^2}}
 \end{aligned} \tag{40}$$

Considering the effects of flux leakage, the flux inside the material is a constant and is equal to the flux leakage coefficient η , times the flux inside inspection head.

$$\phi = k \times \phi_h = k \times A_h \times B_h \tag{41}$$

where ϕ_h , B_h , A_h are flux, flux density and area of inspection head. η the flux leakage coefficient is determined by the configuration of inspection head and its value is less than unity due to flux leakage from the inspection head primary across the two legs of the c core.

From Eqs. 40 and 41, we can obtain:

$$B_h = \frac{H(0) w a \mu(\beta a)}{\eta A_h} \frac{t}{\sqrt{a^2 + t^2}} \tag{42}$$

This equation therefore gives the relation between two measurable quantities B_h and $H(0)$ with correction for leakage η and making some other simplifying assumption about average permeability and average width of the flux path w in the y - z plane.

By slightly rearranging Eq. 42, we can obtain:

$$\mu(\beta a) = \frac{\eta A_h B_h}{H(0) w a} \frac{\sqrt{a^2 + t^2}}{t} \tag{43}$$

From Fig. 51, it can be seen that if $H(0)$ is fixed, β and $H(\beta a)$ are also fixed. Then the permeability of the material at the depth of βa and subject to magnetic field of $H(\beta a)$ can be

determined by two measurable quantities $H(0)$ and B_h . This result is useful in the measurement of permeability at different depths by adjusting the pole length of inspection head 2a.

Transfer Function with Flux Leakage and Geometry Correction

In practice the magnetic field is not uniform in the test materials, and the field measured is the value on the surface of the sample $H(0)$. Therefore in order to find the intrinsic B-H curve of the test specimen, we should calculate the magnetic induction at the same position on the surface $B(0)$. Assuming $B(0) \approx \mu_{\text{avg}} H(0)$, which is a reasonable approximation for soft magnetic materials, Eq. 42 can be rearranged as:

$$B(0) = \eta A_h B_h \frac{\sqrt{a^2 + t^2}}{w a t} \quad (44)$$

Finally, combining Eq. 30 with Eq. 43, we get the following transfer function:

$$H = H_{\text{surface}} \quad (45)$$

$$B = \eta A_h B_h \frac{\sqrt{a^2 + t^2}}{w a t} \quad (46)$$

Test Results and Discussions

Flux leakage The test configuration is shown in Fig. 55. In order to check the flux inside the magnetic circuit, two additional flux coils of 25 turns were wound one on the test sample and another on the leg of the inspection head. The Magnescope [11] was used to

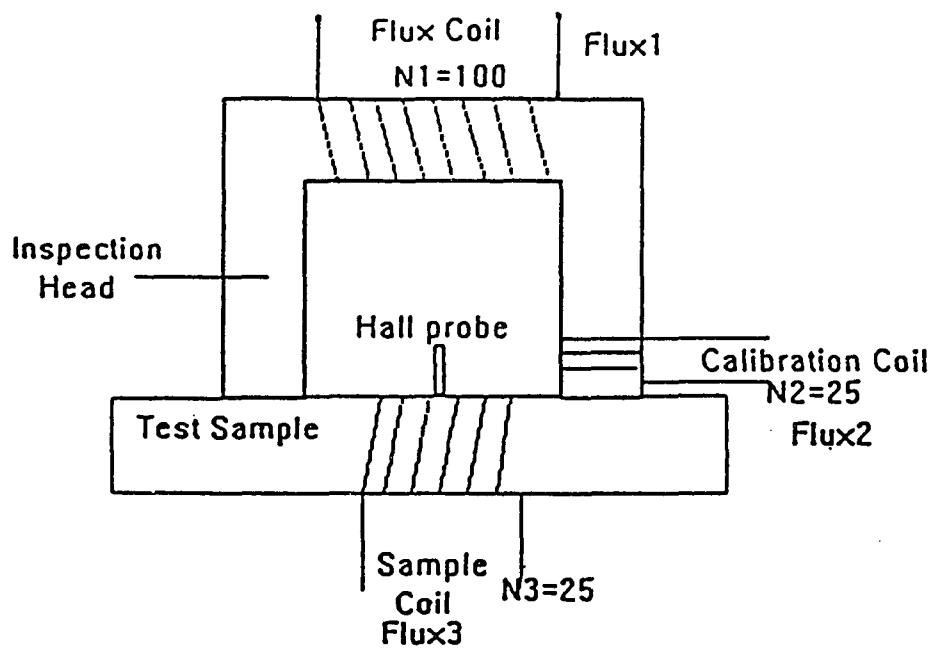


Fig. 55. Configuration of flux leakage test.

record hysteresis loops of B-H. By multiplying flux density B by cross section A, flux-H curves of magnetic flux ϕ versus magnetic field H were calculated for locations 1, 2, 3 on the magnetic circuit, which were identified as Flx1-H, Flx2-H and Flx3-H respectively. Flux continuity was checked in different test samples listed in Table 10. The relations between these curves were quite similar. A typical example of data, taken on sample 2, is shown on Fig. 56.

It was found that the flux inside inspection head in Location 1 was larger than that in Location 2 and Location 3, but the latter two were almost identical. Therefore, it is quite clear that the flux leakage occurred mainly inside the inspection head and the flux leakage at the discontinuity between inspection head and sample can be neglected. This is demonstrated in Fig. 52.

The leakage coefficient η was calculated according to the definition of $\text{Flx3}/\text{Flx1}$, which is the same as $\text{Flx2}/\text{Flx1}$. Values of η measured on different samples are shown on Fig. 57. It can be seen that the values of η are almost constant at about 80% regardless of the differences in geometry and material composition of the test samples. This indicates that the amount of flux leakage is determined mainly by the inspection head itself. Thus η is a parameter characterizing the efficiency of an inspection head.

While it is not always possible to wind a flux coil on a test sample in a practical situation, it is not difficult to wind a calibration coil in Location 2 to find the leakage coefficient of an inspection head before using the transfer function. Fig. 58 shows hysteresis loops from Sample 3. B-H curves from both direct measurement and as a result of calculations using the transfer function match each other excellently.

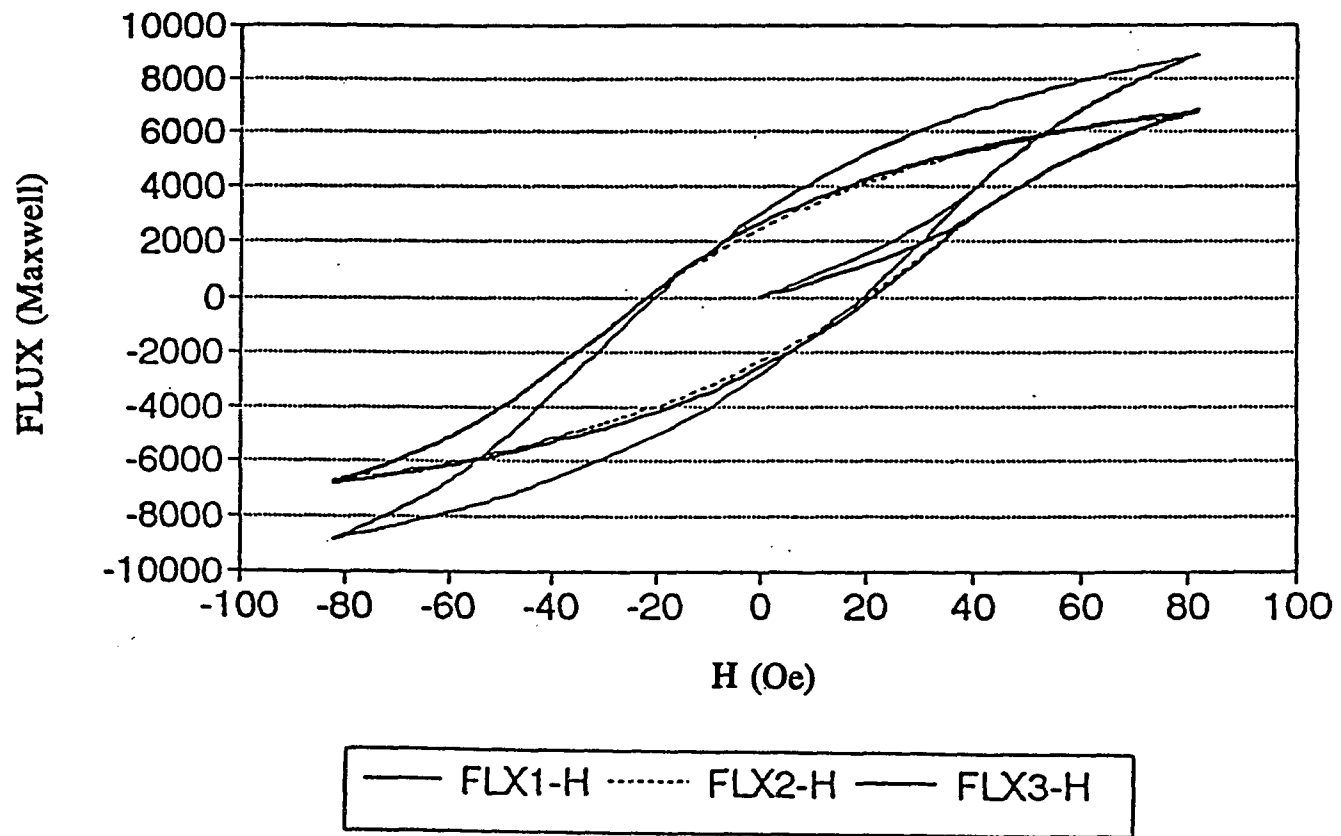


Fig. 56. Flux-H_{surface} loop in Location 1, 2, 3 of magnetic circuit.

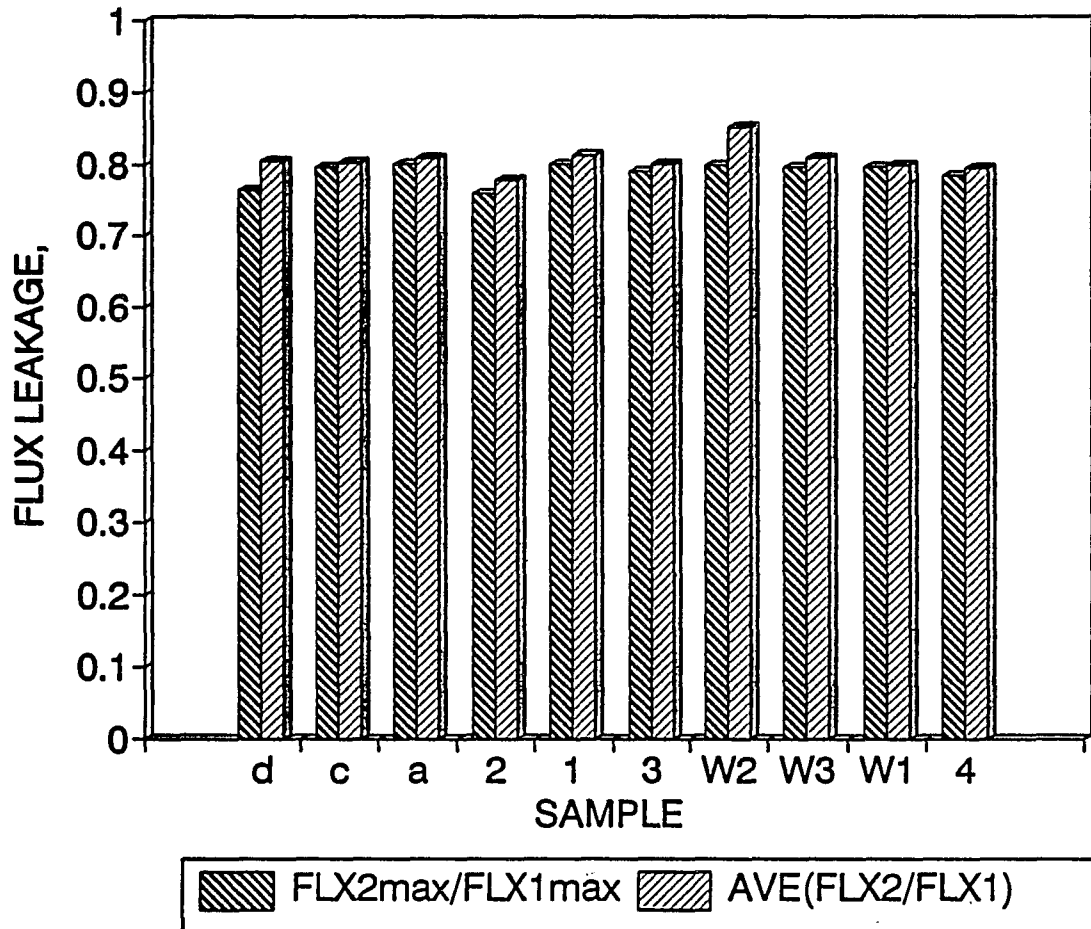


Fig. 57. Flux leakage coefficient for different samples. $Flx2_{max}/Flx1_{max}$ is the ratio of maximum value of $Flx2$ to maximum value of $Flx1$ on flux-H loop. $Ave(Flx2/Flx1)$ is average value of the ratio of $Flx2$ to $Flx1$ on the flux-H loop.

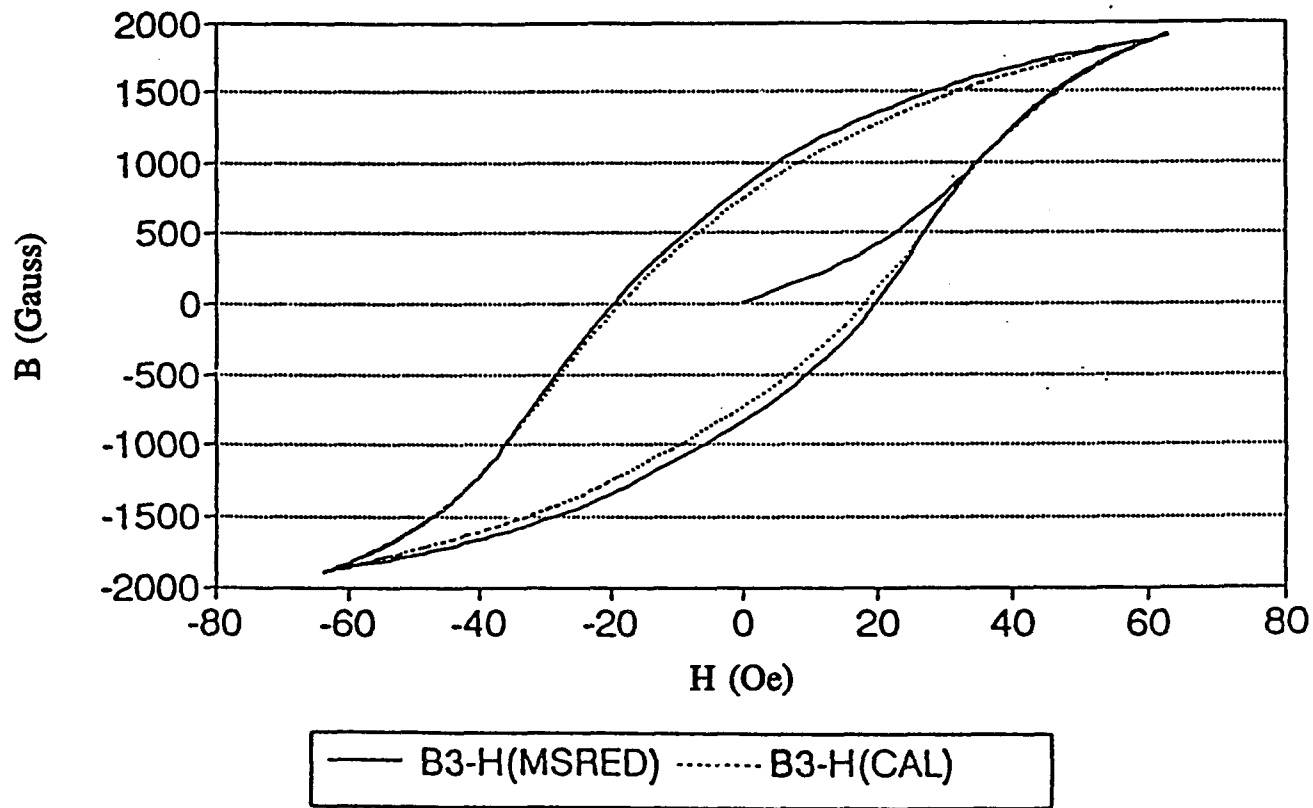


Fig. 58. Comparison of direct measurement and measurement calculated by first approximation.

Table 10. Test samples for flux leakage

Sample	Material (steel)	Area(cm ²)	Dimension
a	Armco	0.403	1"x1/4"x1/4"
c	Armco	0.202	1"x1/4"x1/8"
d	Armco	0.101	1"x1/4"x1/16"
1	Armco	2.420	3.15x2.64x0.93(cm ³)
2	Armco	2.420	irregular shape
3	Armco	3.760	irregular shape
4	Armco	8.840	7.3x3.4x2.6(cm ³)
W1*	medium carbon	5.000	long steel bar
W2*	medium carbon	4.550	long steel bar
W3*	medium carbon	4.990	long steel bar

* W1, W2, W3 have different composition

Limits of first approximation First approximation assumes magnetic flux passes through the cross-section of the inspection head uniformly. According to the surface magnetic charge model, both B and H inside a test material are distributed non-uniformly and this distribution is a function of $1/(y^2+a^2)^{3/2}$, where a is half of the distance between the poles of the inspection head and y is the distance from the surface of the test sample. According to this model, the penetration depth of the field, at which the magnetic field decays to 1/e of its surface value, is about 0.97a. Therefore, it can be seen that the first approximation, which gives B_s-H_s curves, works only when the thickness of test sample is less than half of the distance between the legs of the inspection head. When this dimension

of the test material is larger, an effective cross sectional area should be estimated in order to use the above transfer function. This can be achieved using the surface charge model.

Flux inside inspection head One direct result of this analytic model of magnetic field distribution is Eq. 42 which gives flux inside inspection head as a function of thickness t of test material and pole separation $2a$. Experiments were performed on a set of samples with different thickness. B_h was measured while $H(0)$ was kept fixed. Experimental data were then fitted by the theoretical function: $y/(a^2 + y^2)^{1/2}$ for two different inspection heads of pole separation of $2a=31.8$ mm and $2a=19.0$ mm respectively. For an inspection head with $2a=31.8$ mm, $H(y)$ was also measured and data were fitted by the function $1/(a^2 + y^2)^{3/2}$ according Eq. 36. Data are presented in Table 11 and the curve fitting results are shown in Fig. 59 to Fig. 61 (experimental points are for $y = t$). Results are in good agreement with the theory considering the finite dimension of the sample, which in this case was not even a very close approximation to the infinite boundary condition.

Correction for Geometry Effects The transfer function based on surface magnetic charge model is given by Eq. 45 and 46. Comparing this with the transfer function within the first approximation shown in Eq. 32 and 33, it can be see that the effective area of cross section of the test material is defined as:

$$A_{effect} = \frac{wat}{\sqrt{a^2 + t^2}} \quad (47)$$

This is a fairly reasonable result, because when the dimension of the specimen matches the inspection head, (i.e., $t \ll a$), then $A_{effect}=wt$, which is the physical cross section of the specimen. On the other hand, if the test material is very thick, (i.e., $t \gg a$), then $A_{effect}=wa$,

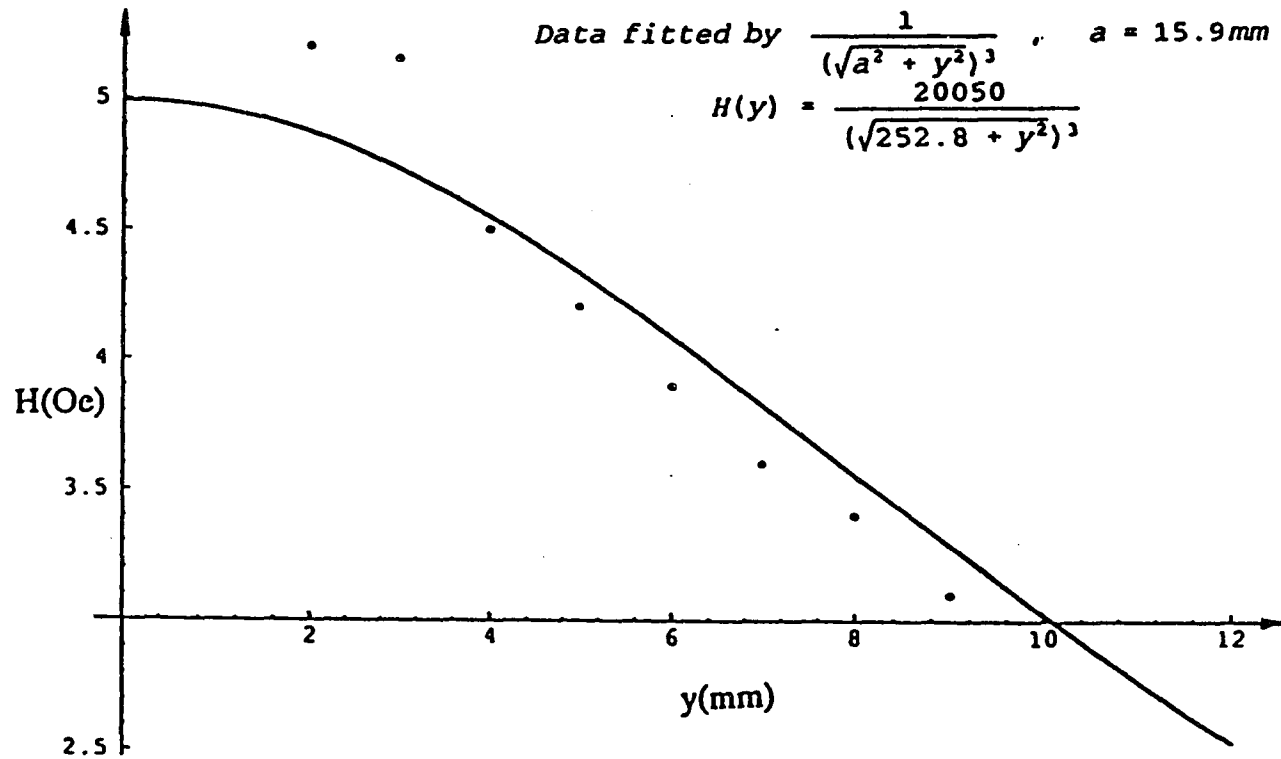


Fig. 59. Experimental data and curve fitting of magnetic field inside the material on y axis (use inspection head of a = 15.9 mm).

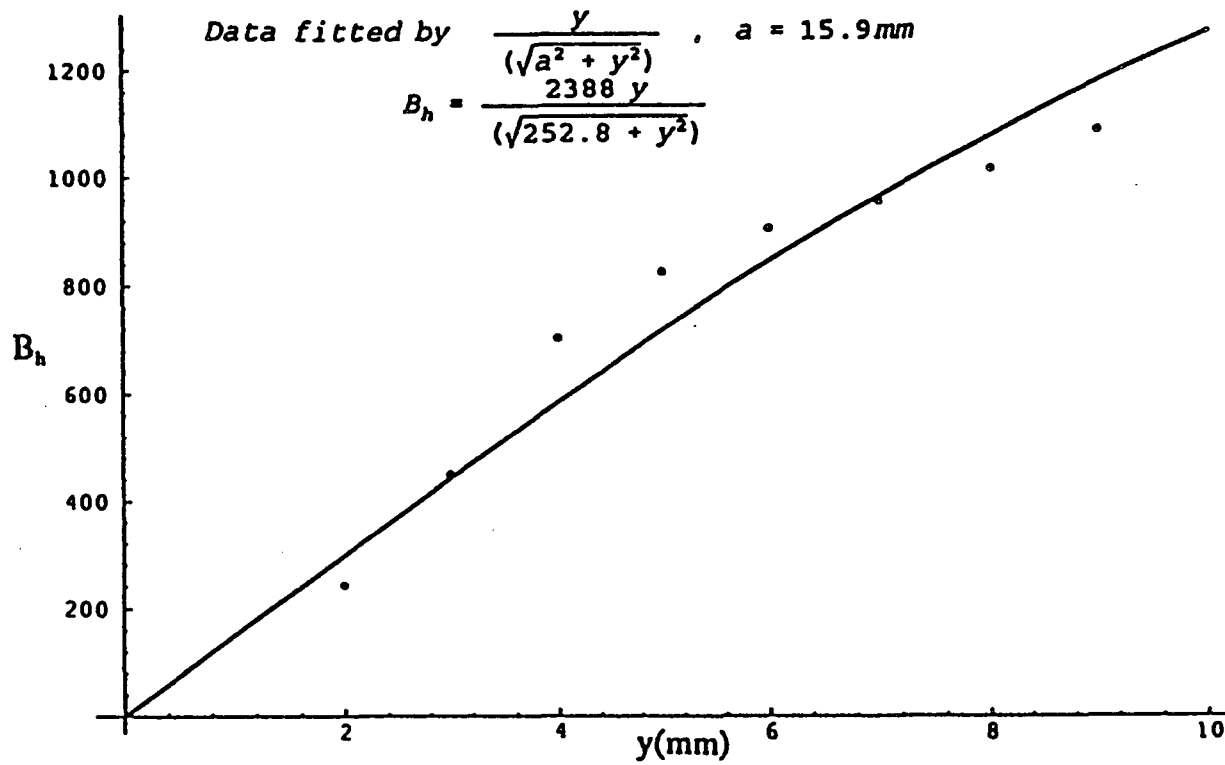


Fig. 60. Experimental data and curve fitting of flux density inside inspection head on specimen of different thickness (use inspection head of $a = 15.9\text{ mm}$).

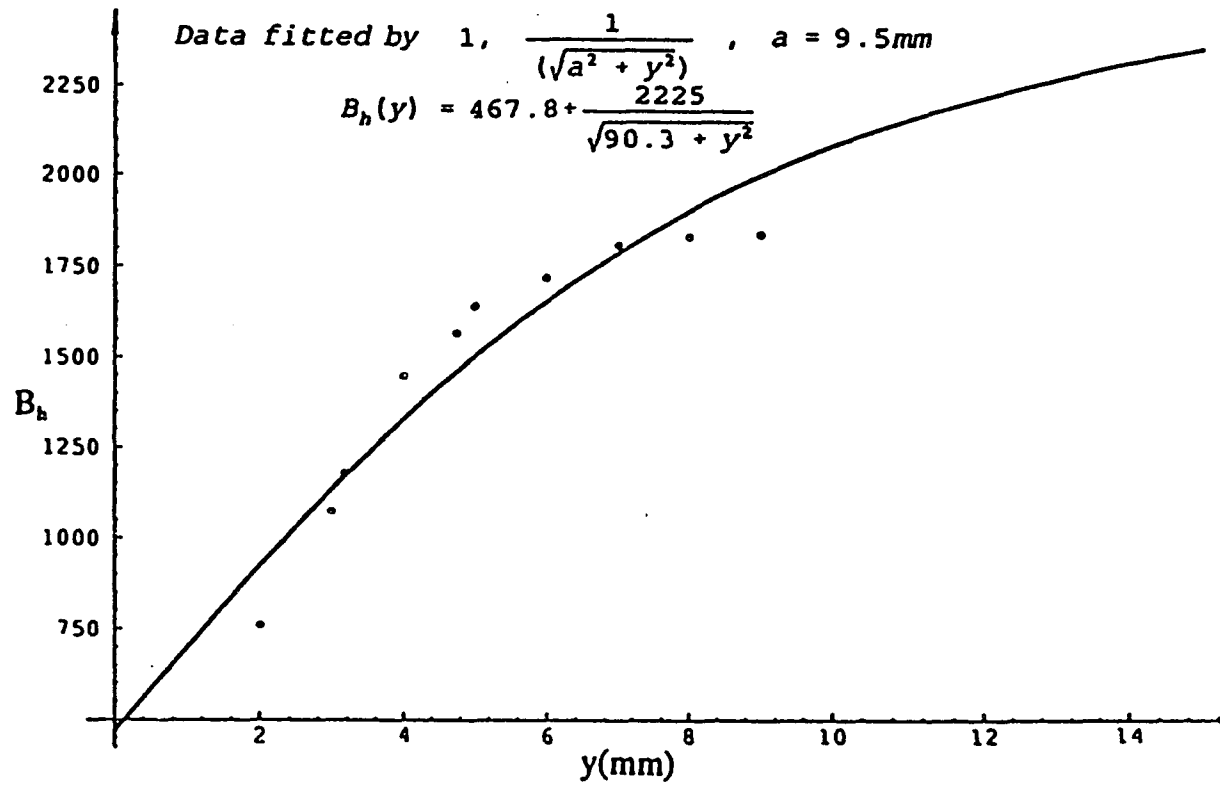


Fig. 61. Experimental data and curve fitting of flux density inside inspection head on specimen of different thickness (use inspection head of $a = 9.5$ mm).

Table 11. Measurements of B_h and $H(t)$ in samples of different thickness

H(0)=6 Oe				H(0)=18 Oe		
a=15.9 mm				a=9.53 mm		
Sample	t(mm)	B_h^*	H(t) (Oe)	Sample	t(mm)	B(t)*
T1	2.00	244	5.2	T1	2.00	761
T2	3.00	451	5.2	T2	3.00	1075
T3	4.00	702	4.5	TK1	3.18	1180
T4	5.00	825	4.2	T3	4.00	1448
T5	6.00	905	3.9	TK2	4.76	1565
T6	7.00	954	3.6	T4	5.00	1639
T7	8.00	1013	3.4	T5	6.00	1717
T8	9.00	1085	3.1	T6	7.00	1809
				T7	8.00	1831
				T8	9.00	1836

* relative value

where a is the penetration depth of the field.

Conclusions and Future Work

An transfer function for surface inspection has been derived with the objective of determining intrinsic magnetic properties from surface measurements. The current discussion has focused on the correction of the flux leakage and the geometrical effects. The flux leakage study has shown that although there is an inherent flux leakage inside an inspection head, this can be corrected for the amount of leakage. The correction is mainly determined by the configuration of the inspection head and can be characterized by a parameter called the leakage coefficient η . According to this idea, each inspection head should be tested first

to find the leakage coefficient before taking magnetic measurements. Although the first approximation works well when the thickness of the test sample is no larger than the penetration depth of the field, it is generally quite safe to say that, by taking the leakage coefficient into account, the flux inside a sample can be measured to a high degree of accuracy by this method.

The correction of geometrical effects is based on the surface magnetic charge model. According to this model, an analytic equation for magnetic field distribution inside a material due to a surface magnetic dipole is presented. The average permeability is defined. The relation between the flux density inside the inspection head and the thickness of test material has been derived and was experimentally tested. Although the derivation above is based on the surface magnetic charge model, similar steps can be followed as long as we know the field distribution inside the test material, which is dependent on the material properties.

In the future, additional experimental tests of this transfer function should be undertaken as well as the simulation of field distribution inside the test material by finite element methods. As a result, a better transfer function is expected. Also, the present study was focused on the correction of the B component of B-H curve. In practice, the corrections to the H component should also be considered due to the lift-off problem and the surface roughness condition. This will be discussed subsequently.

B. IMPROVEMENT OF MAGNETIC SURFACE MEASUREMENT BY REDUCING THE LIFT-OFF EFFECT

Background

In surface magnetic inspection, the result of the magnetic measurement is very sensitive to the test condition, including the way the inspection head is contacted with the test specimen. The fluctuation of magnetic test results due to the unstable or irreproducible contact of the inspection head with the test specimen is defined as the life-off problem. This is a very common practical problem and should be addressed, especially for on-site NDE measurements where the surface preparation should be a minimum. Since magnetic NDE techniques are relatively new, this problem has rarely been considered.

The variations of the magnetic measurements caused by the lift-off problem are usually due to the surface roughness and surface curvature of the test specimen. For example, in recent on-site measurement of creep effects in steam pipes [9], it was found that the unstable contact of a flat inspection head with the rounded pipe was one of the largest factors causing data fluctuation in magnetic measurements. Similarly, the instability problem of an inspection head on bridge steel also caused of data fluctuation [10]. Therefore, in general, it is believed that the minimization of lift-off effect can be achieved by a stable contact of the inspection head with the test material is necessary for a good surface magnetic measurements. However, this condition can not always be achieved.

In this study, the influence of lift-off effect on the magnetic measurement has been diminished by two techniques: use of a magnetic coupling gel and by pre-lifting the

inspection head a fixed distance above the test material. The function of magnetic gel is to enhance the magnetic coupling across the interface between the inspection head and the test sample. The purpose of pre-lifting is to reduce the relative effects of changes in the size of the gap on the magnetic measurement. These two techniques are both applicable when good contact of inspection head with the test material is impossible.

Experimental

Magnetic coupling gel A magnetic coupling gel is a fine, chemically stable mixture of single domain magnetic particles with petroleum jelly. The magnetic coupling gel used in this study was made in Ames Laboratory, using an iron particle mixture with vaseline. The magnetic properties of magnetic coupling gel were measured in a solenoid using the Magscope [11]. The experimental setup is shown in Fig. 62. The Hall probe used here. The specimen was prepared by filling a plastic tube with the magnetic coupling gel. The ratio of the length to the diameter of the specimen was 7.27, therefore, carrying a nominal demagnetization coefficient $N_d/4\pi$ of 0.013 [12]. The measured hysteresis curve was later corrected according to this value. System calibration was also performed by obtaining a B-H loop without any specimen, so that the actual permeability of magnetic coupling gel can be determined.

Measurement with magnetic coupling gel The specimens used in this investigation were three pieces of P22 Cr-Mo steel [13], labeled as Specimen B, C, D, shown in Fig. 39. These specimens were cut from the steam pipe of a fossil power plant with different degrees of swelling and surface roughness. The outer diameter of these specimens were about 13

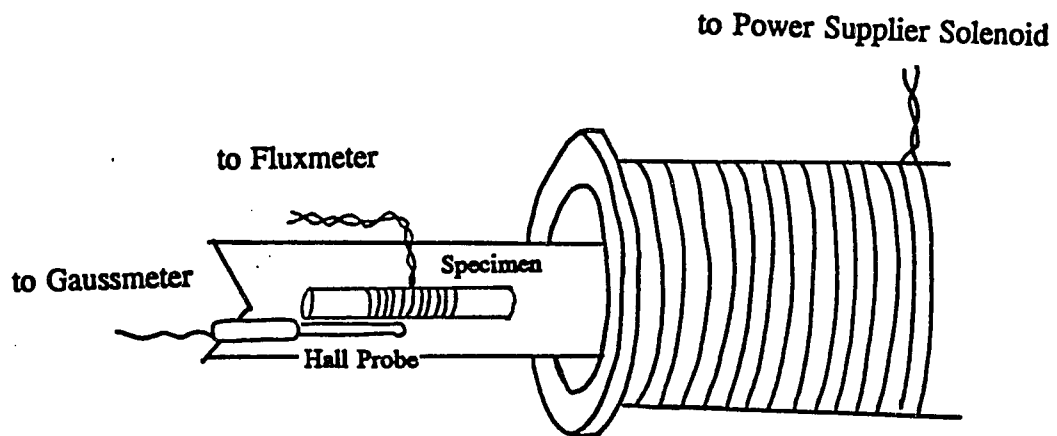


Fig. 62. Measurement of magnetic hysteresis curve of magnetic coupling gel by solenoid.

3/4". Magnetic hysteresis measurements were performed by placing a flat inspection head on the outer surface of each specimen with three different interface conditions between the inspection head and the test material: (1) with magnetic coupling gel as the interface medium, (2) with vacuum grease as the interface medium and (3) with direct dry contact. The measurement configuration is shown in Fig. 63. Magnetic hysteresis parameters, such as coercivity, remanence and initial permeability were measured by the Magnescope [11]. Eight measurements were repeated on each surface of a specimen under each test condition. Statistical analysis was later performed to compare the standard deviation of the test results.

Measurement with pre-lifting The specimens used in this investigation were also three pieces of P22 Cr-Mo steel, as mentioned above: Specimen B, C, D. Each specimen had a smooth radial surface with surface roughness giving an average peak-to-peak distance of about 8 micro inch, and a rough radial surface with surface roughness peak-to-peak distance of about 500 micro inch. The roughness of the surfaces was estimated by comparing with GE Standard Roughness Specimen, Cat. 8651831G2. The hysteresis measurements were taken under four test conditions, with the inspection head positioned (a) directly on the smooth surface, (b) directly on the rough surface, (c) on the smooth surface with a sheet of paper as cushion, and (d) on the rough surface with a sheet of paper as cushion. Measurements were performed for each test condition at eight different spots equally spaced on the surface. The measurement configuration is shown in Fig. 64. Statistical analysis was later performed to find the standard deviation of the eight measurements.

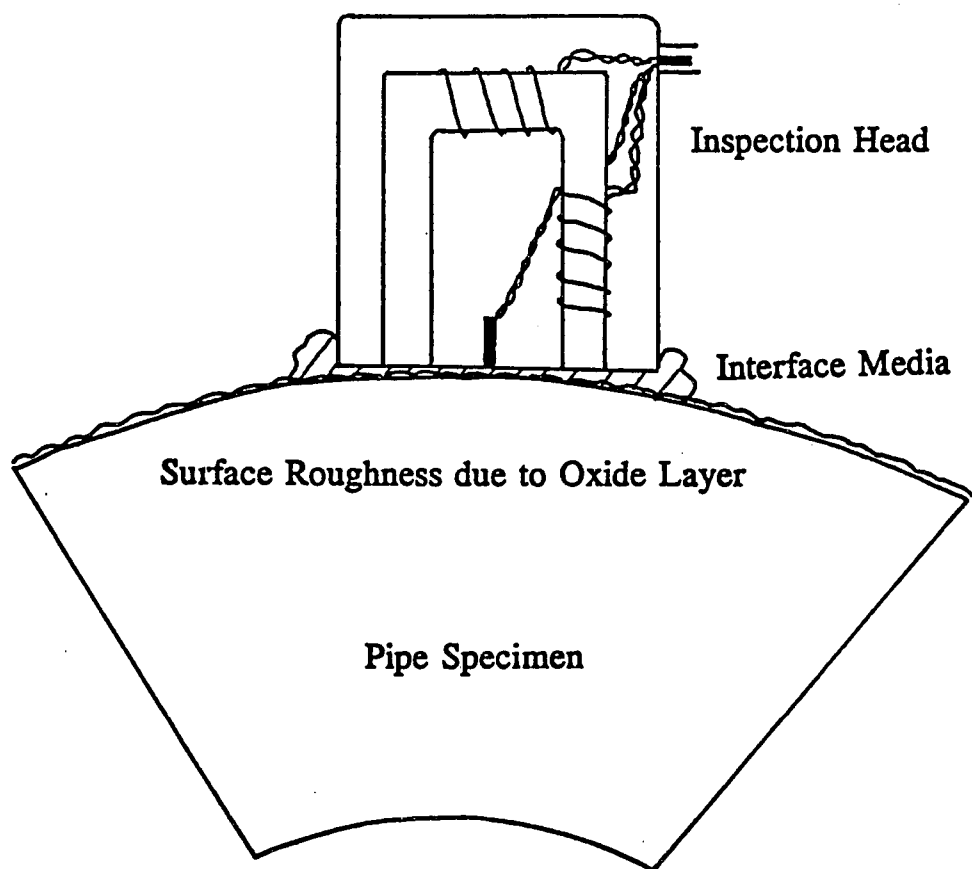


Fig. 63. Surface magnetic hysteresis measurement from the outer surface of the pipe specimen.

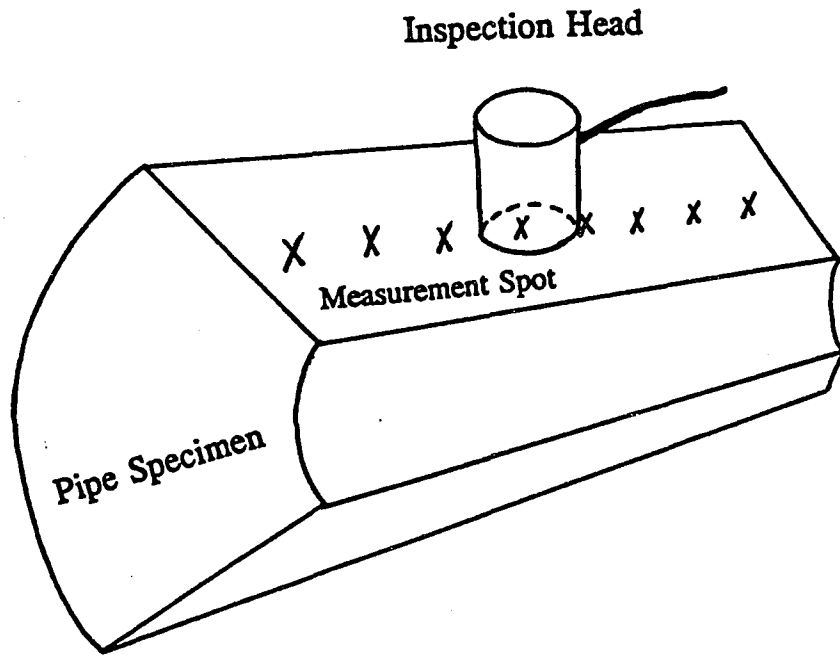


Fig. 64. Surface magnetic hysteresis measurement from the radial surface of the pipe specimen (X: stands for measurement location).

Results and Discussions

Magnetic coupling gel Magnetic properties of the magnetic coupling gel are shown in Fig. 65. The hysteresis loop shows little hysteresis loss and a small coercivity, therefore the magnetic coupling gel can be treated as a superparamagnetic material. The average relative permeability, being the most important parameter for magnetic coupling, was calculated at about 3.34. This value is mainly determined by the nature of the magnetic particle and by the volumetric loading of this material. The greater the quantity of magnetic particle in petroleum jelly, the higher the permeability of the gel.

Effect of magnetic coupling gel on test results Test results of hysteresis measurements taken at the outer surfaces of these specimens and the statistical analysis are shown in Fig. 66 - 67. It can be seen that in Specimen D and C, the measurement with direct dry contact had the largest variation, the measurement with the aid of magnetic coupling gel had the least variation and the measurement with vacuum grease was intermediate.

The largest variation of magnetic measurement in the direct contact case is caused by the lift-off problem due to the poor magnetic contact of inspection head with the curved outer surface of the specimen. Vacuum grease improves the repeatability of the test result by providing a stable physical contact between the inspection head and the specimen. Magnetic coupling gel provides not only a stable physical contact, but also a better magnetic coupling due to its higher permeability. The higher permeability of the magnetic coupling gel reduced the influence of the air gap inside the magnetic circuit on the measurement results by a factor of 3.34, which is the relative permeability of the magnetic coupling gel.

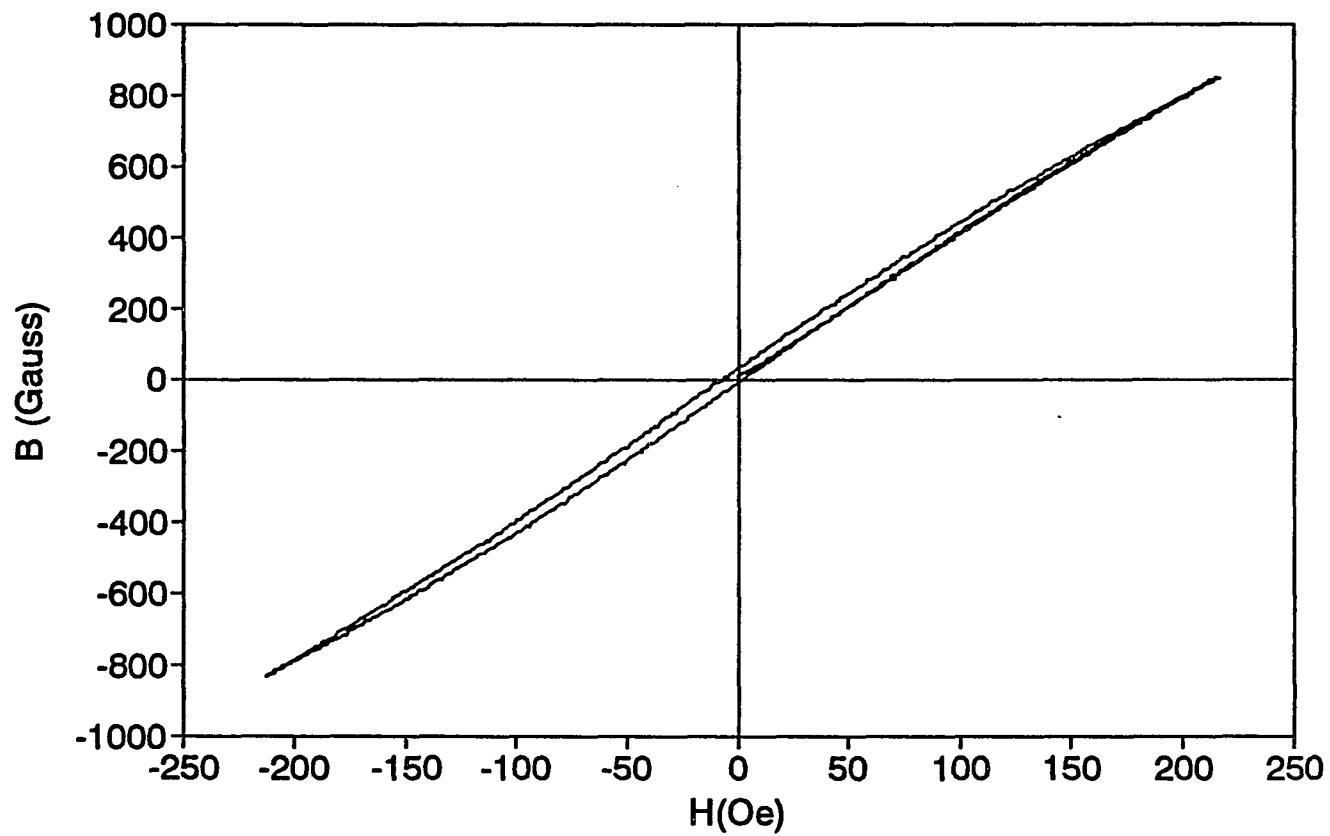


Fig. 65. Magnetic hysteresis curve of magnetic coupling gel.

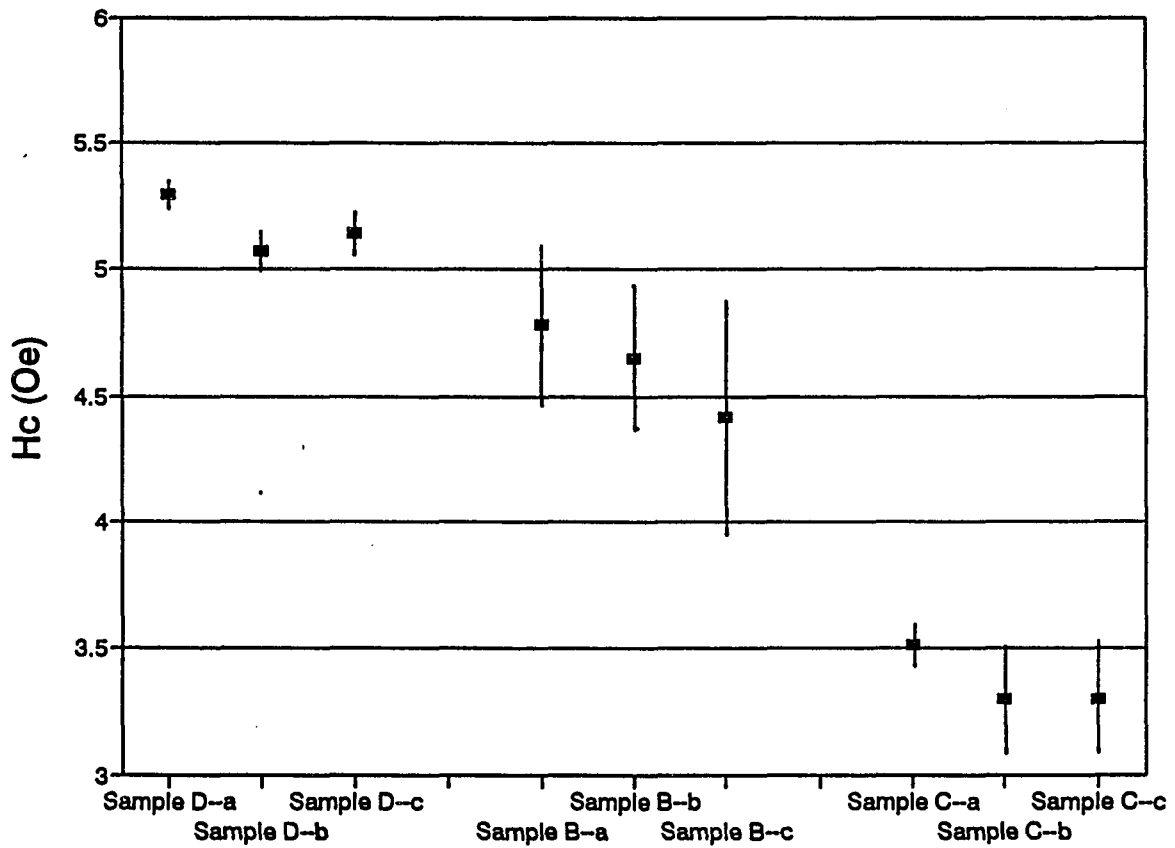


Fig. 66. Coercivity of the test specimens at different measurement conditions. Error bar stands for one standard deviation of eight measurements. (Measurement condition: (a) measurement with magnetic coupling gel as interface media, (b) measurement with vacuum grease as interface media, (c) measurement with direct dry contact).

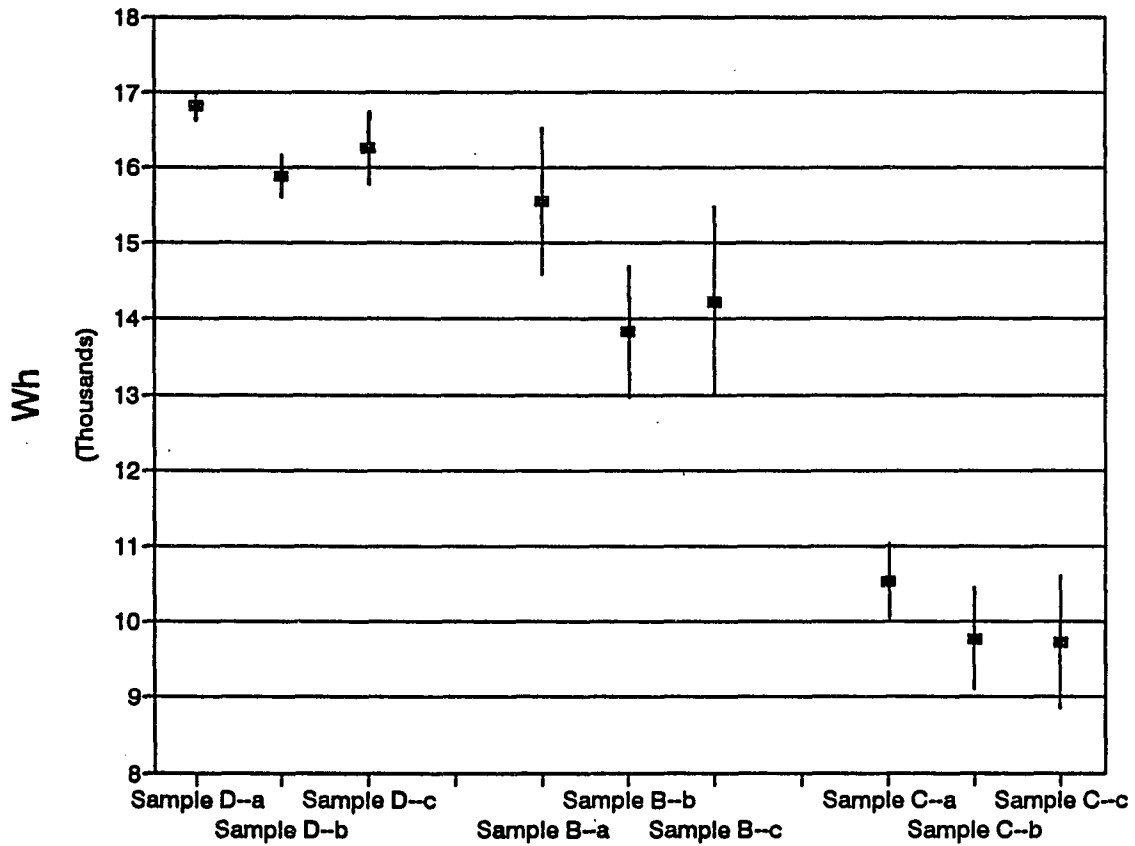


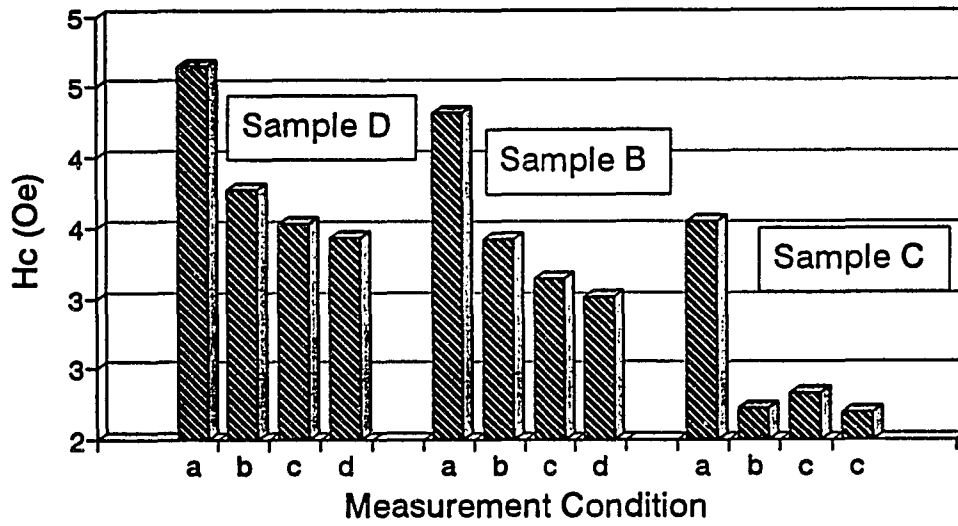
Fig. 67. Hysteresis loss of the test specimens at different measurement conditions. Error bar stands for one standard deviation of eight measurements. (Measurement condition: (a) measurement with magnetic coupling gel as interface media, (b) measurement with vacuum grease as interface media, (c) measurement with direct dry contact.

The result on Specimen B, however, shows no advantage of magnetic coupling gel over vacuum grease. This is because of the very poor surface condition of this specimen. (There was significant surface roughness near the thermocouple hole. See Fig. 39.) In this situation, stable physical contact is the most important factor in ensuring reproducible magnetic measurements. Therefore, as a consequence of this, the test results with magnetic coupling gel and vacuum grease are quite similar.

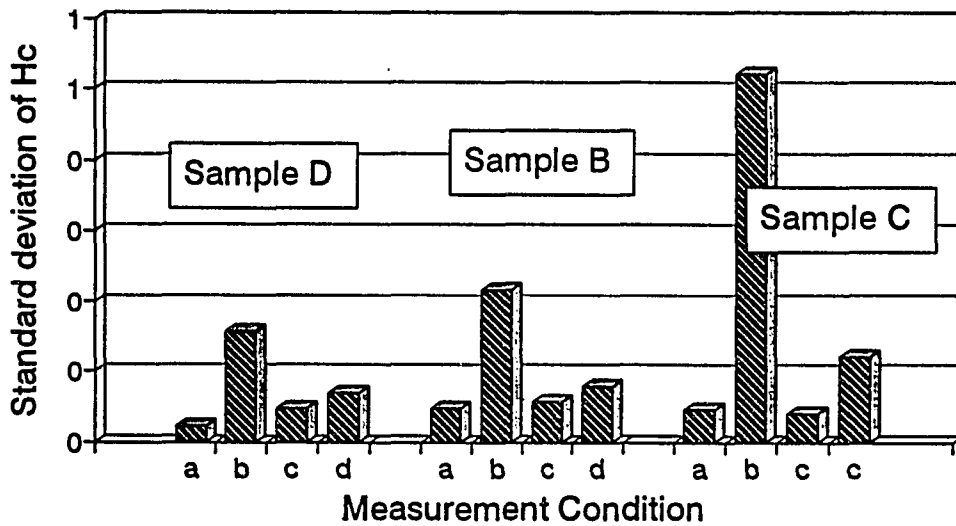
Effect of pre-lifting on measurement results Test results of magnetic properties and their standard deviation are shown in Fig. 68 - 70. It can be seen that by lifting a predetermined distance between the inspection head and the test specimen, two good effects on the surface measurement are introduced:

(1) The differences between the measurement results with different surface conditions are reduced, while the differences between different samples are still preserved. (Note that the difference of measurement result between test condition (c) and (d) is much less than that between (a) and (b), and the difference between specimens are almost the same for all test conditions.) In a practical situation, this means that by properly pre-lifting, the influence on magnetic measurement due to the lift-off problem and the real material properties can be separated.

(2) The measurement fluctuation due to the lift-off problem is significantly reduced compared with the measurement condition of case (b). This means that by properly pre-lifting, the measurement variation becomes less sensitive to the surface condition of the test specimen, which is advantageous for extracting intrinsic magnetic properties from the measurement.

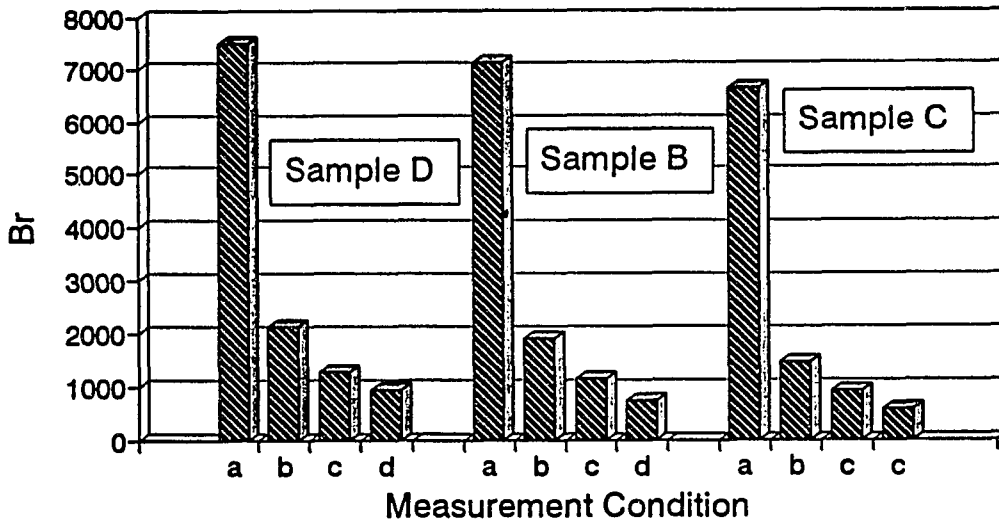


(i)

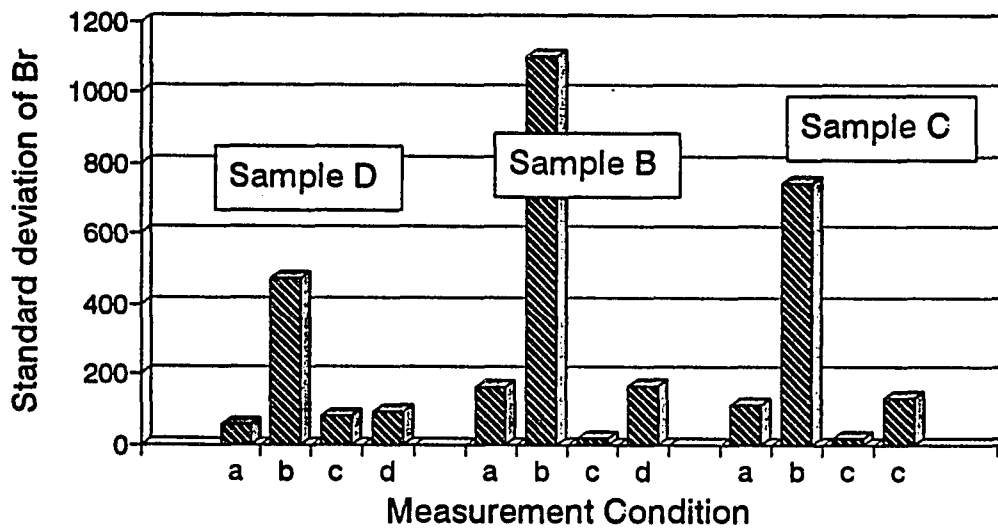


(ii)

Fig. 68. (i) Coercivity of test specimens at different measurement conditions. (ii) Standard deviation of coercivity of eight measurement. (Measurement condition: with inspection head positioned (a) directly on smooth side, (b) directly on rough side, (c) on smooth side with a sheet of paper as cushion, and (d) on rough side with a sheet of paper as cushion).

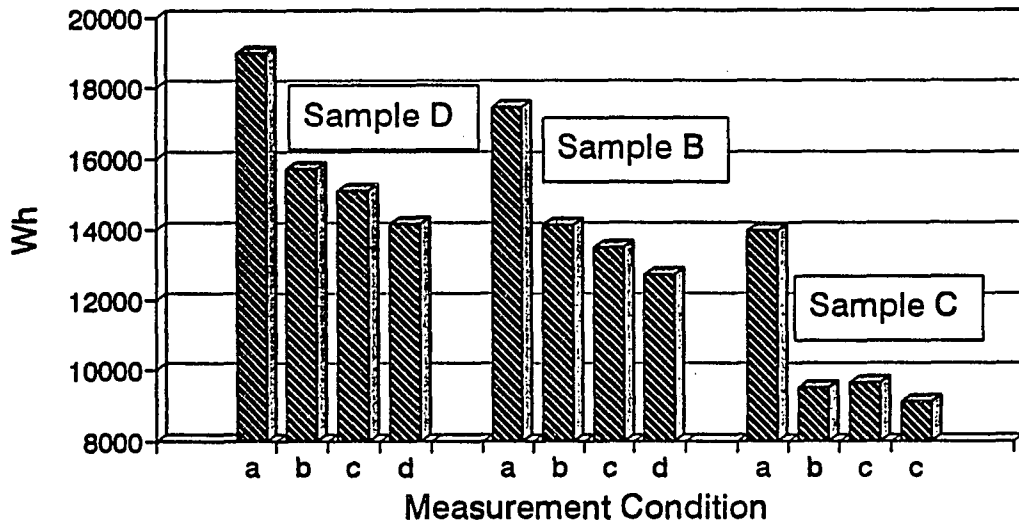


(i)

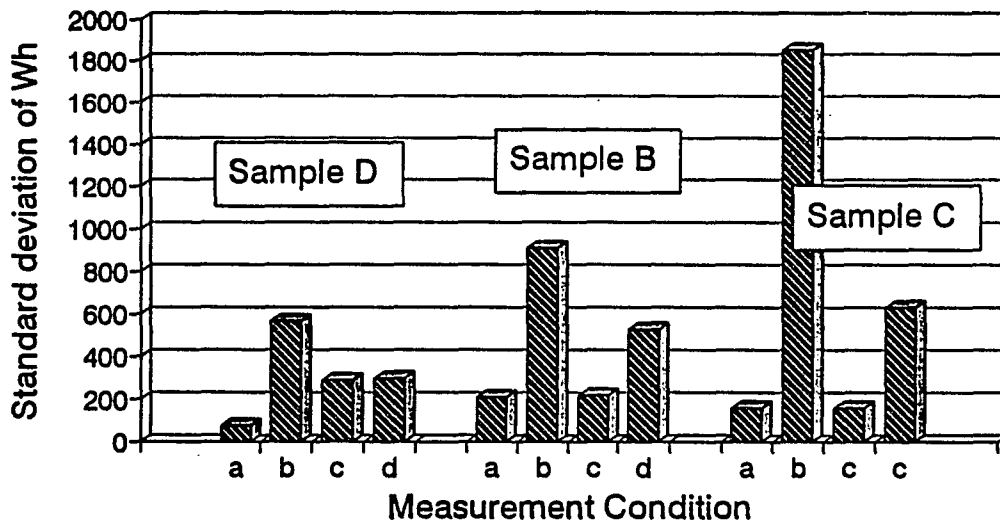


(ii)

Fig. 69. (i) Remanence of test specimens at different measurement conditions. (ii) Standard deviation of remanence of eight measurement. (Measurement condition: with inspection head positioned (a) directly on smooth side, (b) directly on rough side, (c) on smooth side with a sheet of paper as cushion, and (d) on rough side with a sheet of paper as cushion).



(i)



(ii)

Fig. 70. (i) Hysteresis loss of test specimens at different measurement conditions. (ii) Standard deviation of hysteresis loss of eight measurement. (Measurement condition: with inspection head positioned (a) directly on smooth side, (b) directly on rough side, (c) on smooth side with a sheet of paper as cushion, and (d) on rough side with a sheet of paper as cushion).

Both (1) and (2) indicate that the lift-off effect can be used to improve the measurement result. For example, if two specimens for evaluation have different surface conditions, by properly pre-lifting or taking measurement at different lift-off distances, the pure difference due their intrinsic material properties can be deduced.

Magnetic Circuit Model

The magnetic coupling effect of the magnetic coupling gel and the pre-lifting effect can be analyzed by the magnetic circuit model shown in Fig. 71. According to Ampere's circuital law [14],

$$Ni = H_1 l_1 + H_2 l_2 + H_3 l_3 \quad (48)$$

where Ni is the magnetomotive force provided by the power coil and l_1, l_2, l_3 are the mean magnetic flux path inside the inspection head, interface and test material. Suppose there is no flux leakage, due to the magnetic flux continuity, we can get:

$$A_1 \mu_1 H_1 = A_2 \mu_2 H_2 = A_3 \mu_3 H_3 \quad (49)$$

where A_1, A_2, A_3 and μ_1, μ_2, μ_3 are the average cross sections and permeabilities of the inspection head, interface and the test material. Working with the above equations, the magnetic field inside the test material can be determined from:

$$H_3 = \frac{A_1 A_2 \mu_1 \mu_2 Ni}{A_1 A_2 \mu_1 \mu_2 l_3 + A_1 A_3 \mu_1 \mu_3 l_2 + A_2 A_3 \mu_2 \mu_3 l_1} \quad (50)$$

Because the flux spreads out into the test specimen, normally A_3 is greater than A_1 and A_2 . However, here in the interests of simplicity, A_3 will be set equal to A_1 and A_2 .

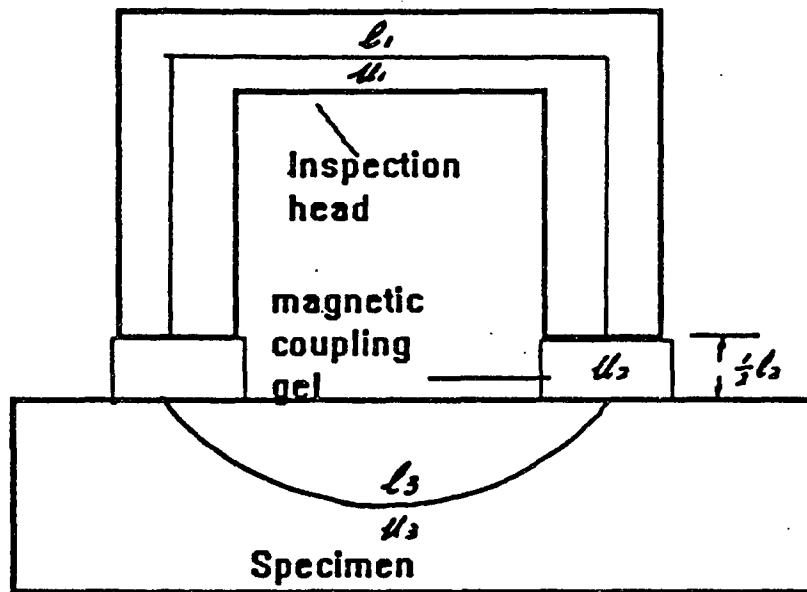


Fig. 71. Diagram of magnetic circuit of surface inspection with interface media.

The variation of the magnetic field (and therefore the measured coercivity) due to the lift-off problem can be analyzed by differentiating H_3 with respect to l_2 . Assuming cross sections of magnetic flux path are the same in a simple case, we can obtain:

$$\frac{dH_3}{dl_2} = -\frac{Ni \mu_1^2 \mu_2 \mu_3}{(\mu_1 \mu_2 l_3 + \mu_1 \mu_3 l_2 + \mu_2 \mu_3 l_3)^2} \quad (51)$$

Coupling effect of magnetic coupling gel If l_2 is so small that the second term in the denominator of Eq. 51 can be neglected, then dH_3/dl_2 is inversely proportional to μ_2 , which means that by filling the interface with magnetic coupling gel, the variation of magnetic field measurement can be reduced. On the other hand, if l_2 is quite large and the second term in the denominator of Eq. 51 dominates, then dH_3/dl_2 is proportional to μ_2 , which means that there is little reduction in the variation of the magnetic field measurement by filling the air gap with magnetic coupling gel. This explains why in Specimen B, the test result with magnetic coupling gel was no better than the measurement with vacuum grease.

The coupling effect of the magnetic coupling gel on a magnetic interface can be illustrated by the following example. It is reasonable to assume the values of the relative permeability of the inspection head and the test material to be 500 and 200 and the flux path of l_1 , l_2 , l_3 to be 10 cm, 0.1 cm and 10 cm respectively. If it is also assumed that the cross sectional areas are the same, then according to Eq. 50:

$$H_3 = \frac{Ni \mu_2}{0.14 (1.4285 + \mu_2)} (A/m) \quad (52)$$

Fig. 72 shows the diagram of the magnetic field inside test material as a function of the permeability of interface material. It can be seen that by filling the air gap with magnetic coupling gel, the magnetic field inside the test material is significantly increased.

Pre-lifting effect From Eq. 51, it can be seen that the variation due to the lift-off effect can also be reduced by increasing l_2 . Actually, the variation is inverse to l_2^2 if other terms in the denominator are small enough. This explains why, by pre-lifting the inspection head a certain distance over the test specimen, the measurement fluctuation due to the variation of l_2 can be reduced. However, the pre-lifted distance should be chosen so that the magnetic properties measured from such an inspection still preserve enough original information about magnetic properties of the test material.

Conclusions

The effects of a magnetic coupling gel and pre-lifting on surface magnetic hysteresis measurement has been investigated. It was found that the magnetic coupling gel can reduce the standard deviation of the test result by providing better magnetic permeance and more stable physical contact between inspection head and test materials. The coupling function of the magnetic coupling gel is mainly due to its higher permeability than the air. It is also found that pre-lifting measurement configuration can enhance the signal to noise ratio of the measurement signal as well as reduce standard deviation. A magnetic circuit model was developed to interpret the experimental result.

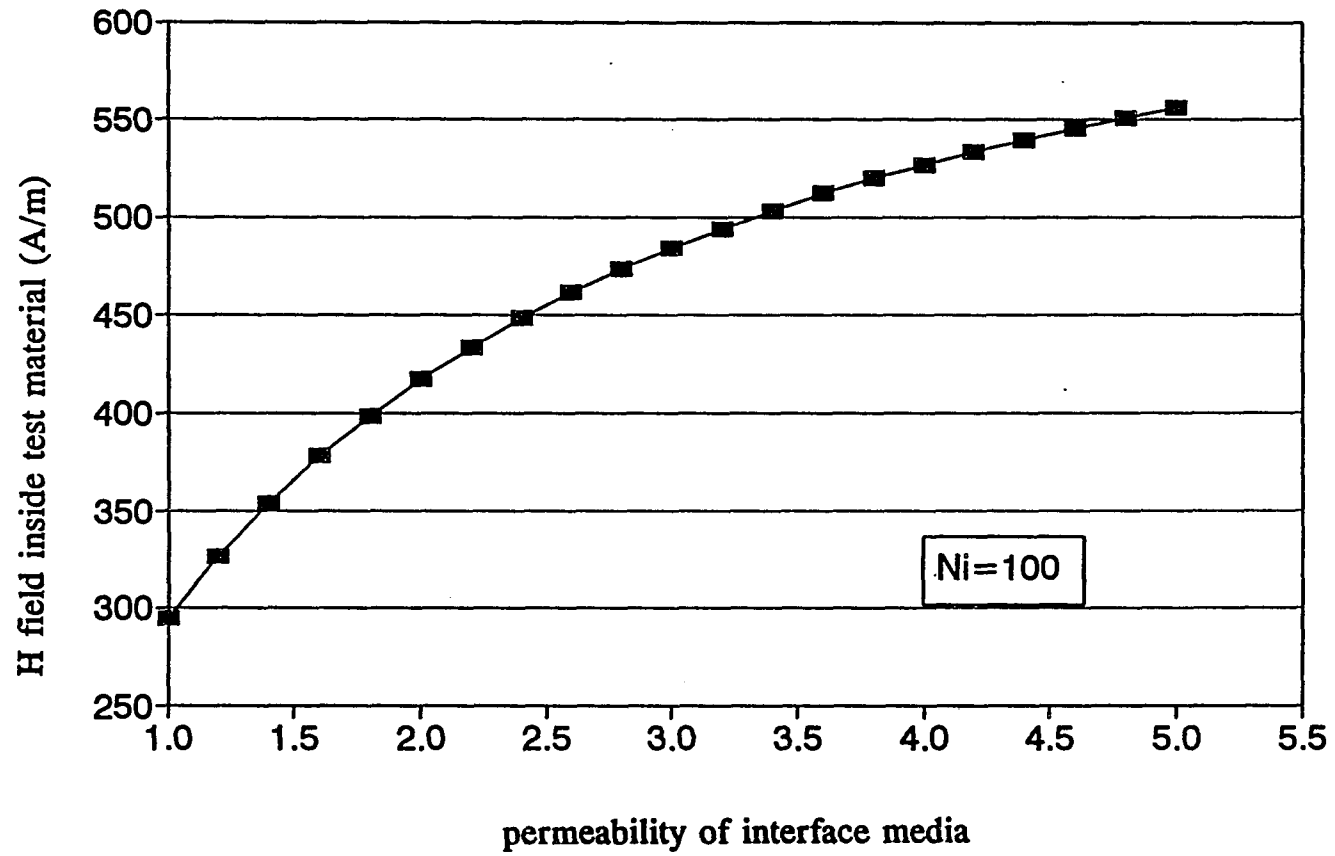


Fig. 72. Magnetic field inside the test material as a function of the permeability of interface media.

REFERENCES

1. Z.J. Chen, D.C. Jiles, J. Kameda, J. Appl. Phys. 75, 6975 (1994)
2. M.K. Devine and D.C. Jiles, IEEE Trans. Mag. MAG-28 2603 (1992).
3. D.A. Kaminski, D.C. Jiles and M.J. Sablik, J. Mag. Mater. 104, 382 (1992).
4. K.F. Bounden, NDT International, 10, 253 (1977).
5. D.L. Atherton and A. Teitsma, J. Appl. Phys. 53, 8130 (1982).
6. British Standards Institution, "Method for magnetic particle flaw detection", British Standard, 6072 (1981).
7. F. Foster, Material Evaluation, 43, 1154 (1985).
8. F. Foster, Material Evaluation, 43, 1398 (1985).
9. M.R. Govindaraju, D.A. Kaminski, M.K. Devine, S.B. Biner and D.C. Jiles, Nondestructive evaluation of creep damage in power-plant steam generators and piping by a new magnetic inspection technique, (to be submitted to J. Appl Phys.).
10. M.K. Devine, A.C. Storm, D.C. Jiles and D. Utrata, Review of Progress in Quantitative Nondestructive Evaluation (Edited by D.O. Thommpson and D.E. Chimenti, Plenum Press, New York, 1994) 13B, p. 1777 .
11. D.C. Jiles, S. Hariharan and M.K. Devine, IEEE Trans. Mag. MAG-26, 2577 (1990).
12. B.D. Cillity, Introduction to Magnetic Material (Addoson-Wesley, 1972), 58-59.
13. Z.J. Chen, M.R. Govindaraju, D.C. Jiles, S.B. Biner and M.J. Sablik, proc. Joint Intermag and MMM Conf., Albuquerque, NM, June, 1994.
14. David Jiles, Introduction to Magnetism and Magnetic Materials (Chapman & Hall, New York, 1991), p. 4.

GENERAL CONCLUSIONS

In this dissertation, the effects of microstructure on magnetic properties of ferromagnetic materials have been discussed. Modelling of structure-sensitive magnetic properties has been presented at the beginning as a contribution to the theory of magnetism. This was followed by discussion of the detection of fatigue damage and creep damage using magnetic hysteresis measurements, which served as contribution in the applications of magnetism. Finally a few magnetic techniques have been presented as practical methods to overcome measurement difficulties.

For the modelling of structural sensitive magnetic properties, a microstructure consisting of localized defects only was considered. By considering reversible domain wall bending at the low field region, and minimizing magnetostatic energy and domain wall energy, initial permeability was found to be proportional to $\rho^{-2/3}$, where ρ was the density of point defects. Besides the modelling of magnetic properties from first principles, the hysteresis model theory was also used to provide more complete information about magnetic properties. In correlating microstructure with the magnetic properties, the relationship between the hysteresis parameter k and defect density ρ was derived. This showed a linear relationship. A model was developed assuming spheroidised carbides Fe_3C in carbon steel acted as point defects in pinning domain wall motion. Theoretical relations were then tested against experimental data.

The study of fatigue effects on magnetic properties were performed on A533B nuclear reactor pressure vessel steel. It was shown that structure-sensitive magnetic properties such

as coercivity, and initial permeability were very sensitive to the fatigue induced microstructure variation. In low cycle fatigue tests under strain controlled conditions, magnetic properties changed dramatically during the last 10% of fatigue life. In high cycle fatigue tests under load controlled conditions, magnetic properties changed throughout the whole fatigue process. Coercivity was found to be linearly related to the logarithm of the number of fatigue cycles. Also, based on domain wall dislocation interactions, a phenomenological model was developed to relate the coercivity with the number of fatigue cycles. Metallurgical studies were also performed to investigate the relationship between fatigue-induced microstructure changes and the magnetic properties of the test material.

Results of the study of creep detection in Cr-Mo steel have also been presented in this dissertation. It was shown that creep damage was usually accompanied by a decrease in coercivity and remanence, which could be explained by the creep-induced microstructure changes. These include (1) the segregation of defects to grain boundary and (2) the formation of grain boundary cavitation. Based on these assumptions, a numerical model was developed to simulate the experimental data. Metallurgical investigation by SEM, EDS and optical microscopy were performed to study the creep-induced microstructure changes. These consisted mainly of grain boundary cavitation.

Finally, practical techniques for surface magnetic hysteresis measurement were presented with the aim of extracting intrinsic magnetic properties and reduced measurement error. Discussions were focused on the derivation of a transfer function with flux leakage correction and geometry effect correction. In solving the lift-off problem in surface magnetic hysteresis measurement, use of a magnetic coupling gel and pre-lifting technique were found

to be useful in the reduction of measurement error. A magnetic circuit model was also developed to interpret the results of in-situ measurements.

GENERAL REFERENCES

1. D.C. Jiles, *NDT International*, 21, 311 (1988).
2. D.C. Jiles, *NDT International*, 23, 83 (1990).
3. M.K. Devine, *JOM*, 44(10), 24 (1992).
4. G.A. Matzkanim, E. Beissner and C.N. Teller, Report NTIAC-79-2, Nondestructive Testing Information Analysis Center, Southwest Research Institute, San Antonio, Texas, October 1979.
5. D.C. Jiles, T.T. Chang, D.R. Hougen and Ranjan, *J. Appl. Phys.* 64, 3620 (1988).
6. R. Langman, *IEEE Trans. Mag.* MAG-26, 1246 (1990).
7. D.C. Jiles, *J. Phys. D: Appl. Phys.*, 21, 1196 (1988).
8. D.C. Jiles and D.Utrata, *J. NDE*, 6, 129 (1988).
9. B.K Tanner, J.A. Szpunar, S.N. M. Willcock, L.L. Morgan and P.A. Mundell, *J. Mater. Sci.*, 23, 4534 (1988).
10. R.Ranjan, O. Buck and R.B. Thompson, *J. Appl. Phys.* 61, 3196 (1987).
11. J. Sternberk, E.Kralochvilova, J.Hrebik and A. Gemperle, *Phys Stat. Sol. (a)*, 79, 523 (1983).
12. I.A. Vais, Yu.P.Bashkirov, A.E.Ivanskii, G.V. Bida, E.D. Sakovich and V.E.Strelyanov, *Sov. J. NDT*, 23, 86 (1987).
13. D.C. Jiles, *J. Appl. Phys.* 63, 2980 (1988).
14. W.A. Theiner, I. Altpeter and R. Kern, *Nondestructive Characterization of Material II* (Edited by C.O. Ruud, R.E. Green and J.F. Bussieve, Plenum Press, New York, 1986), p. 233.
15. M.N. Mikheev, V.M. Morozova, N.V. Renez and G.V. Surin, *Sov J. NDT*, 13, 545 (1977).
16. M.N. Mikheev, E.S. Gorkunov and F.N. Dunaev, *Sov. J. of NDT*, 13, 613 (1977).

17. N.A. Vekser, A.S. Smirnov, A.Y. Fadeev, M.M. Shel, V.F. Tokunov and V.A. Gudyrya, *Sov. J. NDT*, 11, 183 (1977).
18. G.A. Pyatunin and V.I.Slavov, *Sov. J. NDT*, 14, 1027 (1978).
19. J.F. Bussiere, M.Lord and M. Nott, *Non-destructive testing, Proceedings of the 4th European Conference, London, U.K. 1863* (1987).
20. J.F. Bussiere, *Material Evaluation*, 44, 560 (1986).
21. S.A Musikhin, V.F. Novikov and V.N. Borsenko, *Sov. J. NDT*, 24, 633 (1988).
22. M.S.C. Bose, *NDT International*, 19, 83 (1986).
23. M.K. Devine, S. Hariharan and D.C. Jiles, *Review of Progress in Quantitative Nondestructive Evaluation* (Edited by D.O. Thompson and D.E. Chimenti, Plenum Press, NY, 1991), 10, p. 2021.
24. M.K. Devine and D.C. Jiles, *IEEE Trans. Mag.* MAG-28, 2603 (1992).
25. M.K. Devine, D.C. Jiles, J. Apostol and P.K. Liaw, *Review of Progress in Quantitative Nondestructive Evaluation* (Edited by D.O. Thompson and D.E. Chimenti, Plenum Press, New York, 1992), 11, p. 1777.
26. D.C. Jiles, S. Hariharan and M.K. Devine, *IEEE Trans. Mag.* MAG-26 26(5), 2577 (1990).
27. A. Parakka and D.C Jiles, to be submitted to *IEEE Trans. Mag.*
28. R. Langman, *NDT International*, 14(5), 255 (1981).
29. D.C. Jiles and D.L. Atherton, *IEEE Trans. Mag.* MAG-19, 2183 (1983).
30. D.C. Jiles and D.L. Atherton, *J. Appl. Phys.* 55, 2115 (1984).
31. P.Garikipati, T.T. Chang and D.C. Jiles, *IEEE Transa. Mag.* MAG-24, 2922 (1988).
32. M.J. Sablik, H.Kwun, G.L. Burkhardt and D.C. Jiles, *J. Appl. Phys.* 61, 3799 (1987).
33. H.R. Hilzinger, H.Kronmuller, *J. Mag. Mater.* 2, 11 (1976).

34. D.E. Scherpereel, L.L.Kazmerski and C.W. Allen, *Metallurgical Transaction*, 1, 517 (1970).
35. P. Gaunt, *Philos Mag.B*, 48, 261 (1983).
36. M.K. Devine, A.C. Storm, D.C. Jiles and D.Utrata, *Review of Progress in Quantitative Nondestructive Evaluation* (Edited by D.O. Thompson and D.E. Chimenti, Plenum Press, New York, 1994), 13B, p. 1777.
37. M.R. Govindaraju, D.A. Kaminski, M.K. Devine, S.B. Biner and D.C. Jiles, Nondestructive evaluation of creep damage in power-plant steam generators and piping by a new magnetic inspection technique, to be submitted to *J. Appl. Phys.*

ACKNOWLEDGEMENTS

I would like to express my sincere gratitude to many important people.

First of all, I am greatly indebted to my major professor Dr. David C. Jiles for his wise guidance and warm encouragement throughout the course of this study. His professional and personal instruction will be benefit to me for a life time.

Secondly, I would like to extend my appreciation to Dr. S.B. Biner, Dr. M. Sablik and Dr. J. Kameda for their helpful suggestion and discussion.

Thirdly, I would also like to thank Dr. W. Lord, Dr. S. Udpa, Dr. R. Weber and Dr. K. Vedula for dedicating their time to serve on my committee.

Also many thanks are towards my coworkers in the magnetics group of Ames Laboratory. Their advice, thoughts, expertise and friendship through the course of this research are extremely useful.

Finally I would like to dedicate this work to my grandmother and my parents for their dreams, sacrifice and encouragement. I am greatly thankful to my wife for her constant encouragement, support and patience.

Financial support for this dissertation was from U.S. Nuclear Regular Commission, Electric Power Research Institute and U.S. Department of Energy.